

# Chemical abundances of the outer halo stars in the Milky Way \*

Miho ISHIGAKI

*Astronomical Institute, Tohoku University, Sendai 980-8578, Japan*  
*miho@astr.tohoku.ac.jp*

Masashi CHIBA

*Astronomical Institute, Tohoku University, Sendai 980-8578, Japan*  
*chiba@astr.tohoku.ac.jp*

and

Wako AOKI

*National Astronomical Observatory, Mitaka, Tokyo 181-8588, Japan*  
*aoki.wako@nao.ac.jp*

(Received ; accepted )

## Abstract

We present chemical abundances of 57 metal-poor ( $[\text{Fe}/\text{H}] < -1$ ) stars that are likely constituents of the outer stellar halo in the Milky Way. Almost all of the sample stars have an orbit reaching a maximum vertical distance ( $Z_{\text{max}}$ ) of  $> 5$  kpc above and below the Galactic plane. High-resolution ( $R \sim 50000 - 55000$ ), high signal-to-noise ( $S/N > 100$ ) spectra for the sample stars obtained with Subaru/HDS are used to derive chemical abundances of Na, Mg, Ca, Ti, Cr, Mn, Fe, Ni, Zn, Y and Ba with an LTE abundance analysis code. The resulting abundance data are combined with those presented in literature that mostly targeted at smaller  $Z_{\text{max}}$  stars, and both data are used to investigate any systematic trends in detailed abundance patterns depending on their kinematics. It is shown that, in the metallicity range of  $-2 < [\text{Fe}/\text{H}] < -1$ , the  $[\text{Mg}/\text{Fe}]$  ratios for the stars with  $Z_{\text{max}} > 5$  kpc are systematically lower ( $\sim 0.1$  dex) than those with smaller  $Z_{\text{max}}$ . For this metallicity range, a modest degree of depression in the  $[\text{Si}/\text{Fe}]$  and the  $[\text{Ca}/\text{Fe}]$  ratios are also observed. This result of the lower  $[\alpha/\text{Fe}]$  for the assumed outer halo stars is consistent with previous studies that found a signature of lower  $[\alpha/\text{Fe}]$  ratios for stars with extreme kinematics. A distribution of the  $[\text{Mg}/\text{Fe}]$  ratios for the outer halo stars partly overlaps with that for stars belonging to the Milky Way dwarf satellites in the metallicity interval of  $-2 < [\text{Fe}/\text{H}] < -1$  and spans a range intermediate between the distributions for the inner halo stars and the stars belonging to the satellites. Our results confirm inhomogeneous nature of chemical abundances within the Milky Way stellar halo depending on kinematic properties

of constituent stars as suggested by earlier studies. Possible implications for the formation of the Milky Way halo and its relevance to the suggested dual nature of the halo are discussed.

**Key words:** Galaxy:abundances—Galaxy:halo—Galaxy:kinematics and dynamics

## 1. Introduction

Based on recent theoretical and observational studies, it is now widely believed that the stellar halo of the Milky Way (MW) Galaxy has formed through a series of accretions of smaller subsystems in the course of the hierarchical galaxy formation in the Universe. Recent numerical simulations, based on the standard  $\Lambda$ CDM model, predict that such accretion events leave various substructures within a stellar halo of MW-sized ( $\sim 10^{12}M_{\odot}$ ) galaxies (e.g., Diemand et al. 2007). This prediction is well supported by discoveries of various substructures in the MW halo (e.g., Belokurov et al. 2006) as well as in the halos of nearby galaxies (e.g., Brown et al. 2008; Richardson et al. 2009; Martinez-Delgado et al. 2008) as can be identified in spatial distribution, kinematics and metallicity of constituent stars. As an example, recent extensive photometric surveys of the MW halo reveal clumpy spatial distributions of stars being apart from the smooth underlying component, such as Sagittarius dwarf galaxy (Ibata et al. 1994; Majewski et al. 2003) or Virgo overdensity (Juric et al. 2008; An et al. 2009). Furthermore, a kinematic substructure of stellar tidal debris remains longer than a spatial substructure, providing insights into the earlier stage of the MW formation (e.g., Helmi & White 1999; Johnston et al. 2008). Indeed, presence of substructures in a velocity or an angular-momentum space has been reported by several authors (e.g., Helmi et al. 1999; Chiba & Beers 2000; Kepley et al. 2007; Dettbarn et al. 2007; Klement et al. 2009; Morrison et al. 2009; Starkenburg et al. 2009; Schlaufman et al. 2009).

Further observational constraints on the formation of the MW stellar halo have been suggested from the fact that the halo comprises of two structural components, the inner and the outer halos, using kinematics and metallicity (e.g., Sommer-Larsen & Zhen 1990; Norris 1994; Chiba & Beers 2000; Carollo et al. 2007; Carollo et al. 2009). In particular, Carollo et al. (2007) showed using SDSS data that the inner halo exhibits a modest net prograde rotation and the average metallicity of  $[\text{Fe}/\text{H}] \sim -1.6$ <sup>1</sup> while the outer halo has a net retrograde rotation with the lower average metallicity ( $[\text{Fe}/\text{H}] \sim -2.2$ ). Based on these results, they suggested that the inner and the outer halos cannot be formed at once through a monolithic collapse but

---

\* Based on data collected at the Subaru Telescope, which is operated by the National Astronomical Observatory of Japan

<sup>1</sup>  $[\text{Fe}/\text{H}] = \log A(\text{Fe}) - \log A_{\odot}(\text{Fe})$

may have been formed through different mechanisms with different timescales and formation epoch. In particular, the results are consistent with the hypothesis that the accretion of dwarf spheroidal galaxies (dSphs) have played more important role in the outer halo.

These recent discoveries of substructures as well as characteristic features of the inner and the outer halos provide us with a concrete picture for the current state of the MW stellar halo as being a collective entity of accreted subsystems and their tidal debris (e.g., Bell et al. 2008). However, the origins of individual structures have not yet been well constrained through phase space information alone because a relaxation process during the dynamical evolution of the MW progressively smears out such substructures and because the accurate measurements of distances and kinematics are yet limited.

It has been recognized that detailed chemical abundance of metal-poor stars provides a fossil signature of the early epoch of the MW formation (e.g., Freeman & Bland-Hawthorn 2002). Important advantage of using chemical abundance of metal-poor stars as a tracer is that the metal-poor stars formed early in the Universe and thus retain materials from that epoch in their atmosphere. Therefore, abundance pattern of the stellar atmosphere reflects that of the star forming clouds at the formation sites. In particular, ratios of the abundance of key elements including  $\alpha$ -elements (Mg, Si, Ca and Ti), Fe-peak elements (Cr, Ni, etc.) and neutron capture (Y, Ba, etc.) elements can be used to infer star formation history based on chemical evolution models, where these elements are predominantly ejected through either Type II or Type Ia SNe.

Although the nucleosynthesis mechanisms of these elements are not fully understood, they provide unique constraints on the halo formation especially when they are used together with kinematics. Indeed, important insights about the early evolution of the MW have been obtained through the analysis of chemical abundance patterns of field halo stars in combination with their kinematics (e.g., Nissen & Schuster 1997; Hanson et al. 1998; Stephens 1999; Fulbright 2002; Stephens & Boesgaard 2002, hereafter SB02; Gratton et al. 2003b, Venn et al. 2004; Roederer 2008). SB02 suggested that  $\alpha$ -elements to iron abundance ratios ( $[\alpha/\text{Fe}]$ ) weakly decrease with increasing apogalactic distance along the galactic plane ( $R_{\text{apo}}$ ) for their  $\sim 60$  sample of metal-poor ( $-4 < [\text{Fe}/\text{H}] < -1$ ) halo stars. Fulbright (2002) also reported the weak correlation of abundance ratios for  $\alpha$  elements with the Galactic rest frame velocity,  $V_{\text{RF}}$ . Both of their sample of field halo stars were reported to have distinct abundances compared to the MW dwarf satellite galaxies. These results are inconsistent with a crude expectation that the MW halo stars may exhibit similar abundance to the MW satellites if dominant halo populations have been accreted from systems similar to these satellites.

A possible interpretation for the abundance discrepancy between the field halo and the MW satellites has been investigated with numerical simulations that implement both cosmologically motivated mass accretion history and chemical evolution for individual building blocks (Robertson et al. 2005; Font et al. 2006a, 2006b; De Lucia & Helmi 2008). Font et al. (2006a)

suggest that the discrepancy in the  $[\alpha/\text{Fe}]$  ratios is a natural expectation from the standard  $\Lambda\text{CDM}$  model if the majority of the MW halo was formed by accretions of a few massive ( $\sim 10^8 - 10^{10} M_\odot$ ) subhalos that had been disrupted early on ( $> 8 - 9$  Gyr ago). In their model, the proposed progenitor subhalos (“building blocks” of the MW host halo) had been enriched with  $\alpha$  elements ejected from Type II SNe associated with a rapid formation of massive stars. The model assumes that the rapid enrichment with the Type II SNe ejecta was subsequently truncated due to the accretion onto the MW halo which can result in enhanced  $[\alpha/\text{Fe}]$  ratios commonly observed among the present-day halo stars. In contrast, the surviving satellite galaxies are modeled to be enriched with iron-rich materials ejected with Type Ia SNe, whose explosion rate is expected to peak at a later time than Type II SNe as modeled by Matteucci & Greggio (1986), resulting in the observed lower  $[\alpha/\text{Fe}]$  ratios.

Following these theoretical implications, it is now important to measure abundances of  $\alpha$  and other key elements for individual stars over a large volume of the stellar halo in order to obtain further constraints on properties and an assembly history of the possible building blocks. In particular, in spite of the fact that the outer halo exhibits characteristics of hierarchically accreted stellar system in contrast to the inner halo (Carollo et al. 2007), abundance data for the outer halo stars are currently quite insufficient. In obtaining high-resolution spectra with required quality and statistics for the halo stars, however, a fundamental problem is that the survey volume is limited to the solar neighborhood (within  $\lesssim 2$  kpc). Therefore, the kinematic information of stars is essential to select stars in remote locations of the halo. The kinematic information including radial velocities, proper motions and distant estimates from the Hipparcos mission and other grand-based surveys are available for calculating orbital parameters of such halo stars (Beers et al. 2000; Chiba & Beers 2000). These data can be used to select targets for the candidate outer halo stars for the purpose of examining similarities and differences in detailed chemical abundances among the recently reported inner and outer halo populations (Carollo et al. 2007; Roederer 2008).

In this paper, we analyze the dependence of chemical abundance of halo stars on their kinematics, based on a large data set assembled from our observations and literature. The most significant point of this work is the inclusion of a homogeneous sample of 57 metal-poor stars whose orbits reach a maximum vertical distance from the galactic plane ( $Z_{\text{max}}$ ) greater than 5 kpc. Our initial results using a subset of 26 stars observed in 2003 were presented in Zhang et al. (2009) (hereafter Z09). In this paper, we present data for additional  $\sim 30$  stars obtained during 2005-2008. High signal-to-noise ( $>100$ ), high-resolution ( $R \sim 55000$ ) spectroscopy of all of these stars was carried out with the High-Dispersion Spectrograph (HDS: Noguchi et al. 2002) mounted on the Subaru telescope. Chemical abundances of Na, Mg, Si, Ca, Ti, Cr, Zn, Fe, Ni, Mn, Y and Ba are derived with a homogeneous manner for all of these sample. The derived abundances are combined with abundance data published in literature (SB02; Gratton et al. 2003a) resulting in a large sample consisting of  $>200$  stars for which both high-resolution

abundance data and three-dimensional velocity components are available. Section 2 describes our sample considered in the following discussions, which includes stars observed during 2003-2008 or published in literature. Section 3 describes our high resolution spectroscopy for a subset of 28 stars obtained in July 2008. Data reduction and abundance analysis for all of our 57 HDS sample are then presented. Based on the compiled data-set, Section 4 shows abundance trends according to their orbital characteristics. Section 5 discusses implication of these results for the formation of the Galactic halo. Finally, Section 6 presents concluding remarks in this work.

## 2. The Sample

The sample used in our work consists of  $\sim 200$  metal-poor dwarf and giant stars that are presumably belonging to the thin/thick disk or the stellar halo of the MW. This sample can be grouped into three subsets of data based the status of observations and analysis as follows; 1) objects observed during 2005-2008 with Subaru/HDS, whose detailed chemical abundances are derived and calibrated in this work (*the main sample*), 2) objects observed in February 2003 with the Subaru/HDS, whose abundance analysis was performed in Z09. These objects are reanalyzed with the same technique as for the main sample for the purpose of keeping homogeneity in the analysis method, 3) objects observed and analyzed in literature. Properties of each subset are described in the following subsections.

### 2.1. *The main sample*

The major purpose of a set of our observations carried out with Subaru/HDS is to obtain accurate chemical abundances for presumed outer halo stars that are observed and analyzed in a homogeneous manner. For this purpose, bright ( $V < 13$ ) metal-poor ( $[\text{Fe}/\text{H}] < -1$ ) stars with  $Z_{\text{max}} > 5$  kpc are selected for observation from the catalog of non-kinematically selected samples provided by Beers et al. (2000) and the catalog of high-proper motion stars by Carney et al. (1994) and Ryan & Norris (1991), all of which include available radial velocities, proper motions and distance estimates. All of these 29 stars were observed with Subaru/HDS in June and July 2008. Details of the observation, analysis of stellar atmospheric parameters (effective temperature:  $T_{\text{eff}}$ , surface gravity:  $\log g$ , micro-turbulent velocity:  $\xi$ ) and the abundance analysis are described in Section 3.

Other two stars were observed in May 2005 (G 64-12 and G 64-37). These observations were carried out with exceptionally high signal-to-noise ratios for the purpose of a Li abundance estimation. Since they also have  $Z_{\text{max}} > 5$  kpc and were observed with the similar instrumental set-up to the 29 stars described above, they are included in the main sample as well.

### 2.2. *The reanalyzed Subaru/HDS sample*

High-resolution spectra for 26 metal-poor dwarfs and giants selected by the same criteria as the main sample were obtained in February 2003 with Subaru/HDS. These stars have been

independently reduced and analyzed in Z09. The observation was carried out with the similar spectral coverage, spectral resolution and signal-to-noise ratios to the main sample. Details of observations, reduction and analysis and results are given in Z09. In order to keep homogeneity in the current analysis technique, we reanalyzed this subset of data with the same method as for the main sample (Section 3.1-3.3). The derived values of stellar atmospheric parameters and chemical abundance results reasonably agree with each other in the two analysis methods as partially reported by Z09.

### 2.3. *The sample from literature*

The third subset for which both high-resolution abundance analysis and kinematic data are available are taken from SB02 and Gratton et al. (2003a) (hereafter G03). From SB02, data of 46 dwarf stars, which do not have a duplicated measurement with this work, are employed for the following discussion. The abundances of Na, Mg, Si, Ca, Ti, Cr, Fe, Ni, Y and Ba were derived in their work from high-resolution ( $R \sim 35000-48000$ ) and high signal-noise ratio spectra primarily taken with the Keck I High Resolution Echelle Spectrometer (HIRES). Most of their sample are kinematically peculiar in terms of  $R_{\text{apo}}$ ,  $Z_{\text{max}}$  and/or  $V_{\phi}$  compared to typical inner halo stars. Abundance analysis was performed in SB02 with a similar manner to the present work described in Section 3.

The abundance data of other 110 stars are taken from G03. Their sample consists of metal-poor ( $[\text{Fe}/\text{H}] < 0$ ) disk and halo stars with available accurate parallax measurements. EWs based on a high-resolution ( $R > 50000$ ) and a high quality ( $\text{S}/\text{N} > 100$ ) spectra were either measured from the data taken with the UVES at Kueyen or assembled from literature. In their work,  $T_{\text{eff}}$  and  $\log g$  were estimated from photometric data while  $\xi$  was estimated using spectroscopic data similar to this work (Section 3). Chemical abundance of O, Na, Mg, Si, Ca, Ti, Sc, V, Cr, Mn, Fe, Ni and Zn using the assembled EWs data were derived adopting these atmospheric parameters. An examination for any systematic differences in derived abundances in these works with those of the present work is performed in Section 3.6.

### 2.4. *Binary stars in the sample*

In our sample, BD+04° 2466 is a known binary from its radial-velocity variation (Jorissen et al. 2005). As noted in Z09, this star shows clear enhancements in  $[\text{C}/\text{Fe}]$ ,  $[\text{Y}/\text{Fe}]$  and  $[\text{Ba}/\text{Fe}]$ . Thus, the stellar surface abundance of this star is most likely affected by a mass transfer from an AGB companion.

BD+01° 3070 is a suspected binary whose radial velocity and an orbital solution were obtained in Carney et al. (2003). G 17-25 and G 59-27 are spectroscopic binaries having estimates of a robust orbital solution in Latham et al. (2002). Unlike BD+04° 2466, these three stars do not show anomalous  $[\text{Y}/\text{Fe}]$  and  $[\text{Ba}/\text{Fe}]$  ratios but show typical values of these ratios within a  $1\sigma$  range for each of their metallicity. Therefore, we assume that the surface abundance of these three stars is not affected by mass transfers from their binary companions.



The amplitudes of radial velocity variations of these binary stars are less than  $20 \text{ km s}^{-1}$ . Such small variations have minimal effects on the calculation of kinematics in the Galaxy within errors described in Section 2.5. Therefore, we include these stars in the following discussion assuming that their binary nature does not change the inner/outer halo classifications defined below and thus does not severely affect results on the overall nature of the inner and the outer halos.

### 2.5. Kinematics of the sample

Three-dimensional velocity components  $U$ ,  $V$  and  $W$  as well as orbital parameters including a rotational velocity with respect to the Galactic rest frame ( $V_\phi$ ), perigalactic and apogalactic distances ( $R_{\text{peri}}$  and  $R_{\text{apo}}$ ), orbital eccentricity ( $e$ ), and  $Z_{\text{max}}$  were calculated in Chiba & Beers (2000) for the Beers et al. sample and we use the same method to calculate these kinematical quantities for the Carney et al. (1994) and Ryan & Norris (1991) sample. The resulting values are tabulated in Table 2. The calculations of the orbital parameters as detailed in Chiba & Beers (2000) were performed adopting the Stäckel-type model for the Galactic potential to analytically estimate these values. We use the orbital parameters calculated in this manner for the sample taken from literature as well, instead of the published values, in order to minimize systematic effects in classifying them based on kinematics in the following discussion.

The errors in these parameters are calculated by generating a thousand of pseudo data of positions, distances and 3-dimensional velocity components whose distributions are Gaussian with dispersions equal to the observational errors of each measured quantity. For each of the pseudo data, orbital parameters are calculated as described above. The Gaussian dispersions in the resulting orbital parameters are taken as  $1 \sigma$  errors in orbital parameters in the following discussions. Median values of errors in  $e$ ,  $R_{\text{apo}}$ ,  $R_{\text{peri}}$ , and  $Z_{\text{max}}$  are 0.048, 1.8 kpc, 0.4 kpc and 1.8 kpc, respectively.

Figure 1 is the plot for the combined sample on a  $\log(Z_{\text{max}})$ - $V_\phi$  plane. The sample stars are tentatively divided into three different domains in  $V_\phi$  and two in  $Z_{\text{max}}$  in order to investigate any systematic differences in chemical abundances of the sample stars on their kinematic properties. For the  $V_\phi$  domains,  $-50 < V_\phi \leq 150 \text{ km s}^{-1}$  (*gray* symbols), is assumed to represent the range of  $V_\phi$  typical of inner halo stars, while  $V_\phi > 150 \text{ km s}^{-1}$  (*blue* symbols) and  $V_\phi \leq -50 \text{ km s}^{-1}$  (*red* symbols) include that of prograde and retrograde outliers, respectively. This classification is based on recent determinations of a modest net prograde rotation ( $0$ - $50 \text{ km s}^{-1}$  with dispersion  $\sim 100 \text{ km s}^{-1}$ ) for the inner halo stars (Chiba & Beers 2000; Carollo et al. 2007). For the  $Z_{\text{max}}$  domains,  $Z_{\text{max}} \leq 5 \text{ kpc}$  (*open* symbols) and  $Z_{\text{max}} > 5 \text{ kpc}$  (*filled* symbols) are assumed to be typical  $Z_{\text{max}}$  domains for the “inner halo” and the “outer halo” candidates. The choice of the boundary of  $Z_{\text{max}} = 5 \text{ kpc}$  is motivated by the result of Carollo et al. (2007) who showed that the average  $[\text{Fe}/\text{H}]$  for their sample stars with  $Z_{\text{max}} > 5 \text{ kpc}$  gradually shifts toward lower metallicity as stars with higher  $Z_{\text{max}}$  are selected. We note that this  $Z_{\text{max}}$  criterion

results in an inclusion of stars with kinematics typical of thick disk stars ( $Z_{\max} < 1$  kpc and  $V_\phi > 100$  km s $^{-1}$ ) in the inner  $Z_{\max}$  domain. Consequently, the sample stars are divided into the six kinematic subgroups, whose member stars are represented by different symbols in Figure 1.

Correlations between the orbital parameters for the sample stars are shown in Figure 2. The symbols are the same as the previous figure. These plots schematically illustrate whether our conventional classification of the six kinematic subgroups using  $Z_{\max}$  and  $V_\phi$  fit into kinematics of more realistic Galactic components. As shown in a  $\log Z_{\max}$ - $R_{\text{apo}}$  plane (*top-left* panel), the criterion of  $Z_{\max} = 5$  kpc as an inner/outer halo boundary results in an inclusion of stars with a wide range of  $R_{\text{apo}}$  ( $\sim 8 - 80$  kpc) in the outer  $Z_{\max}$  domain. It is also noticeable that the majority of the sample stars with  $Z_{\max} \leq 5$  kpc and  $V_\phi > 150$  km s $^{-1}$  (*blue open* symbols) have  $R_{\text{apo}} \sim 10$  kpc, which suggests that this kinematic subgroup largely includes objects belonging to the thin or thick disk component. The *top-right* panel shows a plot of the sample stars in a  $R_{\text{apo}}$ - $V_\phi$  plane. It can be seen that as the  $R_{\text{apo}}$  increases, the sample stars tend to have negative  $V_\phi$ . A plot of a Galactic rest frame velocity,  $V_{\text{RF}}$ , against the  $\log Z_{\max}$  for the sample stars is shown in the *bottom-left* panel. The plot shows that the sample stars with  $Z_{\max} > 5$  kpc currently have a wide range of  $V_{\text{RF}}$  values at the solar neighborhood. The *bottom-right* panel shows locations of the sample stars on an angular-momentum space ( $L_z$ - $L_\perp$ ), where  $L_z = RV_\phi$  and  $L_\perp = (L_x^2 + L_y^2)^{1/2}$ . For the present sample that currently resides close to the Galactic plane,  $L_\perp$  is mostly determined by  $U$  and  $W$  velocity components which are coupled with  $Z_{\max}$ . As expected, the sample stars with  $Z_{\max} > 5$  kpc predominantly reside in the region of  $L_\perp > 1000$  kpc km s $^{-1}$ .

### 3. Observation and Data Analysis

#### 3.1. Subaru HDS observation

High-resolution spectroscopy for most of the main sample was carried out on 2008 July 27 and 28 with Subaru/HDS. Wavelength range of 4030-6740Å was covered with a gap between two CCDs at  $\sim 5300 - 5480$ Å. CCD on-chip binning with  $2 \times 2$  pixels was applied for the spectra. Slit of  $0''.70$  widths is used, which yields a spectral resolution, measured as a FWHM of an emission line profile of a Th-Ar lamp spectrum, is  $R \sim 55000$  at  $\sim 5000$  Å. Additional three stars (BD+13° 2995, G 14-39 and G 20-15) were observed in 2008 June in a service program of Subaru/HDS. Positions,  $V$ -band magnitudes, total exposure time, signal-to-noise ratio and radial velocity estimates for the sample stars are summarized in Table 1.

#### 3.2. Data reduction

The raw data were reduced with standard IRAF routines. Subtraction of bias frames, flat fielding, cosmic ray rejection, background subtraction and wavelength calibration were performed for individual frames. When more than one frame are obtained, they are combined to yield a single spectrum for each star. Examples of reduced spectra, after normalized with



the fitted continuum flux, are shown in Figure 3.

### 3.3. Equivalent width measurement

Equivalent widths are measured for absorption lines in the reduced spectra by fitting a Gaussian to each feature. The absorption lines to be measured and their atomic data (the central wavelength, lower excitation potential and  $\log gf$ ) are mainly adopted from SB02. Also, we supplement the atomic data for the Mg lines, Zn lines and the lines with wavelength  $\lesssim 4500$  Å from the Vienna Atomic Line Database (Kupka et al. 2000). Additionally, we adopt one Y II line and two Mn lines from Barklem et al. (2005).

For Na lines that are weak and/or located close to the neighboring line, a direct integration was used for the EWs measurements instead of a Gaussian fitting according to the following formula:

$$EW = \int_{\lambda_{\min}}^{\lambda_{\max}} \frac{F_{\text{cont}} - F_{\text{line}}}{F_{\text{cont}}} d\lambda \quad (1)$$

where  $\lambda_{\max}$  and  $\lambda_{\min}$  are set to be at the wavelength of  $\pm 3\sigma$  of the typical Gaussian line profile in the present analysis,  $F_{\text{line}}$  and  $F_{\text{cont}}$  are a flux of the spectrum and an interpolated continuum flux at the line center, respectively. Measured EWs, the atomic data with their sources are tabulated in Table 3 (electronic version).

The errors in the equivalent widths ( $\sigma_{EW}$ ) measurements are approximated with the following formula (Cayrel 1988):

$$\sigma_{EW} \sim 1.5 \frac{\sqrt{\text{FWHM}(\Delta x)}}{S/N} \quad (2)$$

where  $\Delta x$  is a spectral dispersion in units of Å per pixel. For our sample stars, a spectral dispersion is set to  $\Delta x = 0.030$  Å at 5000 Å in the case of the  $2 \times 2$  binning was applied. As a result, provided that an FWHM in our observation is typically  $\sim 0.18$  Å and  $S/N=150-500$ ,  $\sigma_{EW}$  ranges from 0.1 to 0.7 mÅ.

The measured EWs are compared with those measured in SB02 for three stars in common (G 165–39, G 25–24 and G 188–30). For these stars, a root mean square (RMS) differences of EWs measured in the two studies is  $\sigma_{\text{rms}} < 2$  mÅ. Given that the internal errors in both measurements are in a range  $\sim 1 - 2$  mÅ, the agreement is excellent. Comparisons of EWs for these three stars are shown in Figure 4.

### 3.4. Abundance analysis

Abundance analysis was performed using an LTE abundance analysis code described in Aoki et al. (2009b). We adopt the model photosphere of Kurucz (1993) with a revised opacity distribution function (“NEWODF”, Castelli & Kurucz 2003). We used Unsöld’s (1955) treatment of van der Waal’s broadening enhanced by a factor of 2.2 in  $\gamma$  as in Ryan, Norris, & Beers (1996). Stellar atmospheric parameters are firstly determined. Then these values are

applied to obtain abundances of individual elements from measured EWs.

### 3.4.1. Stellar atmospheric parameters

Effective temperature ( $T_{\text{eff}}$ ), surface gravity ( $\log g$ ), micro-turbulent velocity ( $\xi$ ) and metallicity ( $[\text{Fe}/\text{H}]$ ) are estimated with an iterative process so that an initial guess of a set of these parameters is consistent with the resulting parameter estimates. In this analysis, we use Fe lines with  $\log(\text{EW}/\lambda) > -4.8$  to exclude strong lines that cannot be well approximated by a Gaussian profile. Note that we use stronger Fe lines in the case that only a few adequate EWs measurements are available for a sample star. The resulting values are shown in Table 4.

$T_{\text{eff}}$  was obtained from EWs of  $\lesssim 70$  Fe I lines so that a trend in derived Fe abundances from each Fe I line as a function of their excitation potentials ( $\chi$ ) is minimized. Three panels of Figure 5 show example plots of a  $\log \epsilon A$  abundance<sup>2</sup> against  $\chi$  (eV) for three stars in our sample. Each panel displays data points and a linear fit (*solid* line) to these data when the best  $T_{\text{eff}}$  estimate was applied. *Dotted* and *dashed* lines show slopes when  $T_{\text{eff}}$  is changed by an amount of the error to the positive and negative direction, respectively. Typically, magnitudes of the slopes can be minimized to  $< 0.01 \pm 0.02$  dex  $\text{eV}^{-1}$ , where an error in the slope estimate corresponds to  $T_{\text{eff}}$  of 20-100 K.

The values of  $T_{\text{eff}}$  obtained with this method are compared with those derived from a  $V - K$  color. We use  $V$  and  $K$  magnitudes from the SIMBAD database and  $E(B - V)$  values, taken from either the catalog of Beers et al. (2000) or Carney et al. (1994), those calculated iteratively in the method described in Beers et al. (2000). The  $E(B - V)$  values were used to correct the  $V$  magnitude for an interstellar extinction adopting a relation,  $A_V = R_V E(B - V)$  where  $R_V = 3.1$ . The calibration of Alonso et al. (1996) and Alonso et al. (1999) for dwarf and giant stars, respectively, are used to estimate  $T_{\text{eff}}$  from the extinction corrected  $V - K$  colors ( $(V - K)_0$ ), where  $K$ -band magnitudes are taken from the 2MASS catalog (Skrutskie et al. 2006).  $T_{\text{eff}}$  estimated using Fe I lines is lower than that estimated from  $(V - K)_0$  by  $\Delta T_{\text{eff}} \sim 150$  K on average (Figure 6). The higher  $T_{\text{eff}}$  estimates from the  $(V - K)_0$  color than those from an  $\chi - \log \epsilon A$  plot is previously reported by Lai et al. (2008). In their sample, negative trends in  $\chi - \log \epsilon A$  plot are observed when the  $T_{\text{eff}}$  derived from the  $(V - K)_0$  colors were applied for the abundance estimates.

In this work, we adopt the  $T_{\text{eff}}$  estimation from Fe I lines rather than the color temperature because this method can be reasonably applied to all of our HDS sample. Furthermore, the color temperatures are sensitive to reddening values as well as errors in photometry that are typically 0.01-0.04 mag in  $K$ -bands. Additionally, spectroscopic  $T_{\text{eff}}$  allows us calibration with other spectroscopic work such as SB02. In the later section, we show that the spectroscopic  $T_{\text{eff}}$  in this work and in SB02 reasonably agree each other. Indeed, as shown in Section 3.5, the effect of change in  $T_{\text{eff}}$  is comparable to typical errors in abundance analysis ( $\Delta[\text{X}/\text{H}] \sim 0.1$  dex) and, in most cases, is canceled out when we normalize  $[\text{X}/\text{H}]$  values with the Fe abundances.

---

<sup>2</sup>  $\log \epsilon A = \log(N_A/N_H) + 12$

$\log g$  was obtained so that the abundances derived from Fe I and Fe II are consistent within 0.02 dex. This analysis is based on an assumption that the derived abundances from neutral and ionized species should be the same. We note, however, using the estimated  $\log g$  values, the resulting abundances of Ti and Cr from their neutral and ionized species are inconsistent by 0.1-0.4 dex (Section 3.4.2).

Finally,  $\xi$  was obtained so that a trend of derived abundances from individual Fe I lines with their equivalent widths is minimized.

The derived stellar parameters are compared with those derived in SB02 for eight objects analysed in common (G 15-13, G 165-39, G 166-37, G 188-30, G 238-30, G 25-24, G 64-12 and G 64-37) and in G03 for four objects analysed in common (G 17-25 or HD 149414, G 43-3 or HD 84937, HD 111980 and HD 134439). We note that G 43-3 is supplemented to our original sample from the archival data of Subaru/HDS <sup>3</sup> in order to better examine systematic differences in derived parameters between our work and G03. The differences in each parameter (this work - literature) for the sample stars are plotted in Figure 7 and tabulated in Table 5. In each panel of Figure 7 ( $T_{\text{eff}}$ : *top-left*,  $\log g$ : *top-right*,  $\xi$ : *bottom-left* and  $[\text{Fe}/\text{H}]$ : *bottom-right*), *circles* and *triangles* represent comparisons with SB02 and G03, respectively. In Table 5, mean differences ( $\Delta_{\text{ave}}$ ) and RMS scatters ( $\sigma$ ) around the mean in each parameters are indicated for the comparisons with SB02 and G03.

As can be seen, a mean difference in  $T_{\text{eff}}$  between SB02 and this work is small (17 K) and within the errors in our temperature determination. Also, the derived  $\log g$  values in this work reasonably agree with SB02. The agreement of  $\xi$  with those derived in SB02 is excellent within scatter  $<0.2 \text{ km s}^{-1}$ .

On the other hand, the average differences in these parameters from G03 are large, mostly due to G 17-25, which is known spectroscopic binary (Latham et al. 2002). In particular, the derived  $T_{\text{eff}}$  value for G 17-25 is significantly different from that derived in G03 by  $\Delta > 400 \text{ K}$ . Such discrepancy could be due to the difference of the analysis technique that G03 used  $B - V$ ,  $b - y$  colors and a  $\text{H}_\alpha$  line profile to estimate  $T_{\text{eff}}$  while this work utilizes Fe I lines similar to SB02. Indeed, G03 reported that G 17-25 is an outlier showing significantly different  $T_{\text{eff}}$ 's estimated from  $B - V$  and  $V - K$ . Accordingly, the difference in the  $\log g$  values is large (0.49 dex) for this object. Excluding this object, the agreement with G03 is reasonable as shown in the last row of Table 5 except that  $\xi$  is lower for HD 111980 in this work by 0.67 dex from the value derived in G03.

The comparison of the  $[\text{Fe}/\text{H}]$  estimates with SB02, except for the three objects discussed below, shows that the  $[\text{Fe}/\text{H}]$  estimate in this work is systematically lower than that in SB02 up to  $\sim 0.19$  dex. This lower  $[\text{Fe}/\text{H}]$  in this work is partly due to our use of the model stellar atmosphere without assumption of convective overshooting while SB02 utilize models which

---

<sup>3</sup> Based on data collected at Subaru Telescope and obtained from the SMOKA, which is operated by the Astronomy Data Center, National Astronomical Observatory of Japan. (Baba et al. 2002)

assume the overshooting (Aoki et al. 2009b). To quantify this effect, we perform the  $[\text{Fe}/\text{H}]$  estimate using the overshooting model as in SB02. The results are plotted by open circles in the bottom-right panel of Figure 7. The resulting  $[\text{Fe}/\text{H}]$  values are higher by  $\sim 0.1$  dex than the original values and the difference from the estimate of SB02 now became small for all stars with  $[\text{Fe}/\text{H}] < -2$ . On the other hand, the 3 objects (G 15-13, G 166-37 and G 188-30) show higher  $[\text{Fe}/\text{H}]$  values in this work than in SB02 by up to 0.2 dex. Since all of these stars show low  $\xi$  values, we suspect that different modelings for a line broadening in this work and in SB02 are responsible for the  $[\text{Fe}/\text{H}]$  discrepancies. The  $[\text{Fe}/\text{H}]$  is in good agreement with G03 except for G 17-25, whose adopted other stellar parameters are significantly different from those of G03.

### 3.4.2. Abundance

The abundances of Na, Mg, Si, Ca, Ti, Mn, Fe, Ni, Zn, Y and Ba for each star are calculated adopting the stellar parameters estimated above. The abundance estimated from individual lines are averaged over a number of detected lines. This value of  $\log \epsilon A$  is normalized with the solar abundances ( $\log \epsilon A_{\odot}$ ) (Grevesse et al. 1996), which yields a value of  $[\text{X}/\text{H}]$  for each species. The derived abundances in  $[\text{X}/\text{H}]$ , errors ( $\sigma$ ) and number of lines ( $N$ ) used in the abundance estimates are tabulated in Table 6-8. In Table 9 and 10, Fe-normalized abundance ratios relative to solar one,  $[\text{X}/\text{Fe}]$ , are listed.

For the element for which both neutral and singly-ionized species are detected for a single element, we took an average of abundances derived from individual species weighted by the variance of the mean for each species to get the  $[\text{X}/\text{Fe}]$  values.

We note that a large discrepancy between Cr abundances obtained from lines of neutral (Cr I) and singly-ionized (Cr II) species is observed for our main sample as illustrated in Figure 8. In this figure, the upper panel shows Cr abundances obtained from Cr II lines ( $[\text{Cr II}/\text{H}]$ ) as a function of those obtained from Cr I lines ( $[\text{Cr I}/\text{H}]$ ). The lower panel shows differences in the two estimates ( $[\text{Cr II}/\text{Cr I}]$ ) as a function of  $[\text{Cr I}/\text{H}]$ . In our main sample,  $[\text{Cr}/\text{Fe}]$  ratios estimated from Cr I are lower than those estimated from Cr II by 0.24 and 0.36 dex on average in the metallicity range  $-2 < [\text{Fe}/\text{H}] \leq -1$  and  $-3 < [\text{Fe}/\text{H}] \leq -2$ , respectively. In most cases, Cr abundances derived from Cr I are assigned more weight than those from Cr II in this study, because a larger number of lines are detected yielding a smaller variance of the mean for Cr I. Such discrepancy was already reported for metal-poor stars with  $-4 < [\text{Fe}/\text{H}] < -2$  studied by Lai et al. (2008). Sobeck et al. (2007) suggest that the discrepancy is possibly due to a NLTE effect which corresponds to over ionization of Cr I, although an exact cause of this phenomenon is still unclear. The discrepancy also presents in our subsample taken from literature (SB02 and G03).

Similarly, Ti abundances estimated from lines of neutral (Ti I) and ionized (Ti II) species are different by  $\sim 0.25$  dex on average, as illustrated in Figure 9. Such a discrepancy could be minimized if  $\log g$  was adopted so that the Ti I and Ti II lines yield similar Ti abundances as

was performed by SB02. Therefore, a caution must be needed when comparing the [Cr/Fe] and [Ti/Fe] abundance results in this study with those from literature (Section 3.6).

For Mn and Ba abundances, the hyper-fine structure (HFS) was taken into account in the abundance calculation. The data on the HFS of Mn I lines are taken from Kurucz & Bell (1995)<sup>4</sup>. For the HFS of Ba, the line list of McWilliam (1998), assuming the isotopic abundance of r-processes estimated for the solar system, was used.

### 3.5. Error estimate

For given  $T_{\text{eff}}$ ,  $\log g$  and  $\xi$  values, uncertainties in abundances ( $\log \epsilon A$ ) are taken as RMS line-to-line scatter (standard deviation :  $\sigma_{\log \epsilon A}$ ) of abundances estimated from individual lines as divided by a square-root of the number of lines detected for the species. In the case of only one or two line are detected for a particular element, the uncertainties are taken to be equal to  $\sigma_{\log \epsilon A(\text{FeI})}$  for that sample star. The values of  $\sigma_{\log \epsilon A(\text{FeI})}$  is typically 0.05-0.1 dex. Thus, the error in an average of Fe abundances derived from each of  $< 70$  Fe I lines results in 0.01-0.02 dex. Using these abundance errors, errors for abundance ratios [X/H] are calculated as a square root of the quadratic sum of the abundance errors and the errors in the Solar abundance. For the Fe-normalized ratio [X/Fe], the error is a square root of the quadratic sum of errors in [X/H] and [Fe/H]. The errors are tabulated along with abundances in Table 6-10.

A largest contribution to uncertainties in derived [X/H] is expected to be due to errors in adopted stellar atmospheric parameters. In order to estimate uncertainties accompanied by this effect, changes in abundances caused by change in adopted stellar parameters are examined for two stars of our main sample. Figure 10 illustrates abundance deviation ( $\Delta[X/H]$ ) for a dwarf (G 275-11) and a giant star (HD 111980) in our sample when stellar atmospheric parameters  $T_{\text{eff}}$  (*top*),  $\log g$  (*middle*) and  $\xi$  (*bottom*) are changed by  $\pm 100\text{K}$ ,  $\pm 0.3$  dex and  $\pm 0.3$  km s<sup>-1</sup>, respectively. In most cases,  $\Delta[X/H]$  is less than  $\sim 0.1$  dex, which is comparable to or larger than the errors estimated from the line-to-line scatter. However, such abundance deviations tend to be canceled out when they are expressed as a ratio to the [Fe/H]. The largest deviation,  $\Delta[X/H] \sim 0.15$  dex, is found for [Ba/H] when  $\xi$  is changed by  $\pm 0.3$  km s<sup>-1</sup>. From these consideration, a maximum error of 0.15 dex for Ba and 0.1 dex for other elements should be taken into account in interpreting the abundance results. Systematic errors in the analysis method are checked by comparing the abundances in this work with those obtained in Z09 for 26 stars independently analyzed in both works. RMS differences in the [X/Fe] ratios for these objects are in the ranges of 0.07 to 0.14, that are similar to the internal errors discussed above.

---

<sup>4</sup> The HFS lists are available at <http://kurucz.harvard.edu/LINELISTS/GFHYP100/>

### 3.6. Cross calibration for the abundance ratios with literature

The derived abundances for the main sample (Section 2.1) and the reanalyzed sample (Section 2.2) are combined with samples from SB02 and G03 as described in Section 2.3, which includes smaller  $Z_{\max}$  stars. Systematic differences arising from differences in the analysis procedures are checked using sample stars commonly analyzed in this work and the literature. Figure 11 shows the differences in derived abundance ratios between those in the literature and in this work.

In this work, eight stars are analyzed in common with SB02 (*circles* in Figure 11, Mn and Zn have not been measured in SB02) as mentioned in Section 3.4.1. For most of the elements analyzed, derived abundance ratios in SB02 are in reasonable agreement with this work within the errors of the measurements, except for Na, Cr and Ba. This work derived lower [Na/Fe], [Cr/Fe] and [Ba/Fe] ratios by 0.16 dex on average than in SB02. The discrepancy in [Na/Fe] ratios in this work and in SB02 is most likely due to the weakness of the measured lines, whose EWs are typically  $< 10\text{\AA}$  and thus, abundance errors of  $\sim 0.2$  dex is expected in our analysis. The discrepancy in [Cr/Fe] is also expected from the large errors in abundance ratios caused by taking average of [Cr/H] derived from neutral and ionizing species of Cr ([Cr I/H] and [Cr II/H], respectively) that are systematically different as described in Section 3.4.2. Such discrepancy is also seen in the sample of SB02 as well. The final [Cr/H] is derived by taking weighted average of [Cr I/H] and [Cr II/H]. In this analysis, difference in the weighting factors, which is determined by the number of lines for each species, between present work and SB02 may cause the large scatter in final abundances. The lower [Ba/Fe] could be due to the hyper fine structure of Ba lines considered in this work. Except for these three elements, the mean difference for each element is less than 0.12 dex.

For the four stars (G 17-25, G 43-3, HD 111980 and HD 134439) analysed in common with G03 (*triangles* in Figure 11, Y and Ba have not been measured in G03), large discrepancies in [Na/Fe] and [Si/Fe] are found for G 17-25 (spectroscopic binary), for which we reported in Section 3.4.1 that the large discrepancies in derived stellar parameters are seen; G03 adopted  $T_{\text{eff}} = 5080$  K estimated from a  $B - V$  color and [Fe/H] =  $-1.34$  while this work adopted a spectroscopic  $T_{\text{eff}}$  of 5515 K and [Fe/H] =  $-0.91$  (Table 5). Apart from this object, an agreement is good on average within 0.12 dex except for Zn. We note that this systematic offset in Zn could cause an artificial difference in abundance between the inner and the outer halo samples since most of the outer halo stars came from our observation while the inner halo sample mostly came from G03. In particular, small systematic offset (0.09 dex) in [Mg/Fe] ratio, which is one of the most important key  $\alpha$  elements for the comparison between different halo populations, should be considered in interpreting the final result. We note that another  $\alpha$  element abundance, [Ca/Fe], shows a good agreement between the two works.



## 4. Results

In the following subsections, we show the resulting abundance ratios ( $[X/Fe]$ ) for all sample stars described in Section 2. For the sample stars from literature, the  $[X/Fe]$  values are taken from published values, assuming that any systematic differences in derived  $[X/Fe]$  ratios by different methods are sufficiently small compared to the typical errors in the  $[X/Fe]$  in this work ( $\sim 0.1$  dex). We caution that abundances of some elements, especially for Na, Cr, Ba, etc. strongly depend on various assumptions employed in different analysis methods, such as treatment of NLTE effects. In the following, we present results from our LTE abundance analysis and do not apply the correction for the NLTE effects.

For clarity, we refer the subsets of the sample with  $Z_{\max} \leq 5$  kpc and  $Z_{\max} > 5$  kpc as “*inner halo sample*” and “*outer halo sample*”, respectively. Since the proposed inner and outer halo components broadly overlap each other (Carollo et al. 2007), the boundary of  $Z_{\max} = 5$  kpc is set as a conventional criterion and, therefore, does not necessary reflect the realistic natures of these components. We discuss the validity of this conventional criterion in Section 5.2.

### 4.1. $[Fe/H]$ - $[X/Fe]$ relations

Figures 12-15 show the  $[X/Fe]$  ratios as a function of  $[Fe/H]$  for all sample stars described in Section 2. As introduced in Figure 1, the inner and the outer halo samples are represented by *open* and *filled* symbols while the colors of the symbols display their rotational motions (*gray* for  $-50 < V_\phi \leq 150$  km s $^{-1}$ , *blue* for  $V_\phi > 150$  km s $^{-1}$  and *red* for  $V_\phi \leq -50$  km s $^{-1}$ ). Shaded regions in Figure 12-15 show an average and  $1\sigma$  scatter of  $[X/Fe]$  for the sample stars having typical inner halo kinematics, estimated within each metallicity interval with widths of  $\Delta[Fe/H] = 0.5$  dex. Here, the typical inner halo kinematics is assumed to be  $Z_{\max} \leq 5$  kpc and  $-50 < V_\phi \leq 150$  km s $^{-1}$  as described in Section 2.5, for which the sample stars are represented by the *gray open* circles in the figures.

Average  $[X/Fe]$  values and their errors ( $\sigma/\sqrt{N}$ ) for the inner and the outer halo samples within each of four metallicity intervals are summarized in Table 11. In this table, the values are shown only for domains whose number of sample stars exceeds 1.

#### 4.1.1. $\alpha$ -elements; Mg, Si, Ca, Ti

Figure 12 shows four  $\alpha$ -elements (from *top-left* to *bottom-right*, Mg, Si, Ca, Ti) to iron ratios as a function of  $[Fe/H]$ .

The most prominent feature in this figure is that a discrepancy in the  $[Mg/Fe]$  between the inner and the outer halo samples is seen in the metallicity interval of  $-2 < [Fe/H] < -1$ . Specifically, the average  $[Mg/Fe]$  ratio of the outer halo sample is lower than the inner one by 0.11 dex as summarized in Table 11. This tendency of the lower  $[Mg/Fe]$  ratios is seen among all  $V_\phi$  domains for the outer halo sample. The lower  $[Mg/Fe]$  ratios for the outer halo are not seen among more metal-poor stars with  $[Fe/H] < -2$ . Instead, a large scatter in  $[Mg/Fe]$  for the outer halo sample, spanning a range in  $[Mg/Fe]$  of  $\sim 0.1$ -0.8 dex, is evident compared to the

inner one. Among stars with  $[\text{Fe}/\text{H}] > -1$ , one outer halo star has the lowest  $[\text{Mg}/\text{Fe}]$  value. Apparent clustering of sample stars at  $-1 < [\text{Fe}/\text{H}] < 0$  and  $[\text{Mg}/\text{Fe}] \sim 0.3-0.5$  is predominantly occupied by the inner halo sample having significant prograde rotation (*open blue* circles), which is typical of thick-disk stars. It is remarkable that these  $[\text{Mg}/\text{Fe}]$  ratios in each  $[\text{Fe}/\text{H}]$  interval for the outer halo sample show a clear gradient in  $[\text{Mg}/\text{Fe}]$  with  $[\text{Fe}/\text{H}]$  as opposed to the inner halo sample, which shows constant mean  $[\text{Mg}/\text{Fe}]$ . This result confirms the recent  $\alpha$  abundance estimate by Z09 using a subset of the sample in the present work.

The  $[\text{Si}/\text{Fe}]$  and  $[\text{Ca}/\text{Fe}]$  ratios tend to be lower for the outer halo sample in the metallicity range of  $-2 < [\text{Fe}/\text{H}] < -1$  as seen in the  $[\text{Mg}/\text{Fe}]$  ratios but by smaller degree. In the  $[\text{Si}/\text{Fe}]-[\text{Fe}/\text{H}]$  plot, the large scatters can be attributed in part to the Si lines used in our sample, which are typically weak ( $< 30 \text{ m}\text{\AA}$ ). Since no Si lines were detected in more metal-poor stars, we could not derive any conclusion on the  $[\text{Si}/\text{Fe}]$  behaviors in the metallicity  $[\text{Fe}/\text{H}] < -2$ . The  $[\text{Ca}/\text{Fe}]$  ratios show a relatively tight correlation with  $[\text{Fe}/\text{H}]$  compared to the other  $\alpha$ -elements among both the inner and the outer halo samples. Specifically, both samples show decreasing trend in  $[\text{Ca}/\text{Fe}]$  with increasing  $[\text{Fe}/\text{H}]$  in all metallicity ranges.

Difference in the  $[\text{Ti}/\text{Fe}]-[\text{Fe}/\text{H}]$  relation between the inner and the outer halo sample is not clear, except that a significant scatter in the  $[\text{Ti}/\text{Fe}]$  ratios for  $[\text{Fe}/\text{H}] < -2$  is evident among the outer halo sample. It is also noticeable that the decreasing trends of  $[\text{X}/\text{Fe}]$  with increasing  $[\text{Fe}/\text{H}]$  seen in Mg, Ca and Si are not evident for the  $[\text{Ti}/\text{Fe}]$  ratios for the outer halo sample.

We discuss in Section 4.2 in detail for this dependence of abundance ratios on the orbital parameters.

#### 4.1.2. Na

Figure 13 shows the  $[\text{Na}/\text{Fe}]$  as a function of  $[\text{Fe}/\text{H}]$  for the sample stars.

Na abundances are estimated in this work from Na I doublet lines at  $5682/5688 \text{ \AA}$  and  $6154/6160 \text{ \AA}$ . These lines are typically weak in metal-poor stars ( $\lesssim 20 \text{ m}\text{\AA}$ ) and are less affected by NLTE effects, which are prominent in stronger resonance lines (Baumuller et al. 1998; Andrievsky et al. 2007). NLTE calculations by Takeda et al. (2003) reported that a LTE analysis using these lines can overestimate Na abundances by 0.05-0.14 dex. This amount of correction is comparable to typical abundance errors in this work ( $\sim 0.1$  dex). Thus, we do not apply the NLTE correction to the resulting Na abundances.

Derived  $[\text{Na}/\text{Fe}]$  ratios show a large scatter ( $\sim 0.15-0.20$  dex) for both of the inner and the outer halo samples. The modest difference in the  $[\text{Na}/\text{Fe}]$  ratios between the two samples is seen in the metallicity interval of  $-2 < [\text{Fe}/\text{H}] < -1$ , such that an average of the  $[\text{Na}/\text{Fe}]$  ratios for the outer halo sample ( $\mu = -0.31$  dex) is lower than the inner one by more than 0.2 dex (Table 11). This lower average  $[\text{Na}/\text{Fe}]$  ratio for the outer halo sample is similar to the value obtained among stars with high rest frame velocity,  $V_{\text{RF}} > 300 \text{ km s}^{-1}$ , in Fulbright (2002), where the mean  $[\text{Na}/\text{Fe}]$  is  $-0.34$  for the same metallicity interval. The lower  $[\text{Na}/\text{Fe}]$  was also reported for three  $\alpha$ -poor halo stars in Ivans et al. (2003).

#### 4.1.3. Fe-peak element; Cr, Mn, Ni, Zn

Figure 14 shows the abundance ratios for Cr, Mn, Ni and Zn as a function of  $[\text{Fe}/\text{H}]$ . For these elements, the difference in the abundance ratios between the inner and the outer halo samples are not clearly seen, except for a modest depression in  $[\text{Zn}/\text{Fe}]$  for the outer halo sample.

Specifically, trends in  $[\text{Cr}/\text{Fe}]$  with  $[\text{Fe}/\text{H}]$  for the inner and the outer halo samples are almost indistinguishable for the metallicity  $[\text{Fe}/\text{H}] > -2$ . In this metallicity range, both of the inner and the outer halo samples approximately show the solar value, 0.0 dex, with a small scatter of 0.1 dex. In the lower metallicity range, the outer halo sample shows a slightly decreasing trend with decreasing  $[\text{Fe}/\text{H}]$  with a relatively large scatter (0.14 dex).

The average  $[\text{Ni}/\text{Fe}]$  ratios for the inner and the outer halo are indistinguishable. For both samples, the  $[\text{Ni}/\text{Fe}]$  ratios are slightly higher for  $-3 < [\text{Fe}/\text{H}] < -2$  on average.

For the  $[\text{Mn}/\text{Fe}]$  ratios, the outer halo sample shows an increasing trend with  $[\text{Fe}/\text{H}]$  similar to the inner halo sample. Mn is thought to be a product of explosive nucleosynthesis during SNe explosion. Umeda & Nomoto (2002) suggest that the trend with  $[\text{Fe}/\text{H}]$  can be explained by a higher relative contributions from a layer containing Mn in metal-rich stars rather than in metal-poor stars.

Many of the outer halo sample show  $[\text{Zn}/\text{Fe}] < 0.0$  while majority of the inner halo sample shows  $[\text{Zn}/\text{Fe}] > 0$  in all metallicity range. Interestingly, lower  $[\text{Zn}/\text{Fe}]$  ratios have been reported for the MW satellites. For example, Shetrone et al. (2001) reported that the  $[\text{Zn}/\text{Fe}]$  ratios determined for Draco, Ursa Minor and Sextans dSphs are lower than those of the Galactic halo or disk stars with  $[\text{Fe}/\text{H}] > -2$ .

#### 4.1.4. Neutron capture element; Ba, Y

Figure 15 shows  $[\text{Y}/\text{Fe}]$  and  $[\text{Ba}/\text{Fe}]$  ratios as a function of  $[\text{Fe}/\text{H}]$  for our inner and the outer halo samples. Because most of the inner halo sample with  $[\text{Fe}/\text{H}] < -2$  do not have available Y and Ba measurements, the similarity and differences between the inner and the outer halo samples for  $[\text{Fe}/\text{H}] < -2$  could not be investigated in detail in the present work. Nevertheless, major features in  $[\text{Y}/\text{Fe}]/[\text{Ba}/\text{Fe}]$  vs.  $[\text{Fe}/\text{H}]$  seen in the sample of Francois et al. (2007) without adequate kinematic parameter estimates are well reproduced with the outer halo sample plotted in Figure 15. Specifically, the  $[\text{Y}/\text{Fe}]$  ratios show an increasing trend with  $[\text{Fe}/\text{H}]$  below  $[\text{Fe}/\text{H}] \simeq -1.5$ , while it is relatively flat for more metal-rich stars. Like Y, Ba for the outer halo sample also shows an increasing trend with  $[\text{Fe}/\text{H}]$  below  $[\text{Fe}/\text{H}] \simeq -1.5$  which reaches below  $[\text{Ba}/\text{Fe}] \simeq -1$  at the lowest metallicity. We note that one of two objects having exceptionally high  $[\text{Y}/\text{Fe}]$  and  $[\text{Ba}/\text{Fe}]$  ratios is a binary star, BD+04° 2466, whose anomalous  $[\text{Ba}/\text{Fe}]$  are reported by Z09. There is no conclusive evidence of binary nature for another Y/Ba-rich star, G 18-24 (Latham et al. 2002). An order of  $\sim 1000$  scatter observed in Francois et al. (2007) sample in the metallicity interval  $-3.2 \leq [\text{Fe}/\text{H}] \leq -2.8$  was not evident in the present outer halo sample.

#### 4.1.5. Abundance pattern of the inner and the outer halo stars

As a summary of our results, Figure 16 shows abundance patterns for the inner (*open* symbols) and the outer (*filled* symbols) halo stars in the metallicity range of  $-2 < [\text{Fe}/\text{H}] < -1$ . The error bar represents a standard deviation divided by a square-root of the number of objects ( $\sigma/\sqrt{N}$ ) in each of the inner and the outer halo sample. Since these error bars do not include systematic errors, systematic differences between the different analysis methods as mentioned in Figure 11 should be taken into account when the inner and the outer halo comparison is made.

As mentioned in the previous subsections, a prominent difference between the inner and the outer halo stars with  $-2 < [\text{Fe}/\text{H}] < -1$  can be seen in the  $[\text{Mg}/\text{Fe}]$  ratio; an average  $[\text{Mg}/\text{Fe}]$  ratio is lower for the outer halo sample by 0.12 dex. Similarly, the  $[\text{Na}/\text{Fe}]$ ,  $[\text{Ca}/\text{Fe}]$ ,  $[\text{Mn}/\text{Fe}]$ ,  $[\text{Zn}/\text{Fe}]$  and  $[\text{Y}/\text{Fe}]$  ratios are apparently lower for the outer halo sample. We note that the inner halo sample is mostly from G03, and the consistency of the abundance analysis between G03 and the present work is not well confirmed (Section 3.4.1 and 3.6) The difference between inner and the outer halo is, however, supported by the gradient of  $[\text{Mg}/\text{Fe}]$ , as well as  $[\text{Ca}/\text{Fe}]$ , only found for the outer halo sample. We also note that the  $[\text{Na}/\text{Fe}]$  ratios for our outer halo sample could actually be even lower since our LTE abundance analysis could overestimate the  $[\text{Na}/\text{Fe}]$  ratios up to  $\lesssim 0.15$  dex compared to the NLTE analysis performed by G03. For other elements, the inner and the outer halo samples show indistinguishable abundance ratios in this metallicity range.

Our results highlight an necessity of increasing a statistical accuracy to conclude on any systematic differences in detailed abundance patterns for the inner and the outer halo stars. In this analysis, systematic errors that possibly arise from various sources such as model atmospheres, methods in stellar parameter estimates, atomic line data, or a treatment of NLTE effects, may mimic the intrinsic scatters on the abundance ratios. Thus, it is important to remark that a homogeneous analysis technique is essential for studying the current subject, as is attempted in the current work.

#### 4.2. Abundance as a function of kinematic parameters

##### 4.2.1. $R_{\text{apo}}\text{-}[X/\text{Fe}]$ relations

Figure 17 shows  $[\text{Mg}/\text{Fe}]$  and  $[\text{Ca}/\text{Fe}]$  (*left* and *right* panel, respectively) as a function of  $\log(R_{\text{apo}})$  for the inner ( $Z_{\text{max}} \leq 5$  kpc, *open* symbols) and the outer ( $Z_{\text{max}} > 5$  kpc, *filled* symbols) halo samples divided into four metallicity intervals; from *top* to *bottom*,  $-1.5 < [\text{Fe}/\text{H}] \leq -1.0$ ,  $-2.0 < [\text{Fe}/\text{H}] \leq -1.5$ ,  $-2.5 < [\text{Fe}/\text{H}] \leq -2.0$ ,  $[\text{Fe}/\text{H}] \leq -2.5$ . A dotted line in each panel shows an average value of  $[\text{Mg}/\text{Fe}]$  or  $[\text{Ca}/\text{Fe}]$  for the objects having typical inner halo kinematics ( $-50 < V_{\phi} \leq 150$  and  $Z_{\text{max}} \leq 5$  kpc).

The most prominent feature in the  $[\text{Mg}/\text{Fe}]$  vs.  $R_{\text{apo}}$  plot is a difference in the typical  $[\text{Mg}/\text{Fe}]$  values above and below  $R_{\text{apo}} \sim 25$  kpc ( $\log R_{\text{apo}} \sim 1.4$ ) for the highest two metallicity

intervals. Below  $R_{\text{apo}} \sim 25$  kpc, in which the inner halo sample dominates, the sample stars show high values of  $[\text{Mg}/\text{Fe}]$  up to  $\sim 0.6$  in the both two highest metallicity intervals ( $[\text{Fe}/\text{H}] > -2$ ). On the contrary, the sample having larger  $R_{\text{apo}}$  is mostly confined to  $[\text{Mg}/\text{Fe}] \lesssim 0.4$ . Such a difference above and below  $R_{\text{apo}} \sim 25$  kpc is not evident in the metallicity interval of  $-2.5 < [\text{Fe}/\text{H}] \leq -2$ . Since the sample size of both the inner and the outer halo is small, a determination for the  $[\text{Mg}/\text{Fe}]$ - $R_{\text{apo}}$  trend below  $[\text{Fe}/\text{H}] \leq -2.5$  is unavailable for the present sample.

The lower  $[\text{Mg}/\text{Fe}]$  for the larger  $R_{\text{apo}}$  is reported in SB02, in which a weak decline in  $[\alpha/\text{Fe}]$  with  $R_{\text{apo}}$  is observed for the halo stars with  $-4 < [\text{Fe}/\text{H}] < -0.5$ . A comparison of their result with the left panel of Figure 17 suggests that the decline in the  $[\text{Mg}/\text{Fe}]$  ratio observed for large  $R_{\text{apo}}$  is primarily due to the stars with  $-2 < [\text{Fe}/\text{H}] < -1$ . Within this metallicity range, the present analysis additionally suggests that  $[\text{Mg}/\text{Fe}]$  is rather constantly low at  $R_{\text{apo}} > 25$  kpc with a negligible gradient.

A main feature of the  $[\text{Mg}/\text{Fe}]$  ratio described above is also found for  $[\text{Ca}/\text{Fe}]$  but by smaller degree; consistently lower  $[\text{Ca}/\text{Fe}]$  below  $R_{\text{apo}} \sim 25$  kpc is seen for the sample over the metallicity intervals  $-2 < [\text{Fe}/\text{H}] < -1$ . In all metallicity intervals, the scatter in  $[\text{Ca}/\text{Fe}]$  is smaller than that of  $[\text{Mg}/\text{Fe}]$ .

#### 4.2.2. $Z_{\text{max}}$ - $[X/\text{Fe}]$ relations

Figure 18 shows  $[\text{Mg}/\text{Fe}]$  and  $[\text{Ca}/\text{Fe}]$  (*left* and *right* panel, respectively) as a function of  $\log(Z_{\text{max}})$  for the inner and the outer halo samples with each metallicity interval the same as in Figure 17. The symbols are the same as in previous figures.

For  $[\text{Mg}/\text{Fe}]$ , trends with  $\log(Z_{\text{max}})$  are significantly different depending on metallicity intervals. For stars with  $-1.5 < [\text{Fe}/\text{H}] \leq -1$ , the inner halo stars show a larger scatter in  $[\text{Mg}/\text{Fe}]$  ranging from  $\sim 0.2$  to  $\sim 0.7$  dex than the outer halo sample for which  $[\text{Mg}/\text{Fe}]$  values are mostly below 0.5 dex. In the metallicity interval of  $-2 < [\text{Fe}/\text{H}] \leq -1.5$ , an apparent gradient above  $Z_{\text{max}} \sim 1$  kpc is seen among the inner and outer halo samples. Below  $Z_{\text{max}} \sim 1$  kpc, the stars with  $[\text{Mg}/\text{Fe}] \gtrsim 0.4$  dominate while above  $Z_{\text{max}} > 10$  kpc, the average  $[\text{Mg}/\text{Fe}]$  reaches down to  $\sim 0.2$  dex. In the metallicity interval  $-2.5 < [\text{Fe}/\text{H}] \leq -2$ , a large scatter in the  $[\text{Mg}/\text{Fe}]$  ranging from  $[\text{Mg}/\text{Fe}] \sim 0.1$  to  $\sim 0.7$  dex is seen for the outer halo sample but not for the inner halo sample. The large scatter for the outer halo sample is even more prominent in the lowest metallicity  $[\text{Fe}/\text{H}] \leq -2.5$ .

For  $[\text{Ca}/\text{Fe}]$ , a modest gradient with  $\log(Z_{\text{max}})$  is seen in the metallicity interval  $-2 < [\text{Fe}/\text{H}] \leq -1.5$  like that seen in  $[\text{Mg}/\text{Fe}]$ .

#### 4.3. Dependence on $V_\phi$ for $[\text{Mg}/\text{Fe}]$ and $[\text{Ca}/\text{Fe}]$

Carollo et al. (2007) suggest that the MW outer halo is characterized by a net retrograde rotation ( $\langle V_\phi \rangle < 0$  km s $^{-1}$ ) relative to the Galactic rest frame. This result implies that the sample stars with a retrograde rotation are more adequate representatives of the actual outer halo population rather than those with prograde rotation.

In order to examine possible dependence on  $V_\phi$  for abundance ratios, Figure 19 plots average  $[\text{Mg}/\text{Fe}]$  (*top*) and  $[\text{Ca}/\text{Fe}]$  (*bottom*) for the kinematic subgroups defined by  $V_\phi$  and  $Z_{\text{max}}$  for each metallicity interval. *Square*, *circle* and *triangle* correspond to  $V_\phi > 150 \text{ km s}^{-1}$ ,  $-50 < V_\phi \leq 150 \text{ km s}^{-1}$  and  $V_\phi \leq -50 \text{ km s}^{-1}$ , respectively. The *open* and the *filled* symbols represent the sample with  $Z_{\text{max}} \leq 5 \text{ kpc}$  and  $Z_{\text{max}} > 5 \text{ kpc}$ , corresponding to the inner and the outer halo sample, respectively. The error bars show standard deviations of the  $[\text{Mg}/\text{Fe}]$  ratios in each metallicity interval and the kinematic subgroup divided by a square-root of a number of the sample stars averaged over.

In the metallicity interval of  $-2 < [\text{Fe}/\text{H}] < -1$ , it is noticeable that the average  $[\text{Mg}/\text{Fe}]$  ratio for the outer halo sample with significant retrograde rotation,  $V_\phi \leq -50 \text{ km s}^{-1}$ , is slightly lower than the other two  $V_\phi$  subgroups. This can be interpreted as the objects with significant retrograde rotation are more likely belonging to the outer halo, which is thought to be formed with a different mechanism from the inner halo (Carollo et al. 2007). The  $[\text{Ca}/\text{Fe}]$  ratios are almost indistinguishable between the three  $V_\phi$  domains. In generally, the present sample with  $-2 < [\text{Fe}/\text{H}] < -1$  does not show significant difference in the  $[\text{Mg}/\text{Fe}]$  and  $[\text{Ca}/\text{Fe}]$  ratios between the different  $V_\phi$  ranges, while the abundance difference is more evident between the inner and the outer halos as defined by below and above  $Z_{\text{max}} = 5 \text{ kpc}$  in this study.

#### 4.4. Kinematics of the low- $[\text{Mg}/\text{Fe}]$ stars

Four panels of Figure 20 show correlations of the orbital parameters similar to Figure 2 but now stars with  $[\text{Mg}/\text{Fe}] < 0.2$  (hereafter “low- $[\text{Mg}/\text{Fe}]$  stars”) are highlighted with open triangles. Only sample stars with  $-2 \leq [\text{Fe}/\text{H}] \leq -1$  are plotted in the figure.

In the  $Z_{\text{max}}\text{-}R_{\text{apo}}$  plane (*top-left* panel), almost all low- $[\text{Mg}/\text{Fe}]$  stars reside in the region,  $5 < Z_{\text{max}} < 25 \text{ kpc}$  ( $0.7 < \log Z_{\text{max}} < 1.4$ ), except one star at  $Z_{\text{max}} < 5 \text{ kpc}$ . The low- $[\text{Mg}/\text{Fe}]$  stars distribute over a wide range in  $R_{\text{apo}}$  such that  $R_{\text{apo}} \sim 10 - 65 \text{ kpc}$ . The *top-right* panel shows a distribution of the sample stars in a  $R_{\text{apo}}\text{-}V_\phi$  plane. In the range  $R_{\text{apo}} < 20 \text{ kpc}$ , most low- $[\text{Mg}/\text{Fe}]$  stars reside around  $V_\phi \sim 0 \pm 100 \text{ km s}^{-1}$ . At higher  $R_{\text{apo}}$ , the low- $[\text{Mg}/\text{Fe}]$  stars tend to have a retrograde orbit. The *bottom-left* panel shows the distribution of the sample stars in a  $Z_{\text{max}}\text{-}V_{\text{RF}}$  plane. Fulbright (2002) reported that, based on chemical abundance analysis for a large sample of  $> 70$  disk and halo stars,  $[\text{Mg}/\text{Fe}]$  ratios are lower by  $\sim 0.2$  dex for the objects with  $V_{\text{RF}} > 300 \text{ km s}^{-1}$ . The lower  $[\text{Mg}/\text{Fe}]$  ratios for  $V_{\text{RF}} > 300 \text{ km s}^{-1}$  stars are also seen in the  $Z_{\text{max}}\text{-}V_{\text{RF}}$  plot in Figure 20. Specifically, 27% of sample stars with  $V_{\text{RF}} > 300 \text{ km s}^{-1}$  are low- $[\text{Mg}/\text{Fe}]$  stars while this fraction drops for lower  $V_{\text{RF}}$  stars: 13% and 0 % for  $150 < V_{\text{RF}} \leq 300 \text{ km s}^{-1}$  and  $V_{\text{RF}} \leq 150 \text{ km s}^{-1}$ , respectively.

In the angular momentum  $L_z\text{-}L_\perp$  space (*bottom-right* panel), low- $[\text{Mg}/\text{Fe}]$  stars predominantly reside at  $L_\perp \gtrsim 600 \text{ kpc km s}^{-1}$ . In the  $L_z\text{-}L_\perp$  plane, Helmi et al. (1999) identified a kinematic substructure (H99 stream), for which several other studies confirmed the presence of a similar structure (Chiba & Beers 2000; Kepley et al. 2007). Recently, Klement et al. (2009)



suggest that, for 21 candidate members of the H99 stream, the  $[\text{Fe}/\text{H}]$  distribution peaks at  $[\text{Fe}/\text{H}] \approx -2.0$ . Figure 21 is the same as the *bottom-right* panel of Figure 20, except that the metallicity range is now set to  $-2.5 < [\text{Fe}/\text{H}] < -1.5$  which is comparable to the suggested metallicity distribution of the H99 stream. In a region containing the reported location of the H99 stream in the  $L_z$ - $L_\perp$  plane ( $L_\perp \approx 2000$  and  $L_z \approx 500$ - $1500$  kpc km s $^{-1}$ ), no low- $[\text{Mg}/\text{Fe}]$  stars are included and span  $[\text{Mg}/\text{Fe}]$  ratios of  $\sim 0.23 - 0.52$ . Whether these stars represent abundances of this kinematic substructure is quite uncertain in the present sample because of the small sample size and the incomplete sample selection. Future systematic observations for robust kinematics and chemical abundances of halo stars including fainter objects may be required to address whether such kinematic substructures have distinct chemical abundances compared to stars in the smooth halo component.

## 5. Discussion

### 5.1. Comparison with recent studies of abundances and kinematics for the halo stars

Previous studies for the possible dependence of detailed chemical abundances of solar-neighborhood stars on their kinematics have provided important implications for early formation of the MW (e.g., Nissen & Schuster 1997; Hanson et al. 1998; Fulbright 2002; SB02; Gratton et al. 2003b; Roederer 2008). In our work, a primary improvement compared with previous studies is the inclusion of a large number of stars with  $Z_{\text{max}} > 5$  kpc. This improvement has the following advantages that 1) abundance-kinematics correlation can be examined by finely dividing the sample into small metallicity intervals and 2) systematic abundance difference between the assumed inner/outer components can be investigated covering a larger number of the outer halo sample, not restricted to a few stars with extreme orbital properties.

SB02 conducted an abundance analysis of high-resolution and high signal-to-noise spectra for halo stars, most of which have extreme kinematic properties such as a large  $R_{\text{apo}}$ , a large  $Z_{\text{max}}$  or an extreme retrograde orbit ( $V_\phi < 0$  km s $^{-1}$ ). They showed that the  $[\alpha/\text{Fe}]$  ratios are lower for large  $R_{\text{apo}}$  stars at a given metallicity without clear connection with both of  $Z_{\text{max}}$  and  $V_\phi$ . Their result for the dependence of the  $[\alpha/\text{Fe}]$  ratios on  $R_{\text{apo}}$  and  $V_\phi$  is indeed reproduced in this work with a much larger number of sample in each metallicity interval. Specifically, our results suggest that stars with  $R_{\text{apo}} > 25$  kpc have lower  $[\text{Mg}/\text{Fe}]$  ratios, which are a main contributor to  $[\alpha/\text{Fe}]$ -kinematics correlation, primarily in the metallicity  $[\text{Fe}/\text{H}] > -2$  (Figure 17) without showing a clear dependence on  $V_\phi$  (Figure 19). Our result also suggests that  $[\text{Mg}/\text{Fe}]$  ratios are lower for large  $Z_{\text{max}}$  stars as well, as found by increasing the number of the sample stars with  $Z_{\text{max}} > 5$  kpc (Figure 18). This feature additionally highlights the importance of examining abundance-kinematics correlations within each metallicity interval rather than including all stars with  $[\text{Fe}/\text{H}] < -1$ , since the correlation could be significantly different depending on a given metallicity.

Another important improvement in the present work is that the sample of all 57 halo stars, most of which have outer halo kinematics, were observed with similar settings and analyzed in a homogeneous manner. The homogeneous analysis allows us the examination of intrinsic scatter of the outer halo sample without been significantly affected by systematic errors. Recently, Roederer (2008) used a large sample of abundances and kinematics assembled from literature to investigate any systematic trends in abundances with their kinematic properties. Although more stringent criteria for the inner and the outer halo stars were employed, each domain largely overlaps with the simple classification employed in the present work. A consistent result is obtained in both works that the  $[\text{Mg}/\text{Fe}]$  in the intermediate metallicity range is lower for the outer halo stars than for the inner halo stars. A larger scatter in the  $[\text{Ni}/\text{Fe}]$  for the outer halo than the inner halo reported in Roederer (2008) is not reproduced in the present work. This feature implies that the reported large scatter in  $[\text{Ni}/\text{Fe}]$  may be partly attributed to the systematic errors among the different abundance analyses. Nevertheless, the present work does not properly cover the metallicities below  $[\text{Fe}/\text{H}] < -3$  yet. More investigation is needed to conclude on the inner/outer difference in a scatter of  $[\text{Ni}/\text{Fe}]$  at lowest metallicity.

### 5.2. *The inner/outer halo boundary in terms of the abundance ratios*

As can be seen in the previous sections, setting the conventional inner/outer halo boundary as being  $Z_{\text{max}} = 5$  kpc results in systematic difference in  $[\text{Mg}/\text{Fe}]$ , and also in  $[\text{Si}/\text{Fe}]$  and  $[\text{Ca}/\text{Fe}]$  with a smaller degree, between these two halo components in the metallicity range of  $-2 < [\text{Fe}/\text{H}] < -1$ . Validity of setting  $Z_{\text{max}} = 5$  kpc as the likely inner/outer halo boundary is examined by applying the different boundary values of  $Z_{\text{max}} = 3$  and 10 kpc as well. In order to illustrate this examination, Figure 22 shows differences in cumulative  $[\text{Mg}/\text{Fe}]$ ,  $[\text{Si}/\text{Fe}]$ ,  $[\text{Ca}/\text{Fe}]$  and  $[\text{Ti}/\text{Fe}]$  distributions for the assumed inner/outer halo by setting different  $Z_{\text{max}}$  boundaries (3, 5, 10 kpc). Only stars with the metallicity range of  $-2 < [\text{Fe}/\text{H}] < -1$  are included in this analysis. Table 12 summarizes Kolmogorov-Smirnoff (K-S) probabilities for the inner/outer halo division in terms of the four  $\alpha$  elements (column 2-5) with the adopted  $Z_{\text{max}}$  boundaries (column 1). For Mg, whose discrepancy between the inner/outer halo is prominent, the change in the boundary within  $Z_{\text{max}} = 3-10$  kpc does not largely alter the conclusion. More specifically, Table 12 shows that, regardless of the different choices of the boundaries, K-S tests for the assumed inner/outer halo  $[\text{Mg}/\text{Fe}]$  distributions disprove the null hypothesis that the two distributions are drawn from the same distribution at  $P_{\text{KS}} < 0.01$ . For Ca, discrepancy such that  $P_{\text{KS}} < 0.01$  is observed if the boundary of  $Z_{\text{max}} = 3$  or 5 kpc is set. On the other hand, for Si and Ti, a K-S test cannot disprove the null hypothesis at  $P_{\text{KS}} < 0.01$  for any choice of the boundaries. Especially, the assumed inner/outer halo are indistinguishable in terms of  $[\text{Ti}/\text{Fe}]$ .

These results suggest that, regarding the present sample, the inner/outer halo transitions in a vertical direction are rather continuous in terms of Mg, Si, Ca and Ti abundance ratios in the range of  $Z_{\text{max}} = 3-10$  kpc. A sharp boundary within this vertical range is not prominent

in the present analysis. It can be noticed, however, that for Mg, the choice of the boundary as  $Z_{\max} = 10$  kpc results in an inclusion of a large number of low [Mg/Fe] stars in the inner domain. This feature suggests that the low [Mg/Fe] stars progressively contribute to the stellar halo at  $Z_{\max} > 5$  kpc. Therefore, the present analysis implies that the properties (IMFs, star-formation timescale, etc.) of the progenitor system, either *in situ* or accreted dwarf galaxies, that contribute to build up the stellar halo, start to change at a vertical distance less than 10 kpc.

Whether there exists a boundary above which a spatial distribution, kinematics and chemical abundances are distinct from the inner halo is still unclear. From a large data set of positions, distances and full space motions for the solar-neighborhood halo stars, Carollo et al. (2007) report an increasing contribution from a stellar component with lower peak metallicity ( $[\text{Fe}/\text{H}] \sim -2.2$ ) and a net retrograde rotation as increasing  $Z_{\max}$  above 5 kpc. This change in characteristic metallicity and rotational motion supports the suggestion obtained in this work from the elemental abundances that dominant progenitors may be different between the inner and the outer halos. It is, however, uncertain in both works whether a transition from the inner to the outer halo is sharp or continuous in terms of metallicity, rotational motion and the elemental abundances. This issue should be addressed with the expanded homogeneous data set of full phase-space information as well as elemental abundances for fainter objects not restricted to the local volume.

It can also be seen from Figure 22 that a degree of the inner/outer halo distinction varies with elements. Mg, Si, Ca and Ti, are conventionally referred to as  $\alpha$ -elements because these are thought to be all produced through similar mechanisms (captures of  $\alpha$  particles). However, the present analysis shows that the degree to which the assumed inner/outer halo are different is large for Mg but negligible for Ti. This discrepancy could partly be due to different production mechanisms for Mg and Ti (Woosley & Weaver 1995), e.g., Mg is mostly produced with hydrostatic burning while dominant Ti is produced during supernovae explosions.

### 5.3. Comparison with the nearby dSphs; possible progenitors of the outer halo stars

We now consider the properties of the possible progenitor systems of the outer halo, whose candidate members show lower [Mg/Fe] than those of the inner halo in this work. These progenitor systems are thought to contribute to a large fraction of the MW halo according to the currently standard  $\Lambda$ CDM model. Although it is now broadly believed that the accretions of smaller progenitor systems have played an important role in making up the MW stellar halo, the properties of the progenitor systems such as a typical size, mass, stellar/gas content, star formation histories are still controversial.

One probable candidate as a dominant progenitor system of the MW halo is a system similar to the dSphs currently orbiting the MW halo. In addition to  $\sim 10$  dSphs previously known (sometimes called “classical” dSph),  $\sim 12$  dSphs, most of which are fainter than  $\sim 10^5 L_{\odot}$ ,

have been newly discovered through the SDSS (Belokurov et al. 2007; Willman et al. 2005). In the following subsections, the possibility that systems similar to these dSphs could be the dominant progenitor of the MW halo by examining similarity in chemical abundance patterns of constituent stars in both systems.

### 5.3.1. Abundance overlap with “Classical” dSphs

Abundance analyses for red giant stars belonging to the relatively bright MW satellites, Ursa Minor, Sculptor, Draco, Sextans, Carina, Fornax and Leo I, are available from high-resolution spectroscopy (e.g., Shetrone et al. 2001; Shetrone et al. 2003; Tolstoy et al. 2003; Geisler et al. 2005; Koch et al. 2008a; Aoki et al. 2009a). A comparison of a detailed abundance pattern for our outer halo sample with these satellites, so called “Classical” dSphs, provides implications about whether any of the outer halo sample could have once belonged to systems similar to these dSphs. It was reported that the chemical abundance patterns for these dSphs are distinct compared to the bulk of the Galactic stars at a given metallicity range in that the  $[\alpha/\text{Fe}]$  ratios are lower for the dSphs (Venn et al. 2004). Slightly lower  $[\text{Zn}/\text{Fe}]$  and  $[\text{Y}/\text{Fe}]$  for the dSphs than the halo stars is also reported (Shetrone et al. 2003).

Figure 23 compares the distributions of the  $[\text{X}/\text{Fe}]$  abundance ratios determined for the MW dSphs by Shetrone et al. (2001); Shetrone et al. (2003); Geisler et al. (2005) and Koch et al. (2008a) (*black shaded* histogram) with those of our inner and outer halo samples (*gray solid* and *gray shaded* histogram, respectively) in the MW halo. The metallicity range is restricted to  $-2 < [\text{Fe}/\text{H}] < -1$ , where the observed discrepancy in  $[\alpha/\text{Fe}]$  ratios between the dSphs and the MW halo stars is largest. For some elements, similar peaks of the distributions are evident for the dSphs and the outer halo sample, that are distinct from the inner halo sample. In particular, the  $[\text{Mg}/\text{Fe}]$  ratio, which is shown in the middle panel of the top row, is peaked at  $\sim 0.3$  for the dSphs and the outer halo sample, while that of the inner halo sample is peaked at  $\sim 0.4-0.5$ . According to chemical evolution models for dSphs, the lower  $[\text{Mg}/\text{Fe}]$  ratio is partly interpreted by a lower star formation rate in dSphs which leads to a significant contribution of Fe to the system from delayed enrichment of Type Ia SNe (e.g., Lanfranchi & Matteucci 2003). Therefore, if the initial mass function (IMF) is the same for any systems and time-independent, contributions of Fe from SN Ia are needed to reproduce the  $[\text{Mg}/\text{Fe}]$  ratios observed in dSphs and the outer halo sample. Although the crude assumptions about the universality of the IMF should be ultimately examined, it can be inferred that possible progenitor systems for the outer halo are similar to the dSphs in terms of its lower star formation rate. Another remarkable feature in a comparison of the  $[\text{Mg}/\text{Fe}]$  distributions is that the  $[\text{Mg}/\text{Fe}]$  ratios of  $< -0.1$  observed in the dSphs are not observed for both of the inner and outer halo samples. The extremely low values of the  $[\text{Mg}/\text{Fe}]$  ratios are observed in Draco, Sextans, Carina and Leo I (Shetrone et al. 2001; Shetrone et al. 2003). A few Galactic halo stars have also been reported to have  $[\text{Mg}/\text{Fe}] < -0.1$  (Ivans et al. 2003), similar to the values observed in the dSphs. Whether such low  $[\text{Mg}/\text{Fe}]$  ratios are extremely rare within the MW halo or not cannot be concluded in

the present analysis because of the limitation of the number of sample ( $\sim 60$  for  $Z_{\max} > 5$  kpc) and the spatial extent (within  $\sim 2$  kpc from the Sun).

The [Na/Fe] and [Zn/Fe] ratios distributions are peaked at slightly lower value for the outer halo sample than the inner halo sample. For the [Na/Fe] ratios, the distribution for the outer halo and the dSphs have similar peaks at  $\sim -0.3$  dex. For the [Zn/Fe] ratios, although the distribution for the outer halo partly overlap with that for dSphs, these distribution is significantly different in that the distribution for dSphs is more broad ranging from  $\sim -0.6$  to 0.5 while that for the outer halo spans relatively narrow range. Models of nucleosynthesis products in the Type II SNe suggest that yields of Zn are determined by various factors such as an explosion energy, a progenitor mass, a mass cut or a geometry of the explosion (Umeda & Nomoto 2002). Which factor is mostly responsible for the [Zn/Fe] of the stars with  $-2 < [\text{Fe}/\text{H}] < -1$ , producing global abundance difference within the outer halo progenitors, remains unclear. We note that the measurement quality of dSph stars is not as good as that of halo stars, and that might be one of the reasons for the large scatter. Also, as noted in Section 3.6, the [Na/Fe] and the [Zn/Fe] ratios are systematically offset by  $\sim 0.1 - 0.2$  dex in our outer halo sample, which implies that an actual difference between the inner and the outer halo is much smaller than that can be seen in Figure 23 or in Table 11, if any.

For the neutron capture elements, Y and Ba, the distributions for both of the outer and the inner halo samples are significantly different from that for the dSphs. Specifically, for the field halo sample, the distributions of [Y/Fe] are peaked at higher values while those of [Ba/Fe] are peaked at lower values than for the dSphs. As a result, a significant discrepancy in distributions of [Ba/Y] ratio between the field halo samples and the dSphs is evident as shown in the lower right panel of Figure 23.

For lower metallicity ranges, Aoki et al. (2009a) analyzed chemical abundances of extremely metal-poor ( $[\text{Fe}/\text{H}] < -2.5$ ) stars in the Sextans dSphs. They showed that five in six sample stars show Mg/Fe comparable to the solar value, which is significantly lower than the typical Mg/Fe for the Galactic halo stars with similar metallicity. As shown in Figure 12, none of such low Mg/Fe stars are found among the outer halo sample with  $[\text{Fe}/\text{H}] < -2.5$ , such that  $[\text{Mg}/\text{Fe}] \sim 0.4-0.5$  on average. This comparison for Sextans dSphs and the MW outer halo imply that both systems had experienced distinct chemical enrichment history even at earlier epoch when extremely metal-poor stars were formed. Further abundance information for many stars belonging to other dSphs as well as the MW halo stars with various kinematics are necessary to conclude on a systematic abundance similarity/difference between these systems.

### 5.3.2. Comparison with ultra-faint dSphs

Ultra-faint dSphs recently discovered in SDSS data are a few orders of magnitudes fainter than ‘‘Classical’’ dSphs (e.g., Belokurov et al. 2007). Metallicities of these objects were measured to be  $[\text{Fe}/\text{H}] \sim -3$ , which is comparable to a low metallicity tail of the MW halo metallicity distribution (Kirby et al. 2008). Detailed chemical abundances have been measured

for several stars belonging to these objects (Koch et al. 2008b; Frebel et al. 2009).

Koch et al. (2008b) reported the chemical abundance of two red giants in the recently discovered ultra-faint dSph, Hercules, which are highly unusual in the following points; 1) these stars are strongly deficient in Ba ( $[\text{Ba}/\text{Fe}] < -2$ ) and 2) Mg is highly enhanced compared to Ca. The derived abundances are consistent with the ejecta of massive  $\sim 30 M_{\odot}$  Type II SNe. From these results, it is suggested that these stars were formed with ejecta of a few massive stars as a result of an incomplete mixing of elements within the star forming clouds. Some of the outer halo stars with comparable metallicity ( $-3 < [\text{Fe}/\text{H}] < -2$ ) show similar enhancement in Mg relative to Ca. On the other hand, no stars are found to be in this level of depression in Ba. If a mixing of nucleosynthesis products contained in individual SNe ejecta is inefficient in ultra-faint dSphs, a large scatter in abundances of heavy elements is expected. It remains unclear whether the system like ultra-faint dSphs contributed to the stellar halo until the expected scatters in the abundances are constrained using a larger number of abundance data for stars belonging to such faint stellar systems.

#### 5.4. Implications for the halo formation

In the previous sections, we have shown our main result that the inner and the outer halo samples display different trend in the  $[\text{Mg}/\text{Fe}]$ - $[\text{Fe}/\text{H}]$  relation in the metallicity range of  $-2 < [\text{Fe}/\text{H}] < -1$ , as found by significantly increasing the number of the sample stars with  $Z_{\text{max}} > 5$  kpc. Additionally, in this metallicity range, the outer halo sample displays the overlapping  $[\text{Mg}/\text{Fe}]$  distribution with the MW dwarf satellites. These results suggest that the MW halo is not homogeneously enriched with Mg-rich ejecta of massive Type II SNe, associated with rapid formation of the entire stellar halo which is expected to yield high  $[\text{Mg}/\text{Fe}]$  ratios (e.g., Woosley & Weaver 1995). Instead, the results support the suggestion that the inner and the outer halos may have formed with different mechanisms as examined by kinematics and metallicity of the halo stars (e.g., Carollo et al. 2007). Comparisons with the chemical evolution models specifically suggest that dominant progenitors, either *in situ* or accreted systems, of the inner and the outer halos experienced different chemical enrichment history.

Possible progenitors of the low- $[\text{Mg}/\text{Fe}]$  outer halo stars are systems in which star formation had proceeded at a slow rate and/or accreted relatively recent time. The recent accretion allows the progenitor system to dominate with iron-rich materials due to delayed enrichment with Type Ia SNe (e.g., Matteucci & Greggio 1986). This scenario requires a longer timescale for the outer halo formation which is consistent with the possible age spreads for the outer halo globular clusters in the MW using metallicities and horizontal-branch morphologies as a tracer (Searle & Zinn 1978; Geisler et al. 2007). Indeed, likely remnants of the later accretions were identified as spatially coherent substructures in the MW stellar halo (e.g., Juric et al. 2008). Nevertheless, Figure 23 also shows that the  $[\text{Mg}/\text{Fe}]$  distributions for neither of the inner nor the outer halo can reproduce the lowest  $[\text{Mg}/\text{Fe}]$  tail ( $[\text{Mg}/\text{Fe}] < 0$ ) of the satellites. This result



suggests that the progenitor system would not completely resemble with the presently surviving MW satellites in terms of chemical abundances, thereby star-formation history. As suggested in the cosmological simulation of Kazantzidis et al. (2009), the outer halo progenitors could have been disrupted through tidal interactions with the MW halo, even though they may have accreted relatively recent time.

In contrast to the outer halo, the enhanced [Mg/Fe] ratios ( $\sim 0.4-0.5$ ) frequently observed among the inner halo stars are compatible that the dominant fraction of the *inner* halo formed with an early accretion of a few massive progenitors (Font et al. 2006a). Alternatively, recent simulation results suggest that a sizable fraction of the inner halo may have formed in-situ (Zolotov et al. 2009).

Further numerical simulations which investigate different formation mechanisms for the inner and the outer halo components taking into account evolution of both kinematics and chemical abundances will be useful to understand observational data as presented in this work.

In the present study, quantitative estimation of the properties of the merging history such as a typical progenitor mass, epoch of the dominant accretion events or star formation history within the progenitor system remains unresolved. The major issue that hampers the interpretation of the present data is the bias against stars with  $Z_{\max} \leq 5$  kpc introduced in the sample selection. In order to supplement the lower  $Z_{\max}$  objects, we have used abundances published in the literature, for which systematic differences caused by using the different analysis methods is present for some elements. The incompleteness of the low  $Z_{\max}$  populations not only obscures the true nature of the inner halo population but may also produce an artificial trend in the abundance ratios as a function of kinematics. Therefore, systematic spectroscopic surveys that are unbiased to particular kinematics are required for a more quantitative examination of the merging history of the MW. This should be addressed with advanced instruments that are capable of a multi-object spectroscopy down to fainter magnitudes. Another important task for the reconstruction of the MW formation is the detailed theoretical understanding of chemical enrichment history within the progenitor systems and their assembly process to form a large galaxy (e.g., Johnston et al. 2008). Our crude underlying assumption in the previous discussions is that the abundance ratios are related to the global properties of the progenitor systems such as mass, luminosity or average metallicity. These assumptions should be tested with theoretical modeling of these systems taking into account the physics of star formation, nucleosynthesis products of various SNe, mixing of the enriched gas or mass loss from evolved stars. In addition, observational estimates of abundance patterns for individual stars in the dwarf satellites should be further obtained to assess the theoretical modelings.

## 6. Conclusion

We present the detailed chemical abundances of 57 metal-poor ( $[\text{Fe}/\text{H}] < -1$ ) halo stars with  $Z_{\max} > 5$  kpc that are candidates of the outer halo population derived from homogeneous

analysis of spectra obtained with Subaru/HDS. This data set is combined with the data presented in the literature in which both high-resolution abundance estimates and kinematic data are available. The resulting sample of  $>200$  stars with  $[\text{Fe}/\text{H}] < 0$  are used to investigate systematic differences in an elemental abundance pattern between the presumed inner and the outer halo populations.

It is shown that the outer halo sample, conventionally defined as stars with  $Z_{\text{max}} > 5$  kpc, shows lower  $[\text{Mg}/\text{Fe}]$  on average by  $\sim 0.1$  dex than those of the inner halo sample in the metallicity range of  $-2 < [\text{Fe}/\text{H}] < -1$ . Modestly lower  $[\text{Na}/\text{Fe}]$ ,  $[\text{Ca}/\text{Fe}]$ ,  $[\text{Mn}/\text{Fe}]$ ,  $[\text{Zn}/\text{Fe}]$  and  $[\text{Y}/\text{Fe}]$  are also observed for the outer halo sample. Since the criterion of  $Z_{\text{max}} > 5$  kpc preferentially selects the stars with a large  $R_{\text{apo}}$  or a large  $V_{\text{RF}}$ , the results are consistent with the earlier suggestions for a decrease in  $[\alpha/\text{Fe}]$  ratios with increasing  $R_{\text{apo}}$  or  $V_{\text{RF}}$  in SB02 and Fulbright (2002). The systematic difference in abundance ratios found for these elements implies that formation mechanisms and/or dominant building blocks between the inner and the outer halo are different as suggested from studies of kinematics and metallicity for the halo stars. A larger number of sample for which both high-resolution abundances and accurate kinematics are available will be required in order to perform an analysis of chemical abundance ratios for each bin of  $[\text{Fe}/\text{H}]$  and kinematic parameters that can be compared to the predictions of the standard theory for galaxy formation.

The  $[\text{Na}/\text{Fe}]$ ,  $[\text{Mg}/\text{Fe}]$  and  $[\text{Zn}/\text{Fe}]$  ratios for the outer halo population partly overlap with those measured for bright giant stars in the MW satellites. On the other hand, for Ti and Y, neither of the inner nor outer halo populations overlap with the MW satellites. Whether the currently observed MW satellites could have contributed to the current stellar halo remains unclear. Elaborated modeling of the star formation history of chemical evolution within the dwarf satellites including the extent of mixing of SNe ejecta as well as dynamical evolution of the satellites will be needed to constrain the detailed properties of possible building blocks of the MW outer halo.

We would like to thank the staff and crew at the Subaru observatory for their exceptional assistance on our observation. We are grateful to L. Zhang, G. Zhao, T. Tsujimoto, T. C. Beers for useful discussion and suggestions, which significantly improved this paper. We also thank the referee, P. Nissen., for valuable comments on an earlier draft. This work has been supported in part by a Grant-in-Aid for Scientific Research (20340039) of the Ministry of Education, Culture, Sports, Science and Technology in Japan.

## References

- Alonso, A., Arribas, S., & Martinez-Roger, C. 1996, *A&A*, 313, 873  
 Alonso, A., Arribas, S., & Martinez-Roger, C. 1999, *A&AS*, 140, 261  
 An, D. et al. 2009, arXiv:0907.1082

- Andrievsky, S. M., Spite, M., Korotin, S. A., Spite, F., Bonifacio, P., Cayrel, R., Hill, V., & Francois, P. 2007, *A&A*, 464, 1081
- Aoki, W. et al. 2005, *ApJ*, 632, 611
- Aoki, W. et al. 2009a, *A&A*, 502, 569
- Aoki, W., Barklem, P. S., Beers, T. C., Christlieb, N., Inoue, S., García Pérez, A. E., Norris, J. E., Carollo, D. 2009b, *ApJ*, 698, 1803
- Baba, H., et al. 2002, in *Astronomical Data Analysis Software and Systems XI*, APS Conference Proceedings Vol. 281, ed. D. A. Bohlender, D. Durand, & T. H. Handley (San Francisco: Astronomical Society of the Pacific), 298
- Barklem, P. S., et al. 2005, *A&A*, 439, 129
- Baumuller, D., Butler, K., & Gehren, T. 1998, *A&A*, 338, 637
- Beers, T. C., Chiba, M., Yoshii, Y., Platais, I., Hanson, R. B., Fuchs, B., & Rossi, S. 2000, *AJ*, 119, 2866
- Bell, E. F. et al. 2008, *ApJ*, 680, 295
- Belokurov, V. et al. 2006, *ApJ*, 642, L137
- Belokurov, V. et al. 2007, *ApJ*, 654, 897
- Brown, T. M. et al. 2008, *ApJ*, 685, L121
- Bullock, J. S. & Johnston, K. V. 2005, *ApJ*, 635, 931
- Carney, B. W., Latham, D. W., Laird, J. B. & Aguilar, L. A. 1994, *AJ*, 107, 2240
- Carney, B. W., Latham, D. W., Stefanik, R. P., Laird, J. B. & Morse, J. A. 2003, *AJ*, 125, 293
- Carollo, D. et al. 2007, *Nature*, 450, 1020
- Carollo, D. et al. 2009, arXiv:0909.3019
- Castelli, F. & Kurucz, R. L. 2003, *IAUS*, 210P, A20
- Cayrel, R. 1988, in *The Impact of Very High S/N Spectroscopy on Stellar Physics*, ed. G. Cayrel de Strobel, & M. Spite (Dordrecht: Kluwer), 345
- Chiba, M. & Beers, T. C. 2000, *AJ*, 119, 2843
- De Lucia, G. & Helmi, A. 2008, *MNRAS*, 391, 14
- Dettbarn, C., Fuchs, B., Flynn, C., & Williams, M. *A&A*, 474, 857
- Diemand, J., Kuhlen, M. & Madau, P. 2007, *ApJ*, 667, 859
- Font, A. S., Johnston, K. V., Bullock, J. S., & Robertson, B. E. 2006a, *ApJ*, 638, 585
- Font, A. S., Johnston, K. V., Bullock, J. S., & Robertson, B. E. 2006b, *ApJ*, 646, 886
- Francois, P., Depagne, E. & Hill, V., et al. 2007, *A&A*, 476, 935
- Frebel, A., Simon, J. D., Geha, M. & Willman, B. 2009, arXiv:0902.2395
- Freeman, K. C. & Bland-Hawthorn, J. 2002, *ARA&A*, 40, 487
- Fulbright, J.P. 2002, *AJ*, 123, 404
- Geisler, D., Smith, V. V., Wallerstein, G., Gonzalez, G., & Charbonnel, C. 2005, *AJ*, 129, 1428
- Geisler, D., Wallerstein, G., Smith, V. V. & Casetti-Dinescu, D. I. 2007, *PASP*, 119, 939
- Gratton, R. G., Carretta, E., Claudi, R., Lucatello, S. & Barberi, M. 2003, *A&A*, 404, 187 (G03)
- Gratton, R. G., Carretta, E., Desidera, S., Lucatello, S., Mazzei, P. & Barbieri, M. 2003, *A&A*, 406, 131
- Grevesse, N., Noels, A. & Sauval, A. J. 1996, *ASPC*, 99, 117

Hanson, R. B., Sneden, C., Kraft, R. P. & Fulbright, J. 1998, *AJ*, 116, 1286  
Helmi, A. & White, S. D. M. 1999, *MNRAS*, 307, 495  
Helmi, A., White, S. D. M., de Zeeuw, T. & Zhao, H. 1999, *Nature*, 402, 53  
Ibata, R. A., Gilmore, G. & Irwin, M. J. 1994, *Nature*, 370, 194  
Ivans, I. I., Sneden, C., James, C. R., Preston, G. W., Fulbright, J. P., Hoflich, P. A., Carney, B. W. & Wheeler, J. G. 2003, *ApJ*, 592, 906  
Ivezic, Z. et al. 2008, *ApJ*, 684, 287  
Johnston, K. V., Bullock, J. S., Sharma, S., Font, A., Robertson, B. E. & Leitner, S. N. 2008, *ApJ*, 689, 936  
Jorissen, A., Začs, L., Ubry, S., Lindgren, H. and Musaev, F. A. 2005, *A&A*, 441, 1135  
Juric, M. et al. 2008, *ApJ*, 673, 864  
Kazantzidis, S., Zentner, A. R., Kravtsov, A. V., Bullock, J. S. & Debattista, V. P. 2009, *ApJ*, 700, 1896  
Kepley, A. A. et al. 2007, *AJ*, 134, 1579  
Kirby, E. N., Simon, J. D., Geha, M., Guhathakurta, P. and Frebel, A. 2008, *ApJ*, 685, L43  
Klement, R. et al. 2009, *ApJ*, 698, 865  
Koch, A., Grebel, E. K., Gilmore, G. F., Wyse, R. F. G., Kleyna, J. T., Harbeck, D. R., Wilkinson, M. I. & Evans, N. W. 2008a, *AJ*, 135, 1580  
Koch, A., McWilliam, A., Grebel, E. K., Zucker, D. B. & Belokurov, V. 2008b, *ApJ*, 688, L13  
Kupka, F. G., Ryabchikova, T. A., Piskunov, N. E., Stempels, H. C. & Weiss, W. W. 2000, *Baltic Astronomy*, 9, 590  
Kurucz, R. L., & Bell, B. 1995, *Kurucz CD-ROM 23, Atomic Line Data* (Cambridge: SAO)  
Lai, D. K., Bolte, M., Johnson, J. A., Lucatello, S., Heger, A. & Woosley, S. E. 2008, *ApJ*, 681, 1524  
Lanfranchi, G. A. & Matteucci, F. 2003, *MNRAS*, 345, 71  
Latham, D. W., Stefanik, R. P., Torres, G., Davis, R. J., Mazeh, T., Carney, B. W., Laird, J. B. & Morse, J. A. 2002, *AJ*, 124, 1144  
Majewski, S. R., Skrutskie, M. F., Weinberg, M. D. & Ostheimer, J. C. 2003, *ApJ*, 599, 1082  
Martinez-Delgado, D., Penarrubia, J., Gabany, R. J., Trujillo, I., Majewski, S. R. & Pohlen, M. 2008, *ApJ*, 689, 184  
Matteucci, F., & Greggio, L. 1986, *A&A*, 154, 279  
McWilliam, A. 1998, *AJ*, 1998, 115, 1640  
Morrison, H. L. et al. 2009, *ApJ*, 694, 130  
Nissen, P. E., & Schuster, W. J. 1997, *A&A*, 326, 751  
Noguchi, K. et al. 2002, *PASJ*, 54, 855  
Norris, J. E. 1994, *ApJ*, 431, 645  
Richardson, J. C. et al. 2009, *MNRAS*, 396, 1842  
Robertson, B., Bullock, J. S., Font, A. S., Johnston, V. & Hernquist, L. 2005, *ApJ*, 632, 872  
Roederer, I. U. 2008, *AJ*, 137, 272  
Ryan, S. G. & Norris, J. E. 1991, *AJ*, 101, 1835  
Ryan, S. G., Norris, J. E. & Beers, T. C. 1996, *ApJ*, 471, 254  
Schlaufman, K. C. et al. 2009, *ApJ*, 703, 2177

- Searle, L. & Zinn, R. 1978, ApJ, 225, 357
- Shetrone, M. D., Cote, P. & Sargent, W. L. W. 2001, ApJ, 548, 529
- Shetrone, M. D., Venn, K. A., Tolstoy, E., Primas, F., Hill, V. & Kaufer, A. 2003, ApJ, 125, 684
- Skrutskie, M. F. et al. 2006, AJ, 131, 1163
- Sobeck, J. S., Lawler, J. E. & Sneden, C. 2007, ApJ, 667, 1267
- Sommer-Larsen, J. & Zhen, C., 1990, MNRAS, 242, 10
- Starkenburger, E. et al. 2009, ApJ, 698, 567
- Stephens, A. 1999, AJ, 117, 1771
- Stephens, A. & Boesgaard, A. M. 2002, AJ, 123, 1647 (SB02)
- Takeda, Y., Zhao, G., Takada-Hidai, M., Chen, Y.-Q., Saito, Y., & Zhang, H.-W. 2003, Chin. J. Astron. Astrophys., 3, 316
- Tolstoy, E., Venn, K. A., Shetrone, M., Hill, V., Kaufer, A., & Szeifert, T. 2003, AJ, 125, 707
- Umeda, H. & Nomoto, K. 2002, ApJ, 565, 385
- Unsöld, A. 1955, Physik der Sternatmosphären, MIT besonderer Berücksichtigung der Sonne (Berlin, Springer), 2. Aufl.
- Venn, K. A., Irwin, M., Shetrone, M. D., Tout, C. A., Hill, V. & Tolstoy, E. 2004, AJ, 128, 1177
- Willman, B. et al. 2005, AJ, 129, 2692
- Woolley, W. E., & Weaver, T. A. 1995, ApJS, 101, 181
- Zhang, L., Ishigaki, M., Aoki, W., Zhao, G. & Chiba, M. 2009, ApJ, 706, 1095
- Zolotov, A., Willman, B., Brooks, A. M., Governato, F., Brook, C. B., Hogg, D. W., Quinn, T. & Stinson, G. 2009, ApJ, 702, 1058

**Table 1.** Observational data

Star name	RA (J2000)	DEC (J2000)	V (mag)	[Fe/H]* (dex)	Exp.time (s)	S/N <sup>†</sup>	V <sub>rad</sub> <sup>‡</sup> (km s <sup>-1</sup> )
BD+04° 2621	12 28 44.65	+04 01 27.0	9.92	-2.41	2700	312	-41.2 ± 0.2
BD+13° 2995	15 44 14.74	+12 56 49.7	11.90	-1.43	3600	168	45.5 ± 0.3
BD-03° 5215	21 28 01.31	-03 07 40.7	10.17	-1.57	3600	369	-292.8 ± 0.2
BD-10° 548	02 46 55.72	-10 07 35.0	10.41	-1.07	1200	281	238.4 ± 0.3
BD-14° 5890	20 56 09.15	-13 31 16.9	10.21	-2.07	1200	359	119.9 ± 0.3
BD-17° 484	02 31 25.76	-16 59 05.1	10.44	-1.74	1800	303	236.2 ± 0.2
BD-18° 271	01 37 18.88	-17 29 03.7	9.81	-2.17	1800	423	-208.5 ± 0.2
CD-24° 17504	23 07 20.12	-23 52 34.3	12.12	-3.70	3600	249	45.4 ± 0.3
G 125-13	19 31 09.23	+36 09 10.1	10.24	-1.39	1200	351	219.7 ± 0.2
G 14-39	13 14 26.93	-04 05 43.5	12.85	-2.13	3600	105	197.9 ± 0.3
G 154-34	17 55 58.45	-16 24 32.8	11.29	-2.15	2400	297	-205.2 ± 0.2
G 165-39	13 59 09.48	+33 51 39.4	10.06	-2.23	1200	375	-170.3 ± 0.3
G 17-25	16 34 42.35	-04 13 44.3	9.63	-1.54	1800	304	-176.2 ± 0.4
G 18-24	22 05 01.41	+08 38 18.4	12.03	-1.43	3600	186	-121.1 ± 0.4
G 188-30	21 55 16.15	+32 38 41.1	11.03	-1.86	2400	337	229.7 ± 0.3
G 20-15	17 47 27.97	-08 46 47.7	10.59	-1.99	1200	167	85.1 ± 0.2
G 206-23	18 21 35.81	+34 49 01.8	12.09	-1.96	3600	159	-0.5 ± 0.4
G 25-24	21 16 41.64	-01 18 08.8	11.63	-1.94	3000	312	45.4 ± 0.3
G 275-11	23 09 58.45	-20 57 23.1	12.29	-1.54	3600	210	13.3 ± 0.2
G 59-27	12 36 39.45	+27 28 28.2	10.90	-2.20	2700	155	-120.2 ± 0.4
HD 111721	12 51 25.36	-13 29 25.4	7.97	-1.26	600	584	21.6 ± 0.2
HD 111980	12 53 15.05	-18 31 20.0	8.37	-0.95	600	507	167.7 ± 0.2
HD 214161	22 37 08.04	-40 30 38.4	9.10	-2.16	600	388	-368.6 ± 0.2
HD 214362	22 37 58.56	-22 38 39.7	9.10	-1.77	600	420	-90.9 ± 0.2
HD 218857	23 11 24.63	-16 15 03.2	8.94	-1.94	600	443	-169.4 ± 0.2
LP 443-65	15 49 22.83	+14 38 28.0	12.31	-1.45	3600	218	-186.2 ± 0.3
LP 763-87	23 37 28.51	-13 47 38.7	11.99	-2.51	3600	166	87.9 ± 0.7
LP 859-35	15 19 35.66	-24 31 04.1	11.66	-1.38	3600	123	168.3 ± 0.3
LP 877-23	22 52 41.03	-20 35 32.9	12.06	-1.74	3600	258	-221.4 ± 0.2

\*The [Fe/H] values taken from the original catalogs (Beers et al. (2000), Carney et al. (1994) or Ryan & Norris (1991))

<sup>†</sup>Signal-to-noise ratio measured as a photon count per dispersion element around ~5800 Å

<sup>‡</sup> Heliocentric radial velocities measured from the spectra obtained in this work.



**Table 2.** Kinematics of the sample stars

Star name	$U$ (km s <sup>-1</sup> )	$V$ (km s <sup>-1</sup> )	$W$ (km s <sup>-1</sup> )	$V_\phi$ (km s <sup>-1</sup> )	$R_{\text{apo}}$ (kpc)	$R_{\text{peri}}$ (kpc)	$Z_{\text{max}}$ (kpc)	$e$
BD+01° 3070	351	56	-105	275	67.32	4.65	17.19	0.87
BD+04° 2466	-107	-538	-259	-329	54.26	8.47	31.20	0.73
BD+04° 2621	2	-268	-154	-48	8.47	2.80	7.56	0.53
BD+09° 2870	377	-273	55	-49	36.62	0.76	6.48	0.96
BD+10° 2495	73	-47	275	174	21.49	7.81	17.30	0.47
BD+12° 2547	-299	-350	-119	-144	28.79	2.80	8.09	0.82
BD+13° 2995	55	-43	140	176	10.03	6.80	4.50	0.20
BD+29° 2356	-24	-71	-190	149	10.06	7.81	7.19	0.14
BD+30° 2611	-10	-59	-284	161	19.98	8.04	16.98	0.43
BD-03° 5215	149	-200	142	16	11.30	0.55	7.62	0.91
BD-10° 548	192	-111	-141	109	15.68	3.15	7.64	0.67
BD-14° 5890	-345	-430	-163	-178	51.85	3.42	28.20	0.88
BD-17° 484	267	-266	-81	-45	18.79	0.93	3.61	0.91
BD-18° 271	-170	-269	173	-47	16.73	1.77	12.24	0.81
CD-24° 17504	77	-276	-244	-57	12.01	6.35	12.02	0.33
G 112-43	-123	-60	-202	159	15.67	6.36	10.74	0.43
G 115-58	185	-274	167	-55	14.91	2.07	11.00	0.76
G 125-13	-190	-219	-140	4	13.59	0.11	8.11	0.98
G 14-39	198	-163	250	58	21.51	4.37	20.60	0.67
G 15-13	-217	-423	166	-203	24.59	5.28	11.76	0.65
G 154-34	141	-234	-129	-14	10.92	0.44	5.95	0.92
G 165-39	-239	-215	-145	6	17.56	0.15	10.04	0.98
G 166-37	-297	-128	339	94	70.11	5.30	66.39	0.86
G 17-25	79	-160	-128	60	9.27	2.05	5.01	0.65
G 18-24	220	-173	-135	43	15.78	1.15	7.97	0.86
G 188-30	278	-190	-93	27	19.86	0.57	5.08	0.94
G 20-15	-134	-24	-122	196	14.08	5.79	4.73	0.42
G 206-23	-213	-151	133	76	15.26	2.04	7.54	0.77
G 238-30	230	-286	405	-71	78.38	6.65	76.89	0.84
G 25-24	31	-146	-305	73	17.45	8.23	17.19	0.37
G 275-11	140	-245	-135	-26	11.10	0.82	6.36	0.86
G 41-41	-150	-399	200	-182	18.75	6.45	11.97	0.49
G 48-29	-363	-298	-148	-83	42.30	1.70	19.53	0.92
G 53-41	30	-316	-162	-95	8.76	4.65	6.38	0.33

Table 2. (Continued.)

Star name	$U$ (km s <sup>-1</sup> )	$V$ (km s <sup>-1</sup> )	$W$ (km s <sup>-1</sup> )	$V_\phi$ (km s <sup>-1</sup> )	$R_{\text{apo}}$ (kpc)	$R_{\text{peri}}$ (kpc)	$Z_{\text{max}}$ (kpc)	$e$
G 59-27	66	-237	-135	-17	9.02	0.66	6.05	0.87
G 64-12	-50	-317	397	-97	42.70	8.33	41.40	0.68
G 64-37	-207	-390	-161	-171	20.06	4.63	9.66	0.63
HD 107752	134	-398	120	-171	14.29	4.89	5.11	0.49
HD 108577	137	-205	-161	18	11.15	1.25	10.67	0.81
HD 111721	56	-274	-133	-54	8.84	1.98	5.34	0.64
HD 111980	-280	-195	-102	23	20.24	0.49	6.00	0.95
HD 119516	130	-60	-254	160	20.86	7.09	16.78	0.50
HD 124358	33	-439	293	-218	27.77	7.76	21.12	0.56
HD 128279	-8	-62	-234	158	13.04	8.37	10.24	0.23
HD 134439	-312	-499	-61	-279	50.08	5.04	5.01	0.82
HD 175305	62	-68	-285	151	20.56	8.16	17.67	0.44
HD 214161	290	-90	262	131	44.26	4.69	37.32	0.81
HD 214362	331	-236	-134	-22	29.65	0.43	11.48	0.97
HD 218857	-92	-141	161	80	10.06	3.36	7.13	0.51
HD 237846	-202	-137	-185	92	20.24	3.51	14.49	0.71
HD 33771	-66	-221	227	-5	10.97	5.68	11.67	0.35
HD 85773	13	-213	-130	9	8.97	0.41	6.59	0.92
LP 443-65	383	-219	169	-5	47.69	0.10	25.41	1.00
LP 763-87	92	-257	-239	-38	12.29	5.66	12.57	0.39
LP 859-35	-188	-231	-144	-12	13.43	0.38	8.21	0.95
LP 877-23	33	-278	140	-58	8.58	2.33	5.65	0.59
LP 894-3	214	-130	-218	94	21.37	4.02	17.71	0.69

**Table 3.** Measured equivalent widths\*

Z Elem. I/II <sup>†</sup>	$\lambda^{\ddagger}$ (Å)	$\log(gf)^{\S}$	Exp. <sup>  </sup> (eV)	EW <sup>#</sup> (BD+01 3070) (mÅ)	EW(BD+04 2466) (mÅ)	EW(BD+04 2621) (mÅ)	...	Ref.**
11 Na I	5682.650	-0.820	2.10	10.3	4.8	-9.9	...	
11 Na I	5688.219	-0.370	2.10	17.6	-9.9	4.6	...	
11 Na I	6154.227	-1.660	2.10	-9.9	-9.9	-9.9	...	
⋮						⋮		

\*This table is fully available in an electronic form.

<sup>†</sup>Atomic number (Z), a name of the element and a state of inization (I/II).

<sup>‡</sup>Wavelength of a line center in units of Å.

<sup>§</sup> $\log(gf)$  values.

<sup>||</sup>Excitation potential in units of electron volts.

<sup>#</sup>Measured equivalent widths in units of mÅ. The value of -9.9 means that the line is undetectable or not adequately measured.

\*\*Reference of the atomic data.

**Table 4.** Stellar atmospheric parameters

Star name	$T_{\text{eff}}$ (K)	$\log g$	[Fe/H] (dex)	$\xi$ (km s <sup>-1</sup> )	$E(B - V)^*$ (mag)	$(V - K)_0^\dagger$ (mag)	$T_{\text{eff}}(\text{color})$ (K)
BD+01° 3070	5077±35	3.01	-1.63	1.04	0.06	1.83	5308
BD+04° 2466	5065±93	1.82	-2.10	1.82	0.04	1.87	5265
BD+04° 2621	4453±18	0.90	-2.68	1.92	0.02	2.31	4760
BD+09° 2870	4285±18	0.29	-2.70	1.92	0.03	2.44	4620
BD+10° 2495	4819±47	1.92	-2.17	1.70	0.02	2.09	5003
BD+12° 2547	4494±27	1.29	-2.10	1.76	0.03	2.38	4673
BD+13° 2995	5650±54	4.90	-1.07	0.05	0.03	1.61	5561
BD+29° 2356	4884±22	2.49	-1.44	1.56	0.01	2.42	4637
BD+30° 2611	4367±75	1.17	-1.32	1.84	0.02	2.97	4214
BD-03° 5215	5380±100	2.05	-1.60	2.14	0.04	1.68	5512
BD-10° 548	4855±90	2.15	-1.72	1.40	0.02	2.10	4985
BD-14° 5890	4630±29	1.47	-2.42	1.73	0.04	2.15	4938
BD-17° 484	6078±56	3.85	-1.65	1.16	0.02	1.26	6172
BD-18° 271	4080±39	0.01	-2.66	2.30	0.02	2.96	-
CD-24° 17504	5821±125	3.50	-3.66	1.22	0.02	1.31	-
G 112-43	5909±52	3.59	-1.51	1.43	0.01	1.35	6001
G 115-58	6131±70	3.87	-1.46	1.44	0.01	1.27	6141
G 125-13	5688±82	4.02	-1.69	1.12	0.01	1.37	5969
G 14-39	4945±82	5.00	-1.88	0.04	0.02	2.38	4596
G 15-13	5225±78	5.00	-1.48	0.05	0.02	1.99	5056
G 154-34	4975±41	4.28	-2.77	0.15	0.04	1.70	5463
G 165-39	6162±68	3.62	-2.16	1.57	0.01	1.22	6271
G 166-37	5355±90	4.95	-1.29	0.05	0.02	1.82	5267
G 17-25	5515±69	5.00	-0.91	0.05	0.03	2.02	5033
G 18-24	5447±98	4.18	-1.62	0.31	0.05	1.40	5915
G 188-30	5326±39	5.00	-1.62	0.05	0.02	1.87	5204
G 20-15	5850±89	4.00	-1.75	1.16	0.09	1.54	5689
G 206-23	5795±97	3.64	-2.18	1.20	0.03	1.28	6149
G 238-30	5299±82	3.39	-3.72	1.19	0.02	1.76	-
G 25-24	5594±76	4.07	-2.02	1.02	0.03	-	-
G 275-11	5817±46	3.78	-1.54	1.06	9.99	-	-
G 41-41	6076±22	3.28	-2.98	1.49	0.03	1.14	6490
G 48-29	6118±37	3.46	-3.03	1.73	0.06	1.05	-
G 53-41	5737±68	4.12	-1.44	1.10	0.04	1.37	5959

Table 4. (Continued.)

Star name	$T_{\text{eff}}$ (K)	$\log g$	[Fe/H] (dex)	$\xi$ (km s <sup>-1</sup> )	$E(B - V)^*$ (mag)	$(V - K)_0^\dagger$ (mag)	$T_{\text{eff}}(\text{color})$ (K)
G 59-27	5829±108	3.20	-2.42	1.66	0.02	1.24	6246
G 64-12	6070±70	3.58	-3.52	1.46	0.02	1.22	-
G 64-37	6105±48	3.65	-3.36	1.49	0.02	1.16	6501
HD 107752	4401±26	0.54	-3.10	1.90	0.03	2.26	-
HD 108577	4840±43	0.96	-2.37	1.87	0.03	2.01	5100
HD 111721	4932±31	2.65	-1.34	1.17	0.03	2.09	4991
HD 111980	5641±101	3.75	-1.25	1.14	0.01	1.56	5649
HD 119516	5438±75	1.76	-2.08	2.28	0.03	1.59	5662
HD 124358	4647±38	1.26	-1.78	1.84	0.06	2.31	4749
HD 128279	5003±35	2.49	-2.44	1.42	0.04	1.83	5337
HD 134439	5230±68	5.00	-1.21	0.07	0.01	-	-
HD 175305	4940±59	2.48	-1.45	1.28	0.03	2.03	5062
HD 214161	4624±40	1.37	-2.23	1.70	0.02	2.18	4891
HD 214362	5636±38	1.60	-2.05	2.46	0.03	1.47	5853
HD 218857	4892±40	2.22	-2.12	1.56	0.03	1.97	5142
HD 237846	4621±39	1.04	-3.18	1.74	0.01	2.08	-
HD 33771	4555±37	1.27	-2.23	1.86	0.03	2.34	4722
HD 85773	4146±16	0.01	-2.58	2.05	0.05	2.76	4362
LP 443-65	6035±84	3.90	-1.74	1.34	0.04	1.18	6322
LP 763-87	5979±80	3.69	-2.68	1.47	0.03	1.16	6417
LP 859-35	5292±68	3.75	-1.78	0.46	0.06	1.58	5632
LP 877-23	5197±53	4.37	-1.78	0.06	0.02	1.66	5506
LP 894-3	5758±90	3.85	-1.67	1.12	0.01	1.50	5748

\*Reddenings.

† Extinction corrected  $V - K$  color. The  $K$ -band magnitudes are taken from the 2MASS catalogue (Skrutskie et al. 2006).

**Table 5.** Comparison of atmospheric parameters derived in this work and those derived in literature

Name	$T_{\text{eff}}$ (K)			$\log g$			[Fe/H] (dex)			$\xi$ (km s $^{-1}$ )		
	TW	SB02	$\Delta^*$	TW	SB02	$\Delta$	TW	SB02	$\Delta$	TW	SB02	$\Delta$
G 15-13	5225	5082	143	5.00	4.61	0.39	-1.50	-1.70	0.20	0.05	0.00	0.05
G 165-39	6162	6118	44	3.62	3.53	0.09	-2.20	-2.17	-0.03	1.57	1.45	0.12
G 166-37	5355	5350	5	4.95	4.71	0.24	-1.31	-1.39	0.08	0.05	0.00	0.05
G 188-30	5326	5141	185	5.00	4.44	0.56	-1.64	-1.89	0.25	0.05	0.31	-0.26
G 238-30	5299	5383	-84	3.39	3.43	-0.04	-3.77	-3.60	-0.17	1.19	1.19	0.00
G 25-24	5594	5733	-139	4.07	3.98	0.09	-2.06	-1.88	-0.18	1.02	1.21	-0.19
G 64-12	6070	6074	-4	3.58	3.72	-0.14	-3.56	-3.47	-0.09	1.46	1.19	0.27
G 64-37	6105	6122	-17	3.65	3.87	-0.22	-3.40	-3.32	-0.08	1.49	1.50	-0.01
$\Delta_{\text{ave}} (\sigma)^\dagger$	17 (108)			0.12 (0.26)			-0.00 (0.16)			0.00 (0.17)		
	TW	G03	$\Delta$	TW	G03	$\Delta$	TW	G03	$\Delta$	TW	G03	$\Delta$
G 17-25	5515	5080	435	5.00	4.51	0.49	-0.91	-1.34	0.43	0.05	0.00	0.05
HD 111980	5641	5745	-104	3.75	3.93	-0.18	-1.25	-1.19	-0.06	1.14	1.81	-0.67
HD 134439	5230	4996	234	5.00	4.65	0.35	-1.21	-1.33	0.12	0.07	0.01	0.06
G 43-3	6181	6290	-109	3.61	4.02	-0.41	-2.31	-2.18	-0.13	1.39	1.25	0.14
$\Delta_{\text{ave}} (\sigma)$	188 (272)			0.22 (0.35)			0.16 (0.25)			-0.19 (0.42)		
$\Delta_{\text{ave}} (\sigma)^\ddagger$	7 (197)			-0.08 (0.40)			-0.02 (0.13)			-0.16 (0.49)		

\*Difference in derived atmospheric parameters between this work (TW) and the literature (SB02 or G03).

†An average of the differences and a RMS scatter around the average.

‡Same as † but excluding G 17-25 (spectroscopic binary).



**Table 6.** Derived Na, Mg, Si, and Ca abundances

Star name	[Na I/H]	<i>N</i>	[Mg I/H]	<i>N</i>	[Si I/H]	<i>N</i>	[Si II/H]	<i>N</i>	[Ca I/H]	<i>N</i>
BD+01° 3070	$-1.88 \pm 0.09$	2	$-1.26 \pm 0.03$	3	$-1.38 \pm 0.09$	1	-	-	$-1.39 \pm 0.03$	13
BD+04° 2466	$-2.14 \pm 0.08$	1	$-1.66 \pm 0.08$	2	$-1.52 \pm 0.08$	1	-	-	$-1.63 \pm 0.04$	10
BD+04° 2621	$-2.89 \pm 0.06$	1	$-2.09 \pm 0.08$	4	-	-	-	-	$-2.29 \pm 0.02$	8
BD+09° 2870	$-2.76 \pm 0.08$	1	$-1.96 \pm 0.16$	5	-	-	-	-	$-2.28 \pm 0.03$	11
BD+10° 2495	$-2.33 \pm 0.08$	2	$-1.70 \pm 0.06$	4	$-1.82 \pm 0.07$	1	-	-	$-1.88 \pm 0.03$	14
BD+12° 2547	$-2.39 \pm 0.08$	2	$-1.61 \pm 0.08$	1	$-1.68 \pm 0.08$	1	-	-	$-1.80 \pm 0.03$	9
BD+13° 2995	$-1.21 \pm 0.06$	2	$-0.52 \pm 0.06$	2	-	-	-	-	$-0.87 \pm 0.03$	10
BD+29° 2356	$-1.70 \pm 0.06$	3	$-1.05 \pm 0.10$	1	$-1.16 \pm 0.10$	2	-	-	$-1.22 \pm 0.04$	9
BD+30° 2611	-	-	$-1.08 \pm 0.09$	1	$-1.19 \pm 0.09$	2	-	-	$-1.26 \pm 0.04$	5
BD−03° 5215	$-2.02 \pm 0.09$	1	$-1.27 \pm 0.08$	2	-	-	-	-	$-1.24 \pm 0.08$	2
BD−10° 548	$-1.98 \pm 0.10$	2	$-1.29 \pm 0.05$	3	$-1.38 \pm 0.02$	3	-	-	$-1.40 \pm 0.03$	9
BD−14° 5890	$-2.70 \pm 0.06$	2	$-1.82 \pm 0.08$	4	-	-	-	-	$-2.06 \pm 0.03$	8
BD−17° 484	$-2.04 \pm 0.07$	2	$-1.24 \pm 0.04$	5	-	-	-	-	$-1.28 \pm 0.03$	7
BD−18° 271	$-2.81 \pm 0.09$	2	$-1.79 \pm 0.07$	4	$-2.16 \pm 0.09$	1	-	-	$-2.34 \pm 0.03$	9
CD−24° 17504	-	-	$-2.96 \pm 0.05$	1	-	-	-	-	$-3.40 \pm 0.05$	2
G 112-43	$-1.60 \pm 0.08$	2	$-1.13 \pm 0.06$	4	$-1.19 \pm 0.08$	1	-	-	$-1.21 \pm 0.02$	15
G 115-58	-	-	$-1.27 \pm 0.04$	4	$-1.42 \pm 0.07$	1	-	-	$-1.27 \pm 0.03$	11
G 125-13	$-1.85 \pm 0.08$	2	$-1.30 \pm 0.03$	4	-	-	-	-	$-1.43 \pm 0.03$	9
G 14-39	$-1.91 \pm 0.04$	1	$-1.35 \pm 0.04$	1	-	-	-	-	$-1.43 \pm 0.04$	7
G 15-13	$-2.27 \pm 0.08$	1	$-1.17 \pm 0.08$	2	-	-	-	-	$-1.33 \pm 0.02$	10
G 154-34	-	-	$-2.25 \pm 0.03$	3	-	-	-	-	$-2.47 \pm 0.03$	10
G 165-39	$-2.41 \pm 0.06$	1	$-1.75 \pm 0.07$	5	-	-	-	-	$-1.74 \pm 0.02$	13
G 166-37	$-1.68 \pm 0.09$	2	$-0.91 \pm 0.08$	2	$-1.11 \pm 0.08$	1	-	-	$-1.12 \pm 0.03$	9
G 17-25	$-1.12 \pm 0.05$	2	$-0.34 \pm 0.05$	2	$-0.77 \pm 0.05$	2	-	-	$-0.64 \pm 0.05$	1
G 18-24	$-1.92 \pm 0.08$	1	$-1.39 \pm 0.02$	3	-	-	-	-	$-1.43 \pm 0.05$	7
G 188-30	$-2.23 \pm 0.06$	1	$-1.09 \pm 0.20$	3	-	-	-	-	$-1.50 \pm 0.03$	10
G 20-15	$-2.01 \pm 0.07$	1	$-1.35 \pm 0.04$	5	-	-	-	-	$-1.48 \pm 0.02$	8
G 206-23	-	-	$-1.60 \pm 0.03$	3	-	-	-	-	$-1.81 \pm 0.03$	4
G 238-30	-	-	$-2.89 \pm 0.05$	1	-	-	-	-	$-3.08 \pm 0.02$	3
G 25-24	$-2.51 \pm 0.07$	1	$-1.73 \pm 0.03$	5	-	-	-	-	$-1.87 \pm 0.03$	6
G 275-11	$-1.83 \pm 0.08$	2	$-1.21 \pm 0.07$	4	-	-	$-1.11 \pm 0.08$	1	$-1.21 \pm 0.04$	8
G 41-41	-	-	$-2.51 \pm 0.05$	2	-	-	-	-	$-2.63 \pm 0.05$	2
G 48-29	-	-	$-2.40 \pm 0.04$	2	-	-	-	-	$-2.50 \pm 0.06$	3
G 53-41	$-1.26 \pm 0.04$	3	$-1.12 \pm 0.05$	3	$-1.15 \pm 0.10$	2	$-0.95 \pm 0.10$	1	$-1.18 \pm 0.03$	14
G 59-27	-	-	$-1.69 \pm 0.04$	3	-	-	-	-	$-1.93 \pm 0.02$	6

Table 6. (Continued.)

Star name	[Na I/H]	$N$	[Mg I/H]	$N$	[Si I/H]	$N$	[Si II/H]	$N$	[Ca I/H]	$N$
G 64-12	-	-	$-2.80 \pm 0.03$	2	-	-	-	-	$-3.05 \pm 0.03$	4
G 64-37	-	-	$-2.83 \pm 0.03$	1	-	-	-	-	$-2.82 \pm 0.17$	3
HD 107752	-	-	$-2.56 \pm 0.12$	4	-	-	-	-	$-2.73 \pm 0.03$	7
HD 108577	$-2.77 \pm 0.09$	1	$-1.79 \pm 0.10$	5	-	-	-	-	$-1.97 \pm 0.03$	8
HD 111721	$-1.51 \pm 0.11$	2	-	-	$-0.95 \pm 0.11$	1	-	-	$-1.03 \pm 0.04$	9
HD 111980	$-1.28 \pm 0.08$	2	$-0.81 \pm 0.08$	2	$-0.82 \pm 0.03$	3	-	-	$-0.92 \pm 0.03$	10
HD 119516	-	-	$-1.74 \pm 0.14$	3	-	-	-	-	$-1.73 \pm 0.07$	1
HD 124358	$-2.40 \pm 0.07$	2	$-1.45 \pm 0.07$	2	$-1.57 \pm 0.01$	3	-	-	$-1.63 \pm 0.04$	9
HD 128279	$-2.78 \pm 0.08$	1	$-1.93 \pm 0.07$	4	-	-	-	-	$-2.09 \pm 0.03$	11
HD 134439	$-1.90 \pm 0.08$	2	$-1.06 \pm 0.08$	2	-	-	-	-	$-1.21 \pm 0.04$	10
HD 175305	$-1.67 \pm 0.09$	2	$-1.09 \pm 0.09$	1	$-1.20 \pm 0.09$	2	$-1.18 \pm 0.09$	1	$-1.20 \pm 0.03$	11
HD 214161	$-2.61 \pm 0.07$	2	$-1.85 \pm 0.09$	4	-	-	-	-	$-2.01 \pm 0.03$	7
HD 214362	-	-	$-1.60 \pm 0.03$	2	-	-	-	-	-	-
HD 218857	$-2.46 \pm 0.07$	1	$-1.71 \pm 0.06$	4	-	-	-	-	$-1.84 \pm 0.03$	8
HD 237846	-	-	$-2.65 \pm 0.15$	3	-	-	-	-	$-2.80 \pm 0.02$	6
HD 33771	$-2.52 \pm 0.09$	1	$-1.63 \pm 0.09$	2	$-1.87 \pm 0.09$	1	-	-	$-1.89 \pm 0.03$	11
HD 85773	$-2.93 \pm 0.05$	1	$-1.79 \pm 0.05$	2	-	-	-	-	$-2.32 \pm 0.02$	5
LP 443-65	$-2.03 \pm 0.06$	1	$-1.34 \pm 0.05$	5	-	-	-	-	$-1.41 \pm 0.03$	8
LP 763-87	-	-	$-2.02 \pm 0.07$	2	-	-	-	-	$-2.28 \pm 0.03$	7
LP 859-35	$-1.79 \pm 0.07$	2	$-1.40 \pm 0.06$	3	-	-	-	-	$-1.53 \pm 0.05$	7
LP 877-23	$-2.06 \pm 0.08$	2	$-1.26 \pm 0.12$	4	-	-	-	-	$-1.58 \pm 0.03$	8
LP 894-3	$-2.16 \pm 0.09$	1	$-1.44 \pm 0.05$	5	-	-	-	-	$-1.52 \pm 0.03$	11

**Table 7.** Derived Ti, Cr and Mn abundances

Star name	[Ti I/H]	<i>N</i>	[Ti II/H]	<i>N</i>	[Cr I/H]	<i>N</i>	[Cr II/H]	<i>N</i>	[Mn I/H]	<i>N</i>
BD+01° 3070	-1.46 ± 0.06	11	-1.19 ± 0.04	7	-1.82 ± 0.03	10	-1.52 ± 0.05	5	-2.32 ± 0.09	2
BD+04° 2466	-1.94 ± 0.08	1	-1.62 ± 0.08	2	-2.28 ± 0.03	5	-1.97 ± 0.08	1	-2.66 ± 0.08	1
BD+04° 2621	-2.59 ± 0.03	7	-2.28 ± 0.04	4	-3.02 ± 0.02	5	-2.59 ± 0.05	1	-3.18 ± 0.02	3
BD+09° 2870	-2.66 ± 0.02	10	-2.43 ± 0.04	8	-3.08 ± 0.02	7	-2.70 ± 0.08	2	-3.39 ± 0.08	1
BD+10° 2495	-2.07 ± 0.02	7	-1.84 ± 0.03	6	-2.44 ± 0.02	9	-2.04 ± 0.06	4	-2.75 ± 0.02	3
BD+12° 2547	-2.07 ± 0.03	8	-1.68 ± 0.05	5	-2.37 ± 0.02	7	-1.99 ± 0.04	3	-2.66 ± 0.08	2
BD+13° 2995	-0.82 ± 0.03	7	-0.47 ± 0.05	3	-1.18 ± 0.04	6	-0.96 ± 0.06	2	-1.60 ± 0.03	3
BD+29° 2356	-1.23 ± 0.06	10	-0.92 ± 0.05	4	-1.64 ± 0.02	6	-1.40 ± 0.10	2	-2.02 ± 0.03	3
BD+30° 2611	-1.27 ± 0.09	2	-1.13 ± 0.09	1	-1.44 ± 0.09	1	-	-	-1.95 ± 0.09	2
BD-03° 5215	-1.46 ± 0.09	2	-1.18 ± 0.09	2	-1.89 ± 0.03	5	-1.57 ± 0.05	4	-2.12 ± 0.08	1
BD-10° 548	-1.56 ± 0.03	3	-1.22 ± 0.10	1	-1.92 ± 0.10	4	-1.74 ± 0.09	2	-2.37 ± 0.03	3
BD-14° 5890	-2.32 ± 0.02	9	-2.07 ± 0.04	3	-2.77 ± 0.02	5	-2.30 ± 0.05	2	-3.06 ± 0.05	2
BD-17° 484	-1.38 ± 0.03	3	-1.09 ± 0.05	6	-1.90 ± 0.06	1	-1.56 ± 0.06	2	-2.24 ± 0.06	2
BD-18° 271	-2.75 ± 0.07	12	-2.23 ± 0.05	3	-3.13 ± 0.04	7	-2.65 ± 0.08	3	-3.26 ± 0.06	3
CD-24° 17504	-	-	-3.17 ± 0.05	3	-3.75 ± 0.05	1	-	-	-	-
G 112-43	-1.22 ± 0.03	7	-1.07 ± 0.03	9	-1.60 ± 0.04	10	-1.39 ± 0.05	5	-1.90 ± 0.02	3
G 115-58	-1.31 ± 0.03	4	-1.07 ± 0.04	10	-1.63 ± 0.01	3	-1.38 ± 0.07	2	-1.95 ± 0.07	2
G 125-13	-1.51 ± 0.02	3	-1.23 ± 0.03	6	-1.89 ± 0.02	5	-1.43 ± 0.07	1	-2.23 ± 0.07	2
G 14-39	-1.31 ± 0.03	5	-1.45 ± 0.08	3	-1.73 ± 0.03	4	-	-	-2.27 ± 0.04	1
G 15-13	-1.27 ± 0.03	10	-1.16 ± 0.06	5	-1.55 ± 0.03	11	-1.43 ± 0.08	1	-1.99 ± 0.08	2
G 154-34	-2.59 ± 0.03	9	-2.36 ± 0.06	4	-2.91 ± 0.01	8	-	-	-3.29 ± 0.06	2
G 165-39	-1.77 ± 0.03	5	-1.67 ± 0.04	9	-2.38 ± 0.05	2	-2.08 ± 0.05	2	-2.69 ± 0.05	2
G 166-37	-1.10 ± 0.03	11	-0.89 ± 0.05	4	-1.41 ± 0.03	8	-1.30 ± 0.08	1	-1.81 ± 0.02	3
G 17-25	-0.49 ± 0.05	2	-0.43 ± 0.05	2	-0.92 ± 0.02	5	-0.97 ± 0.05	1	-1.35 ± 0.07	4
G 18-24	-1.45 ± 0.03	5	-1.13 ± 0.02	3	-1.83 ± 0.07	2	-1.52 ± 0.07	1	-2.19 ± 0.07	2
G 188-30	-1.44 ± 0.03	12	-1.24 ± 0.04	5	-1.71 ± 0.03	10	-1.53 ± 0.06	1	-2.16 ± 0.02	4
G 20-15	-1.53 ± 0.02	3	-1.26 ± 0.03	6	-1.93 ± 0.03	3	-1.59 ± 0.07	2	-2.22 ± 0.07	2
G 206-23	-	-	-1.72 ± 0.05	2	-2.42 ± 0.05	1	-	-	-2.78 ± 0.05	1
G 238-30	-	-	-3.42 ± 0.04	3	-4.01 ± 0.05	1	-	-	-	-
G 25-24	-1.99 ± 0.07	2	-1.70 ± 0.04	4	-2.33 ± 0.02	4	-1.86 ± 0.07	1	-2.65 ± 0.01	3
G 275-11	-1.39 ± 0.08	2	-1.04 ± 0.05	5	-1.81 ± 0.08	2	-1.40 ± 0.08	2	-2.11 ± 0.08	2
G 41-41	-	-	-2.57 ± 0.08	3	-3.15 ± 0.05	1	-	-	-	-
G 48-29	-	-	-2.50 ± 0.07	3	-3.11 ± 0.04	1	-	-	-	-
G 53-41	-1.29 ± 0.03	6	-1.05 ± 0.03	10	-1.62 ± 0.02	7	-1.34 ± 0.10	2	-1.96 ± 0.10	2
G 59-27	-2.04 ± 0.06	1	-2.02 ± 0.04	5	-	-	-	-	-2.88 ± 0.05	1

Table 7. (Continued.)

Star name	[Ti I/H]	<i>N</i>	[Ti II/H]	<i>N</i>	[Cr I/H]	<i>N</i>	[Cr II/H]	<i>N</i>	[Mn I/H]	<i>N</i>
G 64-12	-	-	$-2.96 \pm 0.04$	2	$-3.66 \pm 0.03$	1	-	-	-	-
G 64-37	-	-	$-2.90 \pm 0.07$	3	-	-	-	-	-	-
HD 107752	$-3.13 \pm 0.03$	6	$-2.97 \pm 0.03$	11	$-3.44 \pm 0.02$	6	-	-	-	-
HD 108577	$-2.20 \pm 0.03$	7	$-2.12 \pm 0.04$	7	$-2.62 \pm 0.01$	6	$-2.36 \pm 0.06$	4	$-2.83 \pm 0.09$	1
HD 111721	$-1.21 \pm 0.03$	3	$-0.71 \pm 0.11$	1	$-1.49 \pm 0.05$	5	$-1.27 \pm 0.11$	1	$-1.97 \pm 0.04$	3
HD 111980	$-1.01 \pm 0.04$	4	$-0.67 \pm 0.08$	1	$-1.40 \pm 0.05$	6	$-1.11 \pm 0.07$	3	$-1.81 \pm 0.03$	3
HD 119516	$-1.93 \pm 0.07$	2	$-1.85 \pm 0.04$	6	$-2.33 \pm 0.03$	3	$-1.96 \pm 0.08$	3	$-2.57 \pm 0.07$	1
HD 124358	$-1.86 \pm 0.03$	7	$-1.57 \pm 0.03$	4	$-2.12 \pm 0.02$	9	$-1.75 \pm 0.06$	3	$-2.43 \pm 0.07$	1
HD 128279	$-2.27 \pm 0.02$	13	$-2.09 \pm 0.03$	11	$-2.73 \pm 0.02$	11	$-2.22 \pm 0.08$	1	$-3.04 \pm 0.08$	2
HD 134439	$-1.04 \pm 0.04$	10	$-0.95 \pm 0.05$	3	$-1.30 \pm 0.03$	13	$-1.16 \pm 0.08$	1	$-1.68 \pm 0.04$	4
HD 175305	$-1.27 \pm 0.08$	7	$-1.06 \pm 0.05$	4	$-1.62 \pm 0.03$	9	$-1.47 \pm 0.09$	2	$-2.07 \pm 0.04$	3
HD 214161	$-2.38 \pm 0.07$	8	$-1.91 \pm 0.07$	1	$-2.62 \pm 0.02$	5	$-2.24 \pm 0.03$	3	$-2.91 \pm 0.03$	3
HD 214362	$-1.75 \pm 0.03$	1	$-1.65 \pm 0.03$	2	$-2.25 \pm 0.03$	2	$-2.12 \pm 0.03$	2	$-2.52 \pm 0.03$	1
HD 218857	$-2.03 \pm 0.03$	7	$-1.68 \pm 0.04$	3	$-2.39 \pm 0.02$	5	$-1.94 \pm 0.06$	4	$-2.70 \pm 0.02$	3
HD 237846	$-3.08 \pm 0.02$	5	$-2.98 \pm 0.03$	9	$-3.59 \pm 0.04$	3	-	-	-	-
HD 33771	$-2.17 \pm 0.03$	11	$-1.87 \pm 0.03$	7	$-2.52 \pm 0.02$	9	$-2.07 \pm 0.06$	5	$-2.81 \pm 0.09$	1
HD 85773	$-2.71 \pm 0.04$	9	$-2.20 \pm 0.03$	6	$-2.92 \pm 0.02$	8	$-2.62 \pm 0.05$	1	$-3.01 \pm 0.05$	1
LP 443-65	$-1.49 \pm 0.03$	3	$-1.26 \pm 0.04$	7	$-1.98 \pm 0.06$	2	$-1.67 \pm 0.07$	3	$-2.23 \pm 0.06$	2
LP 763-87	$-2.19 \pm 0.07$	1	$-2.23 \pm 0.05$	4	$-2.87 \pm 0.07$	1	-	-	-	-
LP 859-35	$-1.60 \pm 0.02$	5	$-1.35 \pm 0.07$	3	$-1.99 \pm 0.02$	5	-	-	$-2.35 \pm 0.07$	2
LP 877-23	$-1.67 \pm 0.03$	8	$-1.37 \pm 0.06$	4	$-1.96 \pm 0.01$	5	$-1.85 \pm 0.07$	1	$-2.33 \pm 0.07$	2
LP 894-3	$-1.66 \pm 0.02$	4	$-1.44 \pm 0.04$	9	$-1.93 \pm 0.01$	5	$-1.60 \pm 0.09$	2	$-2.23 \pm 0.09$	2

**Table 8.** Derived Fe, Ni, Zn, Y and Ba abundances

Star name	[Fe I/H]	<i>N</i>	[Fe II/H]	<i>N</i>	[Ni I/H]	<i>N</i>	[Zn I/H]	<i>N</i>	[Y II/H]	<i>N</i>	[Ba II/H]	<i>N</i>
BD+01° 3070	-1.63 ± 0.01	63	-1.63 ± 0.04	9	-1.71 ± 0.05	11	-1.74 ± 0.09	2	-1.82 ± 0.09	2	-1.76 ± 0.09	3
BD+04° 2466	-2.10 ± 0.02	32	-2.10 ± 0.06	5	-1.96 ± 0.08	2	-2.12 ± 0.09	1	-1.56 ± 0.08	2	-0.75 ± 0.08	1
BD+04° 2621	-2.69 ± 0.01	49	-2.67 ± 0.03	5	-2.68 ± 0.06	4	-2.54 ± 0.07	1	-3.16 ± 0.06	1	-3.74 ± 0.05	4
BD+09° 2870	-2.69 ± 0.01	53	-2.70 ± 0.03	7	-2.75 ± 0.06	8	-2.75 ± 0.09	2	-3.25 ± 0.08	2	-3.67 ± 0.08	2
BD+10° 2495	-2.17 ± 0.01	66	-2.17 ± 0.04	9	-2.18 ± 0.04	9	-2.24 ± 0.08	2	-2.40 ± 0.08	2	-2.43 ± 0.05	4
BD+12° 2547	-2.11 ± 0.01	49	-2.06 ± 0.06	5	-2.20 ± 0.05	11	-2.13 ± 0.09	2	-2.26 ± 0.08	2	-2.13 ± 0.08	1
BD+13° 2995	-1.07 ± 0.01	26	-1.08 ± 0.02	6	-1.12 ± 0.06	10	-1.08 ± 0.07	2	-0.71 ± 0.06	1	-0.71 ± 0.06	2
BD+29° 2356	-1.44 ± 0.02	52	-1.41 ± 0.06	5	-1.48 ± 0.07	9	-1.52 ± 0.11	2	-1.38 ± 0.10	1	-1.30 ± 0.10	1
BD+30° 2611	-1.32 ± 0.02	24	-1.31 ± 0.09	2	-1.49 ± 0.04	3	-1.68 ± 0.10	1	-1.49 ± 0.09	1	-1.36 ± 0.09	1
BD-03° 5215	-1.60 ± 0.02	19	-1.58 ± 0.08	4	-1.65 ± 0.08	2	-1.70 ± 0.09	1	-1.70 ± 0.09	1	-1.56 ± 0.08	3
BD-10° 548	-1.72 ± 0.02	42	-1.71 ± 0.09	2	-1.78 ± 0.09	6	-1.86 ± 0.10	2	-1.81 ± 0.10	1	-1.67 ± 0.10	2
BD-14° 5890	-2.42 ± 0.01	48	-2.42 ± 0.02	6	-2.43 ± 0.07	5	-2.43 ± 0.07	2	-2.73 ± 0.06	1	-2.99 ± 0.03	4
BD-17° 484	-1.65 ± 0.01	35	-1.62 ± 0.04	8	-1.78 ± 0.06	1	-1.78 ± 0.07	2	-1.69 ± 0.07	1	-1.78 ± 0.07	2
BD-18° 271	-2.66 ± 0.02	53	-2.65 ± 0.05	8	-2.76 ± 0.07	8	-2.77 ± 0.10	1	-3.07 ± 0.09	1	-3.11 ± 0.09	2
CD-24° 17504	-3.66 ± 0.02	9	-3.67 ± 0.05	2	-	-	-	-	-	-	-4.94 ± 0.06	1
G 112-43	-1.52 ± 0.01	67	-1.51 ± 0.02	9	-1.49 ± 0.06	8	-1.36 ± 0.09	2	-1.69 ± 0.08	2	-1.79 ± 0.04	3
G 115-58	-1.46 ± 0.01	52	-1.46 ± 0.01	10	-1.61 ± 0.07	2	-1.74 ± 0.08	1	-1.66 ± 0.07	2	-1.43 ± 0.04	4
G 125-13	-1.69 ± 0.02	33	-1.69 ± 0.02	7	-1.74 ± 0.03	4	-1.77 ± 0.09	2	-1.82 ± 0.08	1	-1.88 ± 0.08	2
G 14-39	-1.82 ± 0.02	8	-2.17 ± 0.04	2	-1.78 ± 0.04	1	-	-	-	-	-1.97 ± 0.04	2
G 15-13	-1.48 ± 0.02	37	-1.62 ± 0.04	6	-1.51 ± 0.10	5	-1.68 ± 0.09	1	-1.57 ± 0.08	1	-1.36 ± 0.08	2
G 154-34	-2.76 ± 0.01	64	-2.77 ± 0.03	6	-2.82 ± 0.06	1	-	-	-2.89 ± 0.06	1	-3.33 ± 0.03	3
G 165-39	-2.20 ± 0.01	39	-2.19 ± 0.02	10	-2.28 ± 0.05	1	-2.23 ± 0.07	2	-2.14 ± 0.06	1	-2.37 ± 0.04	3
G 166-37	-1.31 ± 0.02	39	-1.31 ± 0.04	5	-1.35 ± 0.09	7	-1.45 ± 0.09	2	-1.23 ± 0.09	1	-1.25 ± 0.09	2
G 17-25	-0.90 ± 0.01	17	-1.15 ± 0.10	3	-0.85 ± 0.11	5	-1.09 ± 0.06	1	-0.67 ± 0.05	1	-0.72 ± 0.05	2
G 18-24	-1.61 ± 0.02	23	-1.62 ± 0.03	3	-1.74 ± 0.07	2	-1.67 ± 0.08	2	-1.03 ± 0.08	2	-0.44 ± 0.08	1
G 188-30	-1.61 ± 0.01	47	-1.75 ± 0.03	5	-1.66 ± 0.07	8	-1.84 ± 0.07	2	-1.74 ± 0.06	1	-1.78 ± 0.04	4
G 20-15	-1.76 ± 0.02	28	-1.75 ± 0.03	6	-1.81 ± 0.07	1	-1.77 ± 0.08	2	-1.83 ± 0.07	1	-1.80 ± 0.03	3
G 206-23	-2.18 ± 0.01	18	-2.17 ± 0.04	3	-	-	-2.21 ± 0.06	1	-2.27 ± 0.05	1	-2.21 ± 0.05	2
G 238-30	-3.77 ± 0.02	16	-3.77 ± 0.05	1	-	-	-	-	-	-	-	-
G 25-24	-2.07 ± 0.01	37	-2.06 ± 0.03	5	-2.21 ± 0.07	1	-2.21 ± 0.08	2	-2.36 ± 0.07	2	-2.22 ± 0.05	3
G 275-11	-1.55 ± 0.02	29	-1.53 ± 0.03	6	-1.62 ± 0.08	1	-1.71 ± 0.09	2	-1.65 ± 0.08	1	-1.62 ± 0.06	4
G 41-41	-2.98 ± 0.02	19	-3.01 ± 0.05	3	-	-	-	-	-	-	-3.57 ± 0.06	1
G 48-29	-3.03 ± 0.01	19	-3.02 ± 0.06	3	-	-	-	-	-	-	-3.59 ± 0.04	1
G 53-41	-1.44 ± 0.02	56	-1.44 ± 0.03	10	-1.50 ± 0.02	8	-1.49 ± 0.10	2	-1.31 ± 0.10	2	-1.21 ± 0.12	3
G 59-27	-2.42 ± 0.01	21	-2.40 ± 0.03	5	-	-	-	-	-2.57 ± 0.06	2	-2.90 ± 0.06	2

Table 8. (Continued.)

Star name	[Fe I/H]	<i>N</i>	[Fe II/H]	<i>N</i>	[Ni I/H]	<i>N</i>	[Zn I/H]	<i>N</i>	[Y II/H]	<i>N</i>	[Ba II/H]	<i>N</i>
G 64-12	$-3.56 \pm 0.01$	14	$-3.56 \pm 0.03$	2	-	-	-	-	-	-	$-3.81 \pm 0.04$	2
G 64-37	$-3.40 \pm 0.01$	15	$-3.39 \pm 0.03$	3	-	-	-	-	-	-	$-4.12 \pm 0.03$	2
HD 107752	$-3.10 \pm 0.01$	61	$-3.10 \pm 0.03$	9	$-3.26 \pm 0.08$	1	$-3.11 \pm 0.09$	2	$-3.50 \pm 0.08$	2	$-3.58 \pm 0.03$	4
HD 108577	$-2.35 \pm 0.02$	51	$-2.39 \pm 0.02$	8	$-2.28 \pm 0.06$	4	$-2.32 \pm 0.10$	2	$-2.77 \pm 0.09$	2	$-2.58 \pm 0.12$	3
HD 111721	$-1.35 \pm 0.02$	35	$-1.31 \pm 0.03$	3	$-1.34 \pm 0.09$	4	$-1.32 \pm 0.12$	2	$-1.08 \pm 0.11$	1	$-1.13 \pm 0.11$	2
HD 111980	$-1.25 \pm 0.02$	36	$-1.26 \pm 0.03$	5	$-1.28 \pm 0.07$	4	$-1.24 \pm 0.09$	2	$-0.98 \pm 0.08$	1	$-0.95 \pm 0.08$	2
HD 119516	$-2.09 \pm 0.02$	27	$-2.07 \pm 0.05$	6	$-2.20 \pm 0.07$	1	$-2.18 \pm 0.08$	2	$-2.26 \pm 0.07$	2	$-2.01 \pm 0.08$	3
HD 124358	$-1.78 \pm 0.01$	47	$-1.76 \pm 0.06$	6	$-1.96 \pm 0.06$	9	$-2.07 \pm 0.08$	2	$-2.35 \pm 0.07$	1	$-2.06 \pm 0.07$	2
HD 128279	$-2.44 \pm 0.01$	70	$-2.45 \pm 0.03$	11	$-2.41 \pm 0.06$	8	$-2.52 \pm 0.09$	2	-	-	$-3.26 \pm 0.04$	3
HD 134439	$-1.20 \pm 0.01$	45	$-1.35 \pm 0.04$	6	$-1.17 \pm 0.11$	5	$-1.50 \pm 0.09$	2	$-1.51 \pm 0.08$	1	$-1.35 \pm 0.08$	2
HD 175305	$-1.46 \pm 0.01$	60	$-1.44 \pm 0.01$	6	$-1.50 \pm 0.08$	7	$-1.56 \pm 0.09$	2	$-1.53 \pm 0.09$	1	$-1.41 \pm 0.09$	1
HD 214161	$-2.23 \pm 0.01$	55	$-2.23 \pm 0.02$	5	$-2.37 \pm 0.08$	6	$-2.48 \pm 0.07$	2	$-2.71 \pm 0.07$	1	$-2.62 \pm 0.04$	4
HD 214362	$-2.05 \pm 0.02$	5	$-2.06 \pm 0.03$	2	$-2.07 \pm 0.03$	1	$-2.06 \pm 0.05$	1	$-2.09 \pm 0.03$	2	$-1.92 \pm 0.03$	1
HD 218857	$-2.12 \pm 0.01$	60	$-2.11 \pm 0.02$	8	$-2.10 \pm 0.10$	4	$-2.13 \pm 0.08$	2	$-2.48 \pm 0.07$	1	$-2.70 \pm 0.05$	4
HD 237846	$-3.17 \pm 0.01$	55	$-3.19 \pm 0.02$	6	-	-	$-3.11 \pm 0.09$	1	$-3.72 \pm 0.08$	1	$-4.36 \pm 0.08$	2
HD 33771	$-2.23 \pm 0.01$	52	$-2.22 \pm 0.02$	6	$-2.25 \pm 0.06$	6	$-2.24 \pm 0.09$	2	$-2.41 \pm 0.09$	1	$-2.52 \pm 0.06$	3
HD 85773	$-2.59 \pm 0.01$	33	$-2.55 \pm 0.04$	4	$-2.56 \pm 0.09$	5	$-2.13 \pm 0.06$	2	$-3.27 \pm 0.05$	2	$-3.33 \pm 0.07$	3
LP 443-65	$-1.74 \pm 0.01$	41	$-1.72 \pm 0.03$	6	$-1.81 \pm 0.06$	1	$-1.86 \pm 0.07$	2	$-1.76 \pm 0.06$	1	$-1.81 \pm 0.03$	4
LP 763-87	$-2.69 \pm 0.02$	22	$-2.67 \pm 0.04$	4	-	-	-	-	$-2.68 \pm 0.07$	2	$-3.12 \pm 0.07$	2
LP 859-35	$-1.78 \pm 0.02$	23	$-1.78 \pm 0.03$	5	$-1.82 \pm 0.07$	1	$-1.79 \pm 0.08$	2	$-2.33 \pm 0.07$	1	$-2.00 \pm 0.09$	4
LP 877-23	$-1.78 \pm 0.01$	45	$-1.79 \pm 0.04$	4	$-1.86 \pm 0.04$	4	$-1.82 \pm 0.08$	2	$-1.97 \pm 0.08$	1	$-1.81 \pm 0.05$	4
LP 894-3	$-1.67 \pm 0.01$	59	$-1.66 \pm 0.02$	9	$-1.84 \pm 0.09$	2	$-2.00 \pm 0.09$	1	$-2.19 \pm 0.09$	1	$-2.05 \pm 0.09$	2



**Table 9.** Fe-normalized abundance ratios

Star name	[Fe/H]	[Na/Fe]	[Mg/Fe]	[Si/Fe]	[Ca/Fe]	[Ti/Fe]
BD+01° 3070	$-1.63 \pm 0.01$	$-0.25 \pm 0.09$	$0.37 \pm 0.03$	$0.25 \pm 0.09$	$0.24 \pm 0.03$	$0.35 \pm 0.04$
BD+04° 2466	$-2.10 \pm 0.02$	$-0.04 \pm 0.09$	$0.44 \pm 0.08$	$0.58 \pm 0.08$	$0.48 \pm 0.04$	$0.33 \pm 0.06$
BD+04° 2621	$-2.68 \pm 0.01$	$-0.21 \pm 0.06$	$0.59 \pm 0.09$	-	$0.40 \pm 0.03$	$0.21 \pm 0.03$
BD+09° 2870	$-2.70 \pm 0.01$	$-0.07 \pm 0.08$	$0.74 \pm 0.16$	-	$0.42 \pm 0.03$	$0.11 \pm 0.02$
BD+10° 2495	$-2.17 \pm 0.01$	$-0.16 \pm 0.08$	$0.47 \pm 0.06$	$0.35 \pm 0.07$	$0.29 \pm 0.03$	$0.19 \pm 0.02$
BD+12° 2547	$-2.10 \pm 0.01$	$-0.29 \pm 0.08$	$0.50 \pm 0.08$	$0.42 \pm 0.08$	$0.30 \pm 0.03$	$0.16 \pm 0.03$
BD+13° 2995	$-1.07 \pm 0.01$	$-0.13 \pm 0.06$	$0.55 \pm 0.06$	-	$0.20 \pm 0.03$	$0.35 \pm 0.03$
BD+29° 2356	$-1.44 \pm 0.02$	$-0.26 \pm 0.06$	$0.39 \pm 0.10$	$0.28 \pm 0.10$	$0.22 \pm 0.04$	$0.39 \pm 0.04$
BD+30° 2611	$-1.32 \pm 0.02$	-	$0.24 \pm 0.09$	$0.13 \pm 0.09$	$0.06 \pm 0.04$	$0.12 \pm 0.07$
BD−03° 5215	$-1.60 \pm 0.02$	$-0.42 \pm 0.09$	$0.33 \pm 0.09$	-	$0.36 \pm 0.09$	$0.28 \pm 0.06$
BD−10° 548	$-1.72 \pm 0.02$	$-0.26 \pm 0.10$	$0.43 \pm 0.05$	$0.34 \pm 0.03$	$0.31 \pm 0.03$	$0.19 \pm 0.03$
BD−14° 5890	$-2.42 \pm 0.01$	$-0.27 \pm 0.06$	$0.61 \pm 0.09$	-	$0.36 \pm 0.03$	$0.18 \pm 0.02$
BD−17° 484	$-1.65 \pm 0.01$	$-0.39 \pm 0.07$	$0.41 \pm 0.05$	-	$0.36 \pm 0.04$	$0.37 \pm 0.03$
BD−18° 271	$-2.66 \pm 0.01$	$-0.15 \pm 0.09$	$0.86 \pm 0.07$	$0.50 \pm 0.09$	$0.32 \pm 0.03$	$0.23 \pm 0.04$
CD−24° 17504	$-3.66 \pm 0.02$	-	$0.71 \pm 0.06$	-	$0.26 \pm 0.06$	$0.49 \pm 0.05$
G 112-43	$-1.51 \pm 0.01$	$-0.09 \pm 0.08$	$0.39 \pm 0.06$	$0.33 \pm 0.08$	$0.31 \pm 0.02$	$0.36 \pm 0.02$
G 115-58	$-1.46 \pm 0.01$	-	$0.19 \pm 0.04$	$0.04 \pm 0.07$	$0.20 \pm 0.03$	$0.25 \pm 0.02$
G 125-13	$-1.69 \pm 0.01$	$-0.16 \pm 0.08$	$0.39 \pm 0.04$	-	$0.26 \pm 0.04$	$0.31 \pm 0.02$
G 14-39	$-1.88 \pm 0.01$	$-0.03 \pm 0.04$	$0.53 \pm 0.04$	-	$0.44 \pm 0.05$	$0.55 \pm 0.03$
G 15-13	$-1.50 \pm 0.01$	$-0.77 \pm 0.08$	$0.34 \pm 0.08$	-	$0.17 \pm 0.03$	$0.25 \pm 0.03$
G 154-34	$-2.77 \pm 0.01$	-	$0.52 \pm 0.03$	-	$0.29 \pm 0.03$	$0.22 \pm 0.03$
G 165-39	$-2.20 \pm 0.01$	$-0.21 \pm 0.06$	$0.45 \pm 0.07$	-	$0.46 \pm 0.02$	$0.46 \pm 0.02$
G 166-37	$-1.31 \pm 0.01$	$-0.37 \pm 0.09$	$0.40 \pm 0.09$	$0.20 \pm 0.09$	$0.19 \pm 0.03$	$0.28 \pm 0.03$
G 17-25	$-0.91 \pm 0.01$	$-0.22 \pm 0.05$	$0.57 \pm 0.05$	$0.14 \pm 0.05$	$0.26 \pm 0.05$	$0.45 \pm 0.04$
G 18-24	$-1.62 \pm 0.02$	$-0.30 \pm 0.08$	$0.23 \pm 0.03$	-	$0.19 \pm 0.05$	$0.35 \pm 0.02$
G 188-30	$-1.64 \pm 0.01$	$-0.59 \pm 0.06$	$0.55 \pm 0.20$	-	$0.14 \pm 0.03$	$0.24 \pm 0.02$
G 20-15	$-1.75 \pm 0.01$	$-0.26 \pm 0.07$	$0.41 \pm 0.04$	-	$0.28 \pm 0.03$	$0.31 \pm 0.02$
G 206-23	$-2.18 \pm 0.01$	-	$0.58 \pm 0.03$	-	$0.36 \pm 0.03$	$0.45 \pm 0.06$
G 238-30	$-3.77 \pm 0.01$	-	$0.88 \pm 0.05$	-	$0.69 \pm 0.03$	$0.35 \pm 0.04$
G 25-24	$-2.06 \pm 0.01$	$-0.45 \pm 0.07$	$0.33 \pm 0.04$	-	$0.19 \pm 0.03$	$0.28 \pm 0.04$
G 275-11	$-1.54 \pm 0.01$	$-0.28 \pm 0.08$	$0.34 \pm 0.07$	$0.43 \pm 0.08$	$0.34 \pm 0.04$	$0.41 \pm 0.04$
G 41-41	$-2.98 \pm 0.01$	-	$0.47 \pm 0.06$	-	$0.35 \pm 0.06$	$0.41 \pm 0.08$
G 48-29	$-3.03 \pm 0.01$	-	$0.63 \pm 0.04$	-	$0.53 \pm 0.06$	$0.54 \pm 0.07$
G 53-41	$-1.44 \pm 0.01$	$0.18 \pm 0.05$	$0.32 \pm 0.06$	$0.39 \pm 0.07$	$0.25 \pm 0.03$	$0.24 \pm 0.02$
G 59-27	$-2.42 \pm 0.01$	-	$0.73 \pm 0.04$	-	$0.49 \pm 0.02$	$0.39 \pm 0.03$

Table 9. (Continued.)

Star name	[Fe/H]	[Na/Fe]	[Mg/Fe]	[Si/Fe]	[Ca/Fe]	[Ti/Fe]
G 64-12	$-3.56 \pm 0.01$	-	$0.76 \pm 0.04$	-	$0.51 \pm 0.03$	$0.60 \pm 0.04$
G 64-37	$-3.40 \pm 0.01$	-	$0.57 \pm 0.03$	-	$0.57 \pm 0.17$	$0.49 \pm 0.07$
HD 107752	$-3.10 \pm 0.01$	-	$0.54 \pm 0.12$	-	$0.37 \pm 0.03$	$0.04 \pm 0.02$
HD 108577	$-2.37 \pm 0.01$	$-0.40 \pm 0.09$	$0.57 \pm 0.10$	-	$0.40 \pm 0.03$	$0.20 \pm 0.02$
HD 111721	$-1.34 \pm 0.02$	$-0.17 \pm 0.11$	-	$0.39 \pm 0.11$	$0.31 \pm 0.04$	$0.17 \pm 0.03$
HD 111980	$-1.25 \pm 0.01$	$-0.03 \pm 0.08$	$0.44 \pm 0.08$	$0.43 \pm 0.03$	$0.33 \pm 0.04$	$0.31 \pm 0.04$
HD 119516	$-2.08 \pm 0.01$	-	$0.34 \pm 0.14$	-	$0.35 \pm 0.07$	$0.21 \pm 0.03$
HD 124358	$-1.78 \pm 0.01$	$-0.61 \pm 0.07$	$0.34 \pm 0.07$	$0.21 \pm 0.02$	$0.16 \pm 0.04$	$0.04 \pm 0.02$
HD 128279	$-2.44 \pm 0.01$	$-0.34 \pm 0.08$	$0.52 \pm 0.07$	-	$0.36 \pm 0.03$	$0.25 \pm 0.02$
HD 134439	$-1.21 \pm 0.01$	$-0.69 \pm 0.08$	$0.15 \pm 0.08$	-	$0.01 \pm 0.04$	$0.21 \pm 0.03$
HD 175305	$-1.45 \pm 0.01$	$-0.22 \pm 0.09$	$0.36 \pm 0.09$	$0.26 \pm 0.06$	$0.25 \pm 0.03$	$0.33 \pm 0.04$
HD 214161	$-2.23 \pm 0.01$	$-0.38 \pm 0.07$	$0.38 \pm 0.09$	-	$0.22 \pm 0.03$	$0.12 \pm 0.05$
HD 214362	$-2.05 \pm 0.01$	-	$0.45 \pm 0.03$	-	-	$0.35 \pm 0.03$
HD 218857	$-2.12 \pm 0.01$	$-0.35 \pm 0.07$	$0.41 \pm 0.06$	-	$0.27 \pm 0.03$	$0.21 \pm 0.02$
HD 237846	$-3.18 \pm 0.01$	-	$0.53 \pm 0.15$	-	$0.38 \pm 0.03$	$0.13 \pm 0.02$
HD 33771	$-2.23 \pm 0.01$	$-0.30 \pm 0.09$	$0.60 \pm 0.09$	$0.36 \pm 0.09$	$0.34 \pm 0.03$	$0.18 \pm 0.02$
HD 85773	$-2.58 \pm 0.01$	$-0.35 \pm 0.06$	$0.79 \pm 0.05$	-	$0.26 \pm 0.02$	$0.18 \pm 0.03$
LP 443-65	$-1.74 \pm 0.01$	$-0.29 \pm 0.06$	$0.40 \pm 0.05$	-	$0.33 \pm 0.04$	$0.34 \pm 0.02$
LP 763-87	$-2.68 \pm 0.01$	-	$0.67 \pm 0.07$	-	$0.40 \pm 0.03$	$0.46 \pm 0.04$
LP 859-35	$-1.78 \pm 0.01$	$-0.01 \pm 0.07$	$0.39 \pm 0.07$	-	$0.26 \pm 0.05$	$0.21 \pm 0.03$
LP 877-23	$-1.78 \pm 0.01$	$-0.28 \pm 0.08$	$0.52 \pm 0.12$	-	$0.20 \pm 0.04$	$0.17 \pm 0.03$
LP 894-3	$-1.67 \pm 0.01$	$-0.49 \pm 0.09$	$0.23 \pm 0.05$	-	$0.15 \pm 0.03$	$0.06 \pm 0.02$

**Table 10.** Fe-normalized abundance ratios

Star name	[Cr/Fe]	[Mn/Fe]	[Ni/Fe]	[Zn/Fe]	[Y/Fe]	[Ba/Fe]
BD+01° 3070	$-0.12 \pm 0.03$	$0.09 \pm 0.09$	$-0.08 \pm 0.05$	$-0.11 \pm 0.10$	$-0.19 \pm 0.09$	$-0.13 \pm 0.09$
BD+04° 2466	$-0.14 \pm 0.03$	$0.08 \pm 0.08$	$0.15 \pm 0.08$	$-0.01 \pm 0.09$	$0.54 \pm 0.09$	$1.36 \pm 0.09$
BD+04° 2621	$-0.27 \pm 0.02$	$0.03 \pm 0.03$	$-0.00 \pm 0.06$	$0.15 \pm 0.07$	$-0.48 \pm 0.06$	$-1.06 \pm 0.05$
BD+09° 2870	$-0.37 \pm 0.02$	$0.08 \pm 0.08$	$-0.05 \pm 0.06$	$-0.06 \pm 0.09$	$-0.56 \pm 0.08$	$-0.98 \pm 0.08$
BD+10° 2495	$-0.22 \pm 0.02$	$0.02 \pm 0.02$	$-0.01 \pm 0.04$	$-0.07 \pm 0.09$	$-0.23 \pm 0.08$	$-0.26 \pm 0.05$
BD+12° 2547	$-0.19 \pm 0.02$	$0.08 \pm 0.08$	$-0.09 \pm 0.05$	$-0.02 \pm 0.09$	$-0.15 \pm 0.08$	$-0.03 \pm 0.08$
BD+13° 2995	$-0.03 \pm 0.03$	$0.04 \pm 0.04$	$-0.04 \pm 0.06$	$-0.00 \pm 0.07$	$0.37 \pm 0.06$	$0.36 \pm 0.06$
BD+29° 2356	$-0.19 \pm 0.03$	$0.04 \pm 0.04$	$-0.04 \pm 0.07$	$-0.09 \pm 0.11$	$0.06 \pm 0.10$	$0.14 \pm 0.10$
BD+30° 2611	$-0.12 \pm 0.09$	$0.09 \pm 0.09$	$-0.17 \pm 0.05$	$-0.36 \pm 0.10$	$-0.17 \pm 0.10$	$-0.04 \pm 0.10$
BD−03° 5215	$-0.20 \pm 0.03$	$0.09 \pm 0.09$	$-0.05 \pm 0.09$	$-0.10 \pm 0.09$	$-0.10 \pm 0.09$	$0.04 \pm 0.09$
BD−10° 548	$-0.11 \pm 0.07$	$0.03 \pm 0.03$	$-0.07 \pm 0.09$	$-0.14 \pm 0.10$	$-0.10 \pm 0.10$	$0.05 \pm 0.10$
BD−14° 5890	$-0.26 \pm 0.02$	$0.05 \pm 0.05$	$-0.01 \pm 0.07$	$-0.00 \pm 0.07$	$-0.31 \pm 0.06$	$-0.56 \pm 0.03$
BD−17° 484	$-0.08 \pm 0.05$	$0.07 \pm 0.07$	$-0.14 \pm 0.07$	$-0.13 \pm 0.08$	$-0.05 \pm 0.07$	$-0.13 \pm 0.07$
BD−18° 271	$-0.37 \pm 0.04$	$0.06 \pm 0.06$	$-0.11 \pm 0.07$	$-0.12 \pm 0.10$	$-0.42 \pm 0.09$	$-0.45 \pm 0.09$
CD−24° 17504	$-0.09 \pm 0.06$	-	-	-	-	$-1.28 \pm 0.06$
G 112-43	$-0.02 \pm 0.03$	$0.03 \pm 0.03$	$0.02 \pm 0.07$	$0.15 \pm 0.09$	$-0.17 \pm 0.08$	$-0.28 \pm 0.04$
G 115-58	$-0.16 \pm 0.01$	$0.07 \pm 0.07$	$-0.15 \pm 0.07$	$-0.28 \pm 0.08$	$-0.20 \pm 0.07$	$0.03 \pm 0.04$
G 125-13	$-0.16 \pm 0.02$	$0.08 \pm 0.08$	$-0.05 \pm 0.03$	$-0.08 \pm 0.09$	$-0.13 \pm 0.08$	$-0.19 \pm 0.08$
G 14-39	$0.15 \pm 0.04$	$0.04 \pm 0.04$	$0.10 \pm 0.04$	-	-	$-0.10 \pm 0.04$
G 15-13	$-0.04 \pm 0.03$	$0.08 \pm 0.08$	$-0.01 \pm 0.10$	$-0.18 \pm 0.09$	$-0.07 \pm 0.08$	$0.14 \pm 0.08$
G 154-34	$-0.14 \pm 0.02$	$0.06 \pm 0.06$	$-0.06 \pm 0.06$	-	$-0.12 \pm 0.06$	$-0.56 \pm 0.03$
G 165-39	$-0.03 \pm 0.04$	$0.05 \pm 0.05$	$-0.08 \pm 0.05$	$-0.03 \pm 0.07$	$0.06 \pm 0.06$	$-0.18 \pm 0.04$
G 166-37	$-0.08 \pm 0.03$	$0.03 \pm 0.03$	$-0.04 \pm 0.09$	$-0.14 \pm 0.09$	$0.08 \pm 0.09$	$0.06 \pm 0.09$
G 17-25	$-0.02 \pm 0.02$	$0.07 \pm 0.07$	$0.05 \pm 0.11$	$-0.18 \pm 0.06$	$0.24 \pm 0.05$	$0.19 \pm 0.05$
G 18-24	$-0.06 \pm 0.05$	$0.08 \pm 0.08$	$-0.12 \pm 0.08$	$-0.06 \pm 0.09$	$0.58 \pm 0.08$	$1.17 \pm 0.08$
G 188-30	$-0.04 \pm 0.03$	$0.02 \pm 0.02$	$-0.03 \pm 0.07$	$-0.21 \pm 0.07$	$-0.11 \pm 0.06$	$-0.14 \pm 0.05$
G 20-15	$-0.13 \pm 0.03$	$0.07 \pm 0.07$	$-0.06 \pm 0.07$	$-0.01 \pm 0.08$	$-0.08 \pm 0.07$	$-0.04 \pm 0.03$
G 206-23	$-0.24 \pm 0.05$	$0.05 \pm 0.05$	-	$-0.03 \pm 0.07$	$-0.09 \pm 0.06$	$-0.04 \pm 0.06$
G 238-30	$-0.24 \pm 0.05$	-	-	-	-	-
G 25-24	$-0.22 \pm 0.02$	$0.02 \pm 0.02$	$-0.15 \pm 0.07$	$-0.15 \pm 0.08$	$-0.30 \pm 0.07$	$-0.16 \pm 0.05$
G 275-11	$-0.06 \pm 0.06$	$0.08 \pm 0.08$	$-0.08 \pm 0.08$	$-0.16 \pm 0.09$	$-0.11 \pm 0.08$	$-0.07 \pm 0.06$
G 41-41	$-0.16 \pm 0.06$	-	-	-	-	$-0.58 \pm 0.06$
G 48-29	$-0.08 \pm 0.04$	-	-	-	-	$-0.56 \pm 0.04$
G 53-41	$-0.17 \pm 0.03$	$0.10 \pm 0.10$	$-0.06 \pm 0.03$	$-0.06 \pm 0.10$	$0.13 \pm 0.10$	$0.23 \pm 0.12$
G 59-27	-	$0.06 \pm 0.06$	-	-	$-0.15 \pm 0.06$	$-0.48 \pm 0.06$

Table 10. (Continued.)

Star name	[Cr/Fe]	[Mn/Fe]	[Ni/Fe]	[Zn/Fe]	[Y/Fe]	[Ba/Fe]
G 64-12	$-0.10 \pm 0.04$	-	-	-	-	$-0.25 \pm 0.04$
G 64-37	-	-	-	-	-	$-0.73 \pm 0.04$
HD 107752	$-0.34 \pm 0.02$	-	$-0.16 \pm 0.08$	$-0.01 \pm 0.09$	$-0.40 \pm 0.08$	$-0.48 \pm 0.03$
HD 108577	$-0.23 \pm 0.02$	$0.09 \pm 0.09$	$0.09 \pm 0.07$	$0.05 \pm 0.10$	$-0.40 \pm 0.09$	$-0.21 \pm 0.12$
HD 111721	$-0.12 \pm 0.04$	$0.05 \pm 0.05$	$0.00 \pm 0.09$	$0.02 \pm 0.12$	$0.26 \pm 0.11$	$0.21 \pm 0.11$
HD 111980	$-0.05 \pm 0.04$	$0.03 \pm 0.03$	$-0.03 \pm 0.07$	$0.01 \pm 0.09$	$0.26 \pm 0.08$	$0.30 \pm 0.08$
HD 119516	$-0.18 \pm 0.03$	$0.07 \pm 0.07$	$-0.11 \pm 0.07$	$-0.10 \pm 0.08$	$-0.17 \pm 0.07$	$0.07 \pm 0.08$
HD 124358	$-0.28 \pm 0.02$	$0.07 \pm 0.07$	$-0.18 \pm 0.06$	$-0.29 \pm 0.08$	$-0.57 \pm 0.07$	$-0.27 \pm 0.07$
HD 128279	$-0.26 \pm 0.02$	$0.08 \pm 0.08$	$0.04 \pm 0.06$	$-0.07 \pm 0.09$	-	$-0.82 \pm 0.04$
HD 134439	$-0.06 \pm 0.03$	$0.04 \pm 0.04$	$0.04 \pm 0.11$	$-0.29 \pm 0.09$	$-0.29 \pm 0.08$	$-0.14 \pm 0.08$
HD 175305	$-0.15 \pm 0.03$	$0.04 \pm 0.04$	$-0.04 \pm 0.08$	$-0.11 \pm 0.10$	$-0.08 \pm 0.09$	$0.05 \pm 0.09$
HD 214161	$-0.23 \pm 0.02$	$0.03 \pm 0.03$	$-0.14 \pm 0.08$	$-0.24 \pm 0.07$	$-0.48 \pm 0.07$	$-0.39 \pm 0.04$
HD 214362	$-0.14 \pm 0.02$	$0.03 \pm 0.03$	$-0.02 \pm 0.03$	$-0.01 \pm 0.05$	$-0.04 \pm 0.04$	$0.13 \pm 0.04$
HD 218857	$-0.21 \pm 0.02$	$0.02 \pm 0.02$	$0.01 \pm 0.10$	$-0.01 \pm 0.08$	$-0.37 \pm 0.07$	$-0.58 \pm 0.05$
HD 237846	$-0.41 \pm 0.04$	-	-	$0.07 \pm 0.09$	$-0.54 \pm 0.08$	$-1.19 \pm 0.08$
HD 33771	$-0.24 \pm 0.02$	$0.09 \pm 0.09$	$-0.02 \pm 0.06$	$-0.01 \pm 0.10$	$-0.18 \pm 0.09$	$-0.29 \pm 0.06$
HD 85773	$-0.27 \pm 0.02$	$0.05 \pm 0.05$	$0.02 \pm 0.09$	$0.45 \pm 0.07$	$-0.69 \pm 0.06$	$-0.75 \pm 0.07$
LP 443-65	$-0.11 \pm 0.05$	$0.06 \pm 0.06$	$-0.07 \pm 0.06$	$-0.12 \pm 0.07$	$-0.02 \pm 0.06$	$-0.07 \pm 0.03$
LP 763-87	$-0.18 \pm 0.07$	-	-	-	$0.01 \pm 0.07$	$-0.43 \pm 0.07$
LP 859-35	$-0.20 \pm 0.02$	$0.07 \pm 0.07$	$-0.03 \pm 0.07$	$-0.01 \pm 0.08$	$-0.55 \pm 0.07$	$-0.22 \pm 0.09$
LP 877-23	$-0.17 \pm 0.02$	$0.08 \pm 0.08$	$-0.08 \pm 0.04$	$-0.03 \pm 0.09$	$-0.18 \pm 0.08$	$-0.03 \pm 0.05$
LP 894-3	$-0.25 \pm 0.02$	$0.09 \pm 0.09$	$-0.17 \pm 0.09$	$-0.33 \pm 0.09$	$-0.53 \pm 0.09$	$-0.38 \pm 0.09$

**Table 11.** Averages and scatters of abundances for the inner/outer halo samples.

Element	$Z_{\max}$ (kpc)	$-4 < [\text{Fe}/\text{H}] \leq -3^*$			$-3 < [\text{Fe}/\text{H}] \leq -2$			$-2 < [\text{Fe}/\text{H}] \leq -1$			$-1 < [\text{Fe}/\text{H}] \leq 0$		
		$\mu^\dagger$	$\frac{\sigma}{\sqrt{N}}^\ddagger$	$N^\S$	$\mu$	$\frac{\sigma}{\sqrt{N}}$	$N$	$\mu$	$\frac{\sigma}{\sqrt{N}}$	$N$	$\mu$	$\frac{\sigma}{\sqrt{N}}$	$N$
Na	$\leq 5$	-	-	0	0.15	0.14	7	-0.10	0.02	52	0.07	0.02	65
	$> 5$	-	-	0	-0.23	0.04	18	-0.31	0.04	39	-0.26	0.03	2
Mg	$\leq 5$	-	-	1	0.44	0.02	16	0.42	0.02	51	0.39	0.01	65
	$> 5$	0.66	0.05	7	0.49	0.03	29	0.31	0.02	40	0.31	0.25	2
Si	$\leq 5$	-	-	0	0.46	0.04	6	0.30	0.02	46	0.24	0.01	65
	$> 5$	-	-	0	0.43	0.03	7	0.25	0.02	26	0.06	0.08	2
Ca	$\leq 5$	-	-	1	0.37	0.02	16	0.31	0.01	52	0.23	0.01	65
	$> 5$	0.47	0.05	7	0.35	0.01	28	0.23	0.01	41	0.18	0.08	2
Ti	$\leq 5$	-	-	1	0.33	0.03	16	0.27	0.01	52	0.19	0.01	65
	$> 5$	0.38	0.08	7	0.27	0.02	29	0.24	0.02	41	0.29	0.16	2
Cr	$\leq 5$	-	-	1	-0.01	0.02	16	-0.02	0.01	52	-0.02	0.01	65
	$> 5$	-0.21	0.06	6	-0.17	0.02	28	-0.07	0.02	41	-0.04	0.01	2
Mn	$\leq 5$	-	-	1	-0.48	0.05	5	-0.39	0.02	27	-0.21	0.04	12
	$> 5$	-	-	0	-0.55	0.02	20	-0.54	0.02	25	-	-	1
Ni	$\leq 5$	-	-	1	0.09	0.04	14	-0.05	0.01	48	-0.03	0.01	62
	$> 5$	-	-	1	-0.02	0.02	25	-0.08	0.01	41	-0.08	0.14	2
Zn	$\leq 5$	-	-	1	0.16	0.07	5	0.09	0.02	22	0.16	0.04	12
	$> 5$	0.03	0.04	2	-0.02	0.03	18	-0.13	0.03	23	-	-	1
Y	$\leq 5$	-	-	0	-0.22	0.04	2	0.03	0.05	16	-0.00	0.03	2
	$> 5$	-0.47	0.07	2	-0.23	0.06	21	-0.12	0.04	38	0.07	0.17	2
Ba	$\leq 5$	-	-	1	-0.34	0.05	7	0.09	0.04	16	0.15	0.02	2
	$> 5$	-0.75	0.17	6	-0.26	0.08	29	0.02	0.04	39	0.17	0.02	2

\* A metallicity interval

† An average  $[\text{X}/\text{Fe}]$  value of the inner or outer halo sample with the given metallicity interval.

‡ A standard deviation divided by the number of objects in each of the inner/outer halo domain with the given metallicity interval.

§ Number of objects

**Table 12.** Dependence of  $P_{\text{KS}}$  on the adopted halo boundary

Boundary $Z_{\max}$ (kpc)	$P_{\text{KS}}^*$			
	$[\text{Mg}/\text{Fe}]$	$[\text{Si}/\text{Fe}]$	$[\text{Ca}/\text{Fe}]$	$[\text{Ti}/\text{Fe}]$
3	$0.13 \times 10^{-3}$	$0.70 \times 10^{-1}$	$0.36 \times 10^{-3}$	0.79
5	$0.30 \times 10^{-4}$	0.39	$0.60 \times 10^{-3}$	0.15
10	$0.45 \times 10^{-2}$	$0.90 \times 10^{-1}$	$0.11 \times 10^{-1}$	0.57

\* Kolmogorov-Smirnoff probabilities for the inner/outer halo division on the boundary  $Z_{\max}$  value.

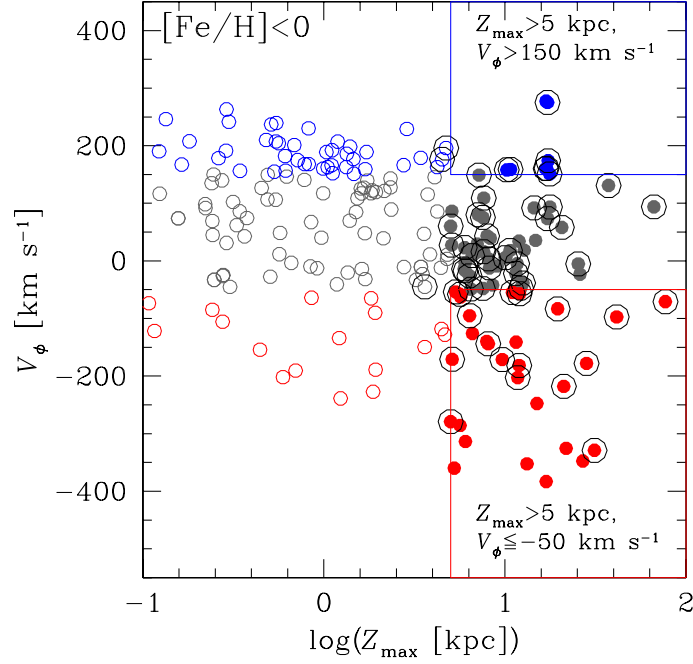


**Fig. 1.** A  $Z_{\max}$ – $V_{\phi}$  plot for the sample stars with  $[\text{Fe}/\text{H}] < 0$ . All of the sample stars in this plot have known kinematics (3-dimensional velocity components, distances) and the measured abundances from our high resolution spectroscopy with Subaru HDS or from literature (SB02; G03). *Open* and *filled* symbols represent stars with  $Z_{\max} \leq 5$  kpc and  $Z_{\max} > 5$  kpc, respectively. *Blue*, *gray* and *red* colors represent stars with  $V_{\phi} > 150$  km s $^{-1}$ ,  $-50 < V_{\phi} \leq 150$  km s $^{-1}$  and  $V_{\phi} \leq -50$  km s $^{-1}$ , respectively. The stars observed with Subaru/HDS are shown by symbols encircled with large black open circles.



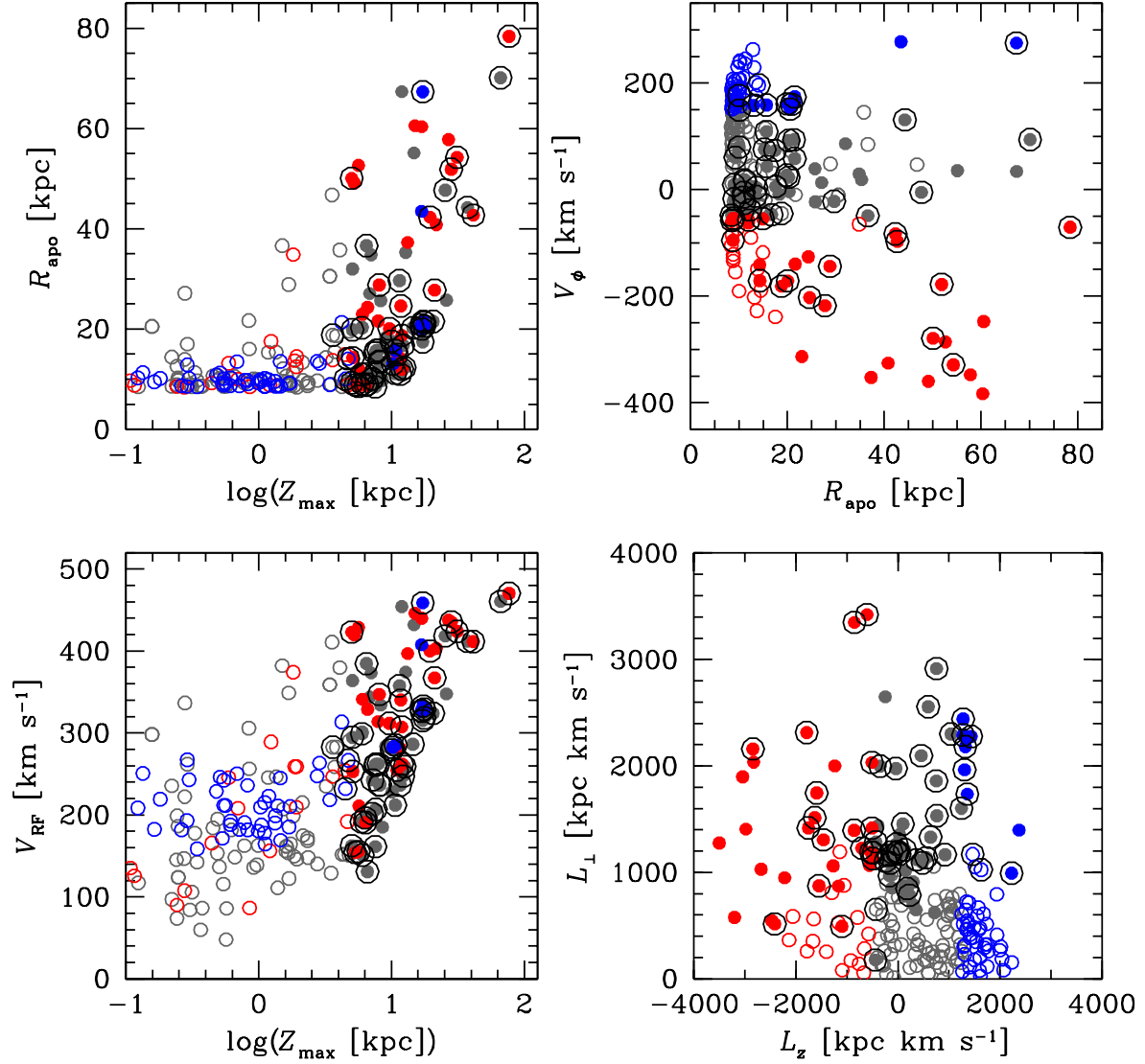


**Fig. 2.** The *top-left*, *top-right* and *bottom-left* panels show correlations between orbital parameters  $Z_{\text{max}}-R_{\text{apo}}$ ,  $V_{\phi}-R_{\text{apo}}$  and  $Z_{\text{max}}-V_{\text{RF}}$ , respectively, for the sample stars. The *bottom-right* panel shows locations of the sample stars on an angular momentum space ( $L_z-L_{\perp}$ ). The symbols are the same as in Figure 1.

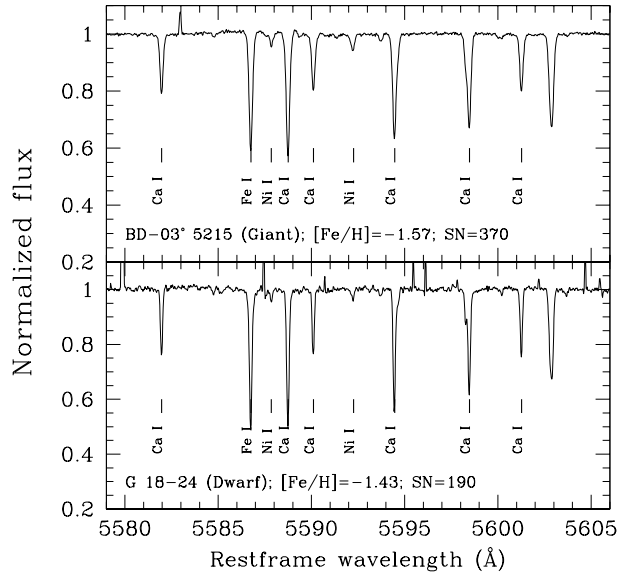


**Fig. 3.** Example of spectra obtained in the observation with Subaru/HDS. Top panel shows a spectrum of BD-03° 5215 (giant) with  $[\text{Fe}/\text{H}] = -1.60$  and  $\text{S}/\text{N} = 369$ . Bottom panel shows a spectrum of G 18-24 (dwarf) with  $[\text{Fe}/\text{H}] = -1.62$  and  $\text{S}/\text{N} = 186$ .

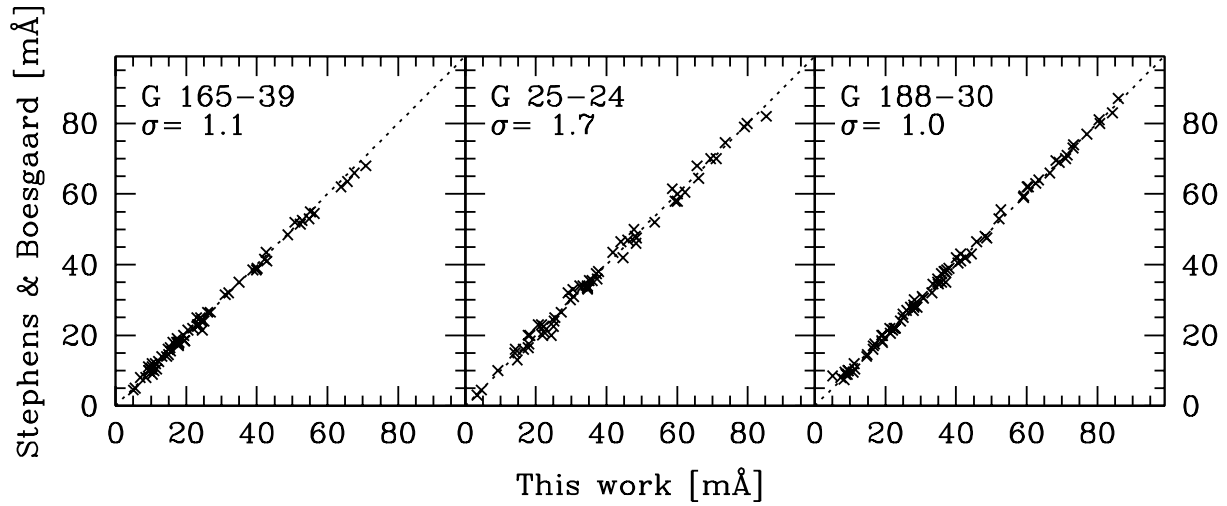


**Fig. 4.** Comparisons of measured EWs (mÅ) in this work and in SB02 for three stars in common, G 165-39 (left), G 25-24 (middle) and G 188-30 (right).

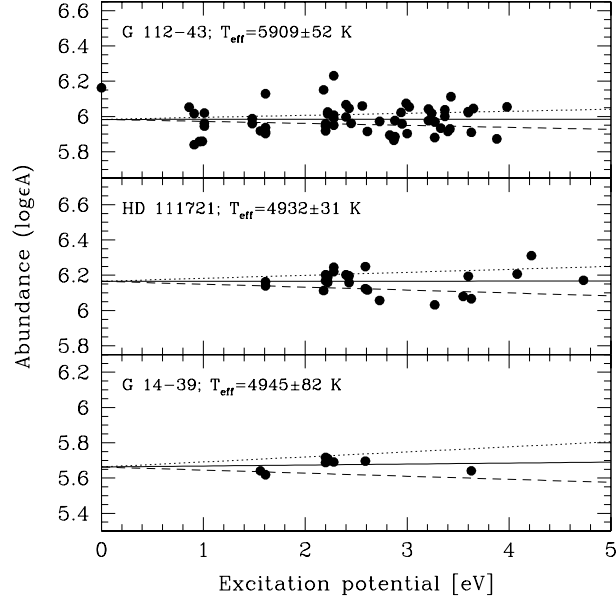


**Fig. 5.** Excitation potential ( $\chi$ ) vs  $\log \epsilon_A$ . *Top*, *middle* and *bottom* panels show the results of G 112-43, HD 111721 and G 14-39, respectively. *Dotted* and *dashed* lines display slopes when  $T_{\text{eff}}$  is changed by an amount of the error to the positive and negative direction, respectively.

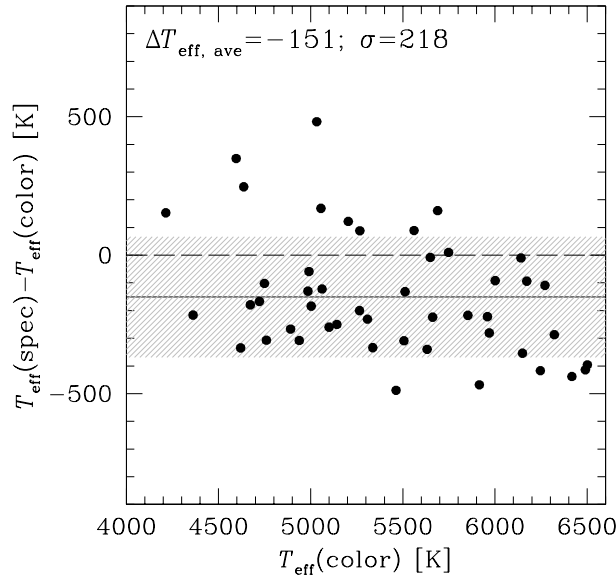


**Fig. 6.** Deviation in  $T_{\text{eff}}$  estimated in our work,  $T_{\text{eff}}(\text{spec})$ , from that obtained with  $(V-K)$  color,  $T_{\text{eff}}(\text{color})$ .

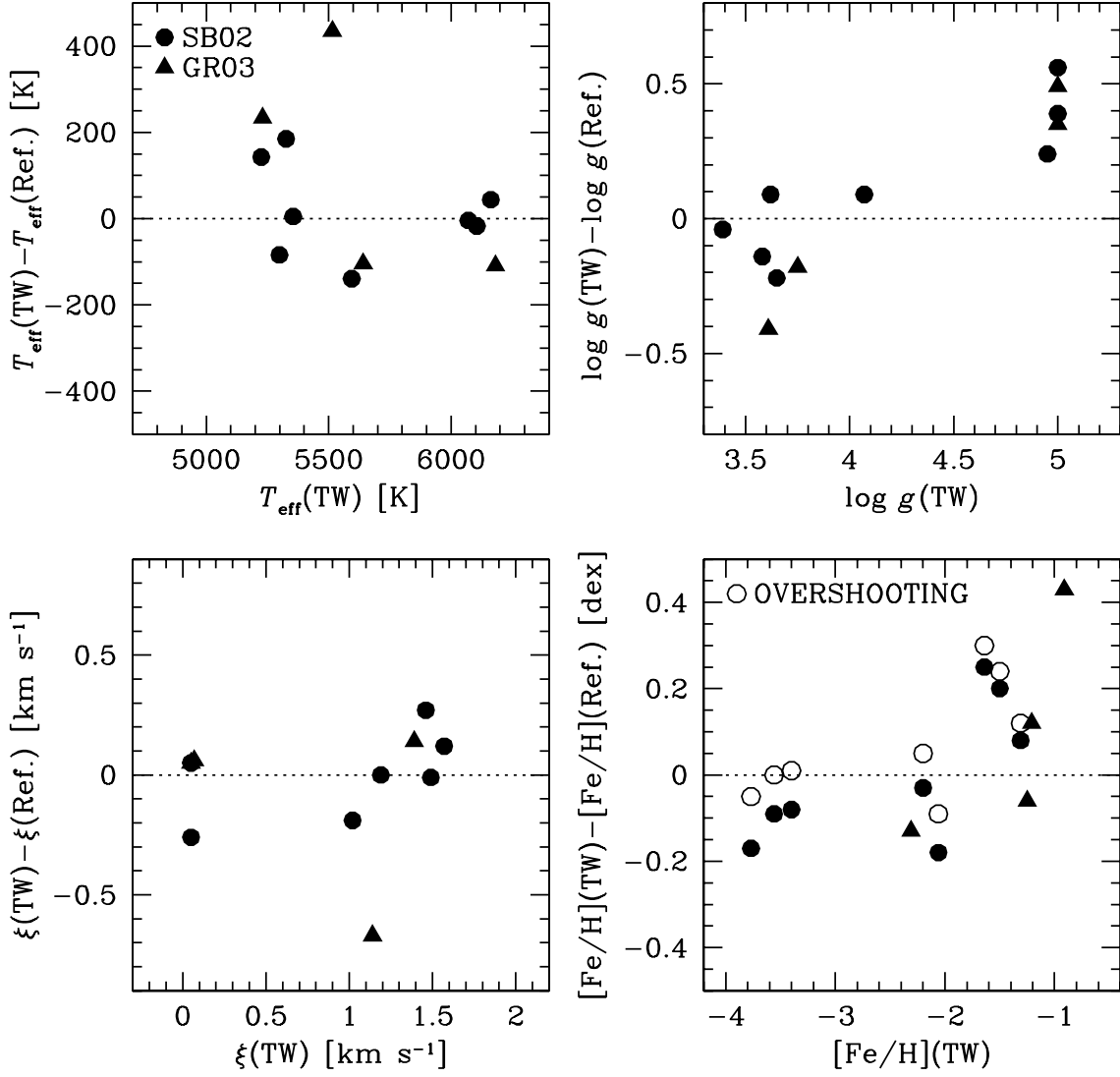


**Fig. 7.** Deviation in the stellar parameters,  $T_{\text{eff}}$ ,  $\log g$ ,  $\xi$  and  $[\text{Fe}/\text{H}]$ , estimated in this work (TW) from those estimated in SB02 (*filled circles*) and G03 (*filled triangles*). For the comparison of the  $[\text{Fe}/\text{H}]$  estimates (*bottom-right* panel), deviations when the overshooting model is applied are shown by *open circles*. (Section 3.4.1)

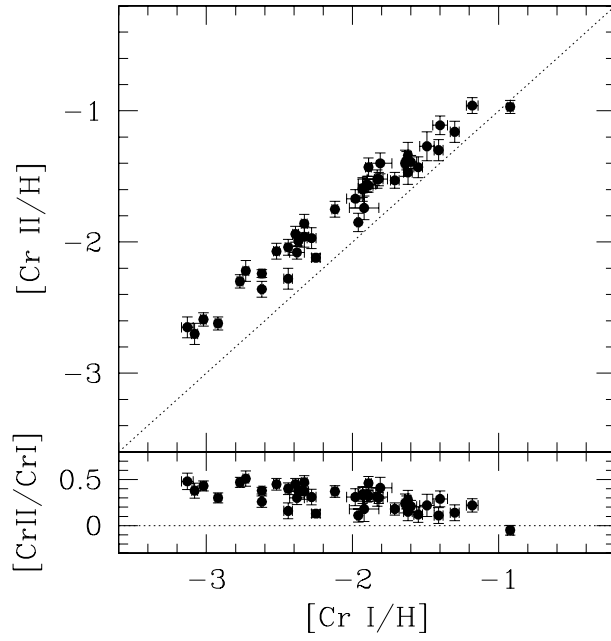


**Fig. 8.** *Upper panel:* Cr abundances estimated from Cr II lines ( $[\text{Cr II}/\text{H}]$ ) as a function of those estimated from Cr I lines ( $[\text{Cr I}/\text{H}]$ ). *Lower panel:* Differences in the two estimates ( $[\text{Cr II}/\text{H}] - [\text{Cr I}/\text{H}] = [\text{Cr II}/\text{Cr I}]$ ) as a function of  $[\text{Cr I}/\text{H}]$

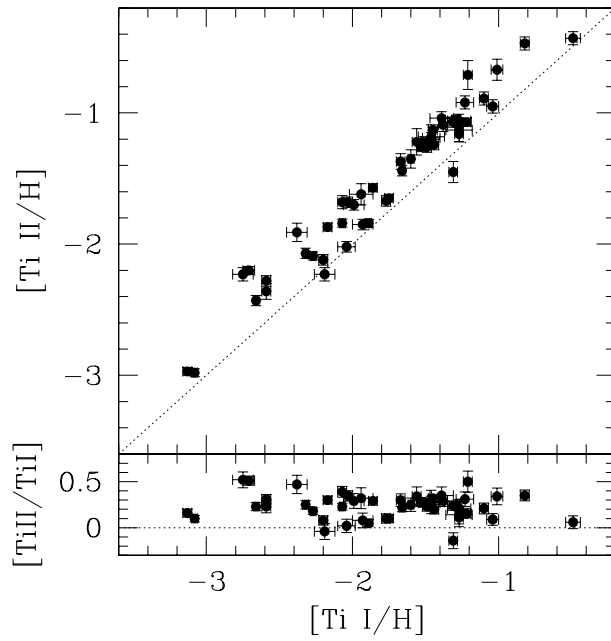


**Fig. 9.** Same as Figure 8 but for Ti.

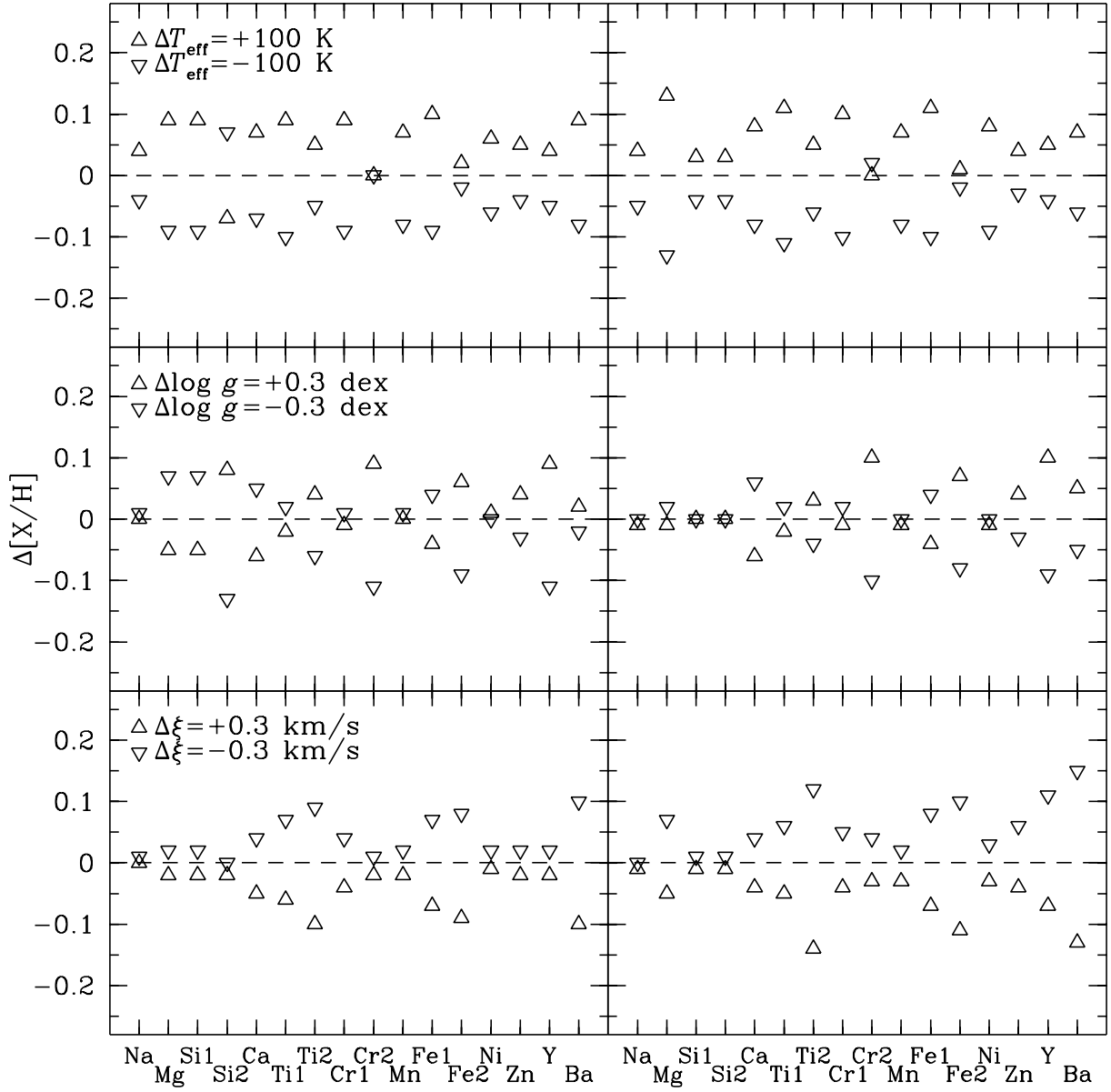


**Fig. 10.** Abundance deviation ( $\Delta[X/H]$ ) for a dwarf, G 275-11 (*left*), and a giant star, HD 111980 (*right*), in our sample when stellar atmospheric parameters  $T_{\text{eff}}$  (*top*),  $\log g$  (*middle*) and  $\xi$  (*bottom*) are changed by  $\pm 100\text{K}$ ,  $\pm 0.3 \text{ dex}$  and  $\pm 0.3 \text{ km s}^{-1}$ , respectively. *Triangles* show the results of changes in parameters to positive direction and *inverted triangles* show those to the negative direction.

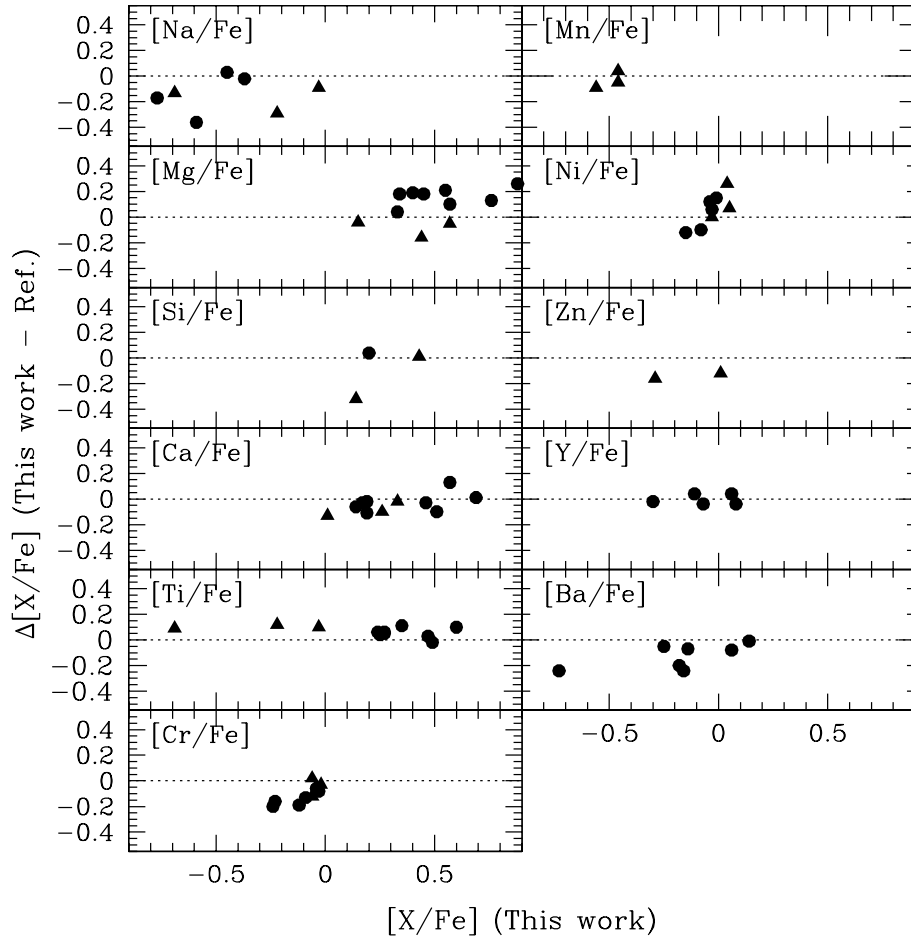


**Fig. 11.** Differences in abundance ratios  $[X/Fe]$  derived in literature and in this work. *Circles* show those derived in SB02 for eight stars (G 15-13, G 165-39, G 166-37, G 188-30, G 238-30, G 25-24, G 64-12, G64-37) and *triangles* show those derived in G03 for four stars (G 17-25, G 43-3, HD 111980, HD 134439)

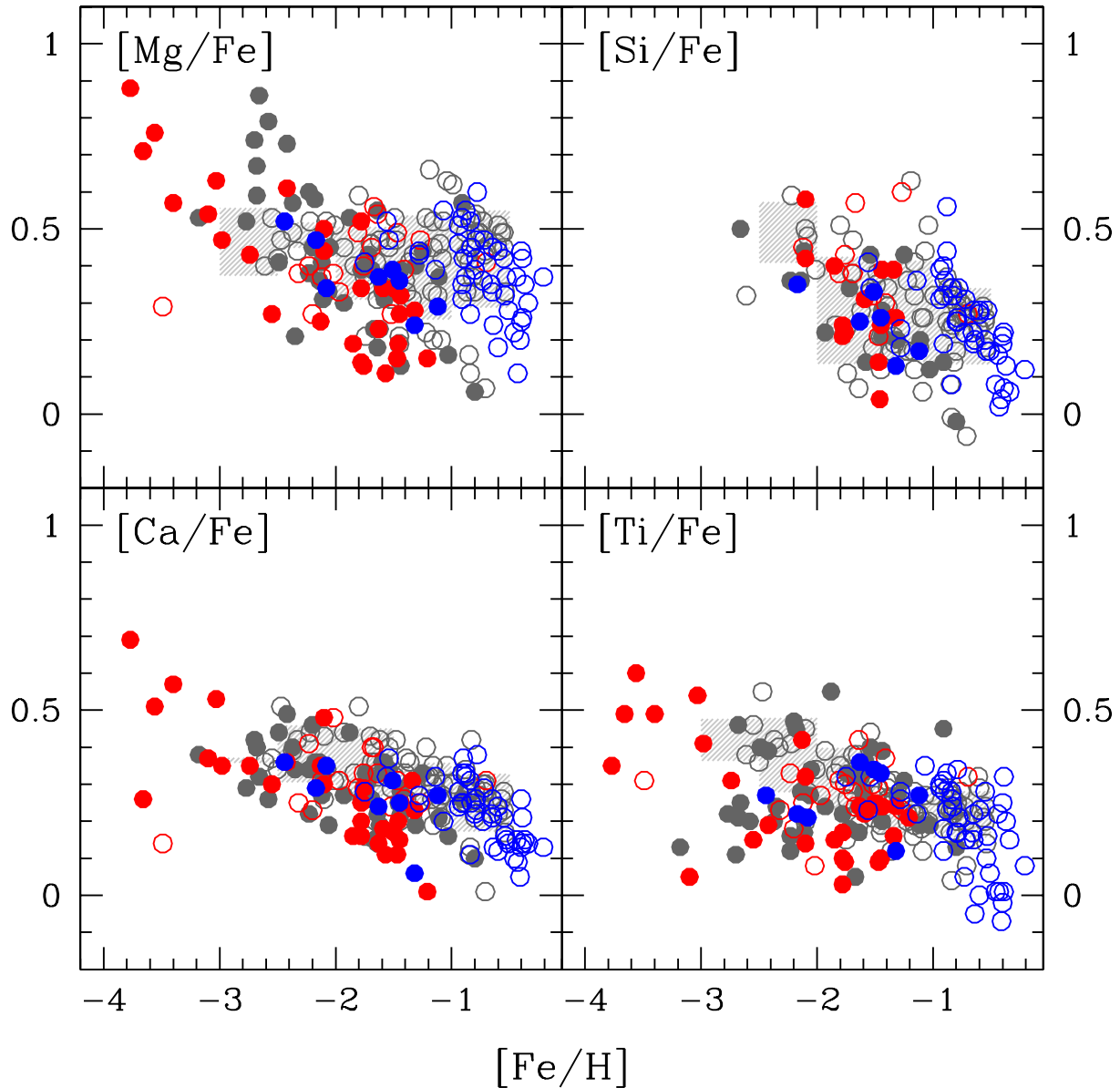


**Fig. 12.** Mg, Si, Ca and Ti abundance ratios as a function of  $[\text{Fe}/\text{H}]$ . As in Figure 1, *open* and *filled* symbols represent stars with  $Z_{\text{max}} \leq 5$  kpc and  $Z_{\text{max}} > 5$  kpc, respectively. *Blue*, *gray* and *red* colors represent stars with  $V_{\phi} > 150$  km s $^{-1}$ ,  $-50 < V_{\phi} \leq 150$  km s $^{-1}$  and  $V_{\phi} \leq -50$  km s $^{-1}$ , respectively. The shaded region highlights average and a  $1\sigma$  scatter of the abundance ratios for the sample stars with a typical inner halo kinematics, which is assumed to be  $Z_{\text{max}} \leq 5$  kpc and  $-50 < V_{\phi} \leq 150$  km s $^{-1}$ .



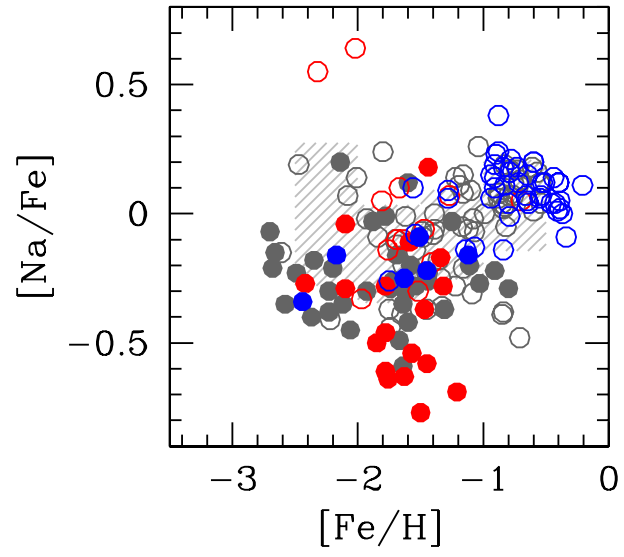


**Fig. 13.**  $[Na/Fe]$  as a function of  $[Fe/H]$ . The symbols are the same as in Figure 12.

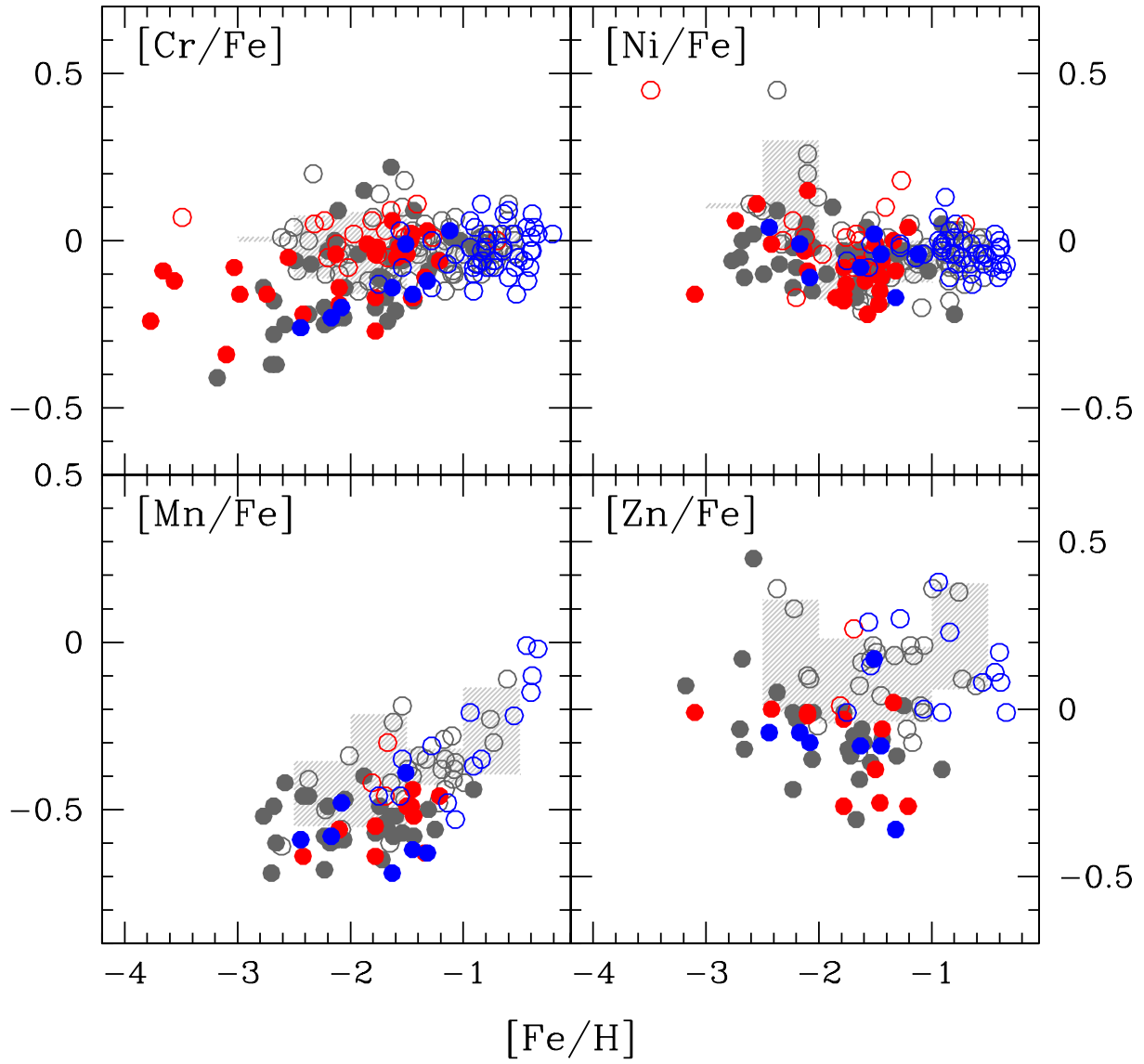


**Fig. 14.** Cr, Ni, Mn and Zn abundance ratios as a function of  $[Fe/H]$ . The symbols are the same as in Figure 12.

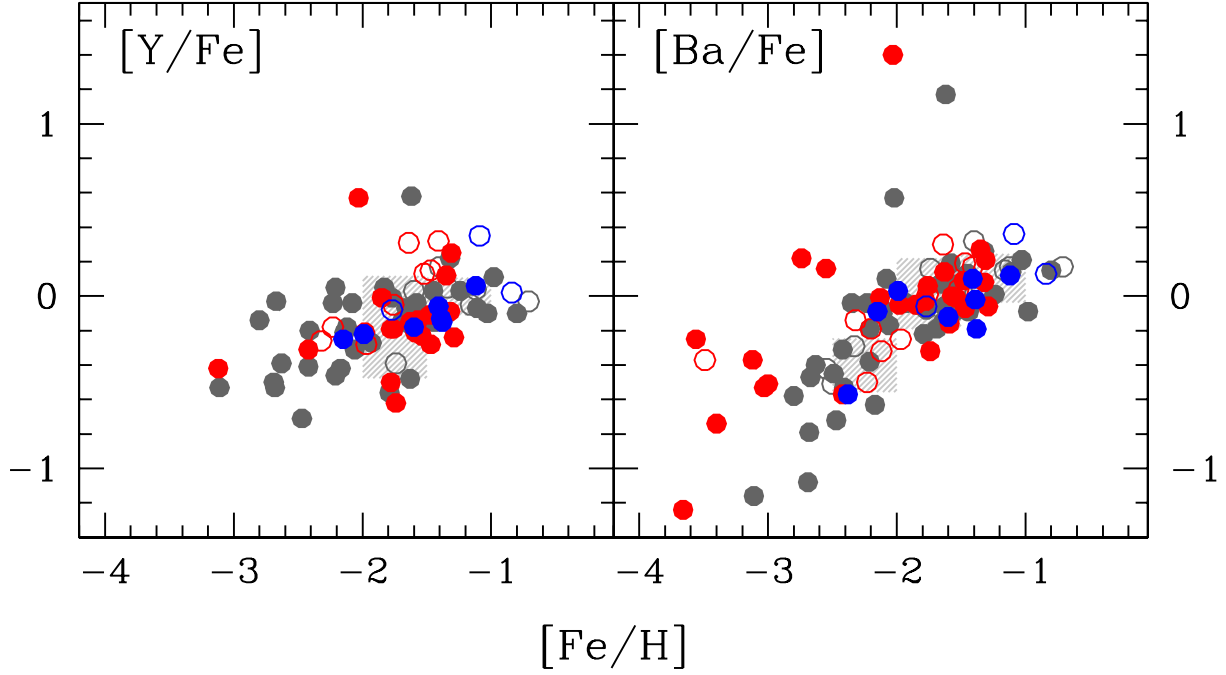


**Fig. 15.** Y and Ba abundance ratios as a function of  $[\text{Fe}/\text{H}]$ . The symbols are the same as in Figure 12. We note that one of the two objects having exceptionally high  $[\text{Y}/\text{Fe}]$  and  $[\text{Ba}/\text{Fe}]$  is a binary star (BD+04° 2466,  $[\text{Fe}/\text{H}] = -2.16$ ) while binary nature of another object (G 18-24,  $[\text{Fe}/\text{H}] = -1.62$ ) is unknown (Latham et al. 2002).

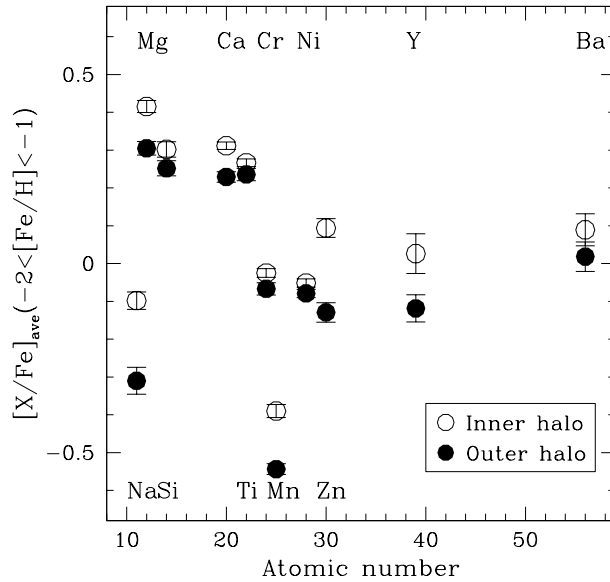


**Fig. 16.** Abundance pattern for the inner (*open* symbols) and the outer (*filled* symbols) halo stars. In this plot, average  $[\text{X}/\text{Fe}]$  values ( $[\text{X}/\text{Fe}]_{\text{ave}}$ ) in the metallicity range of  $-2 < [\text{Fe}/\text{H}] < -1$  are plotted. The error bar represents a standard deviation divided by a square-root of the number of objects ( $\sigma/\sqrt{N}$ ) in each of the inner and the outer halo sample.

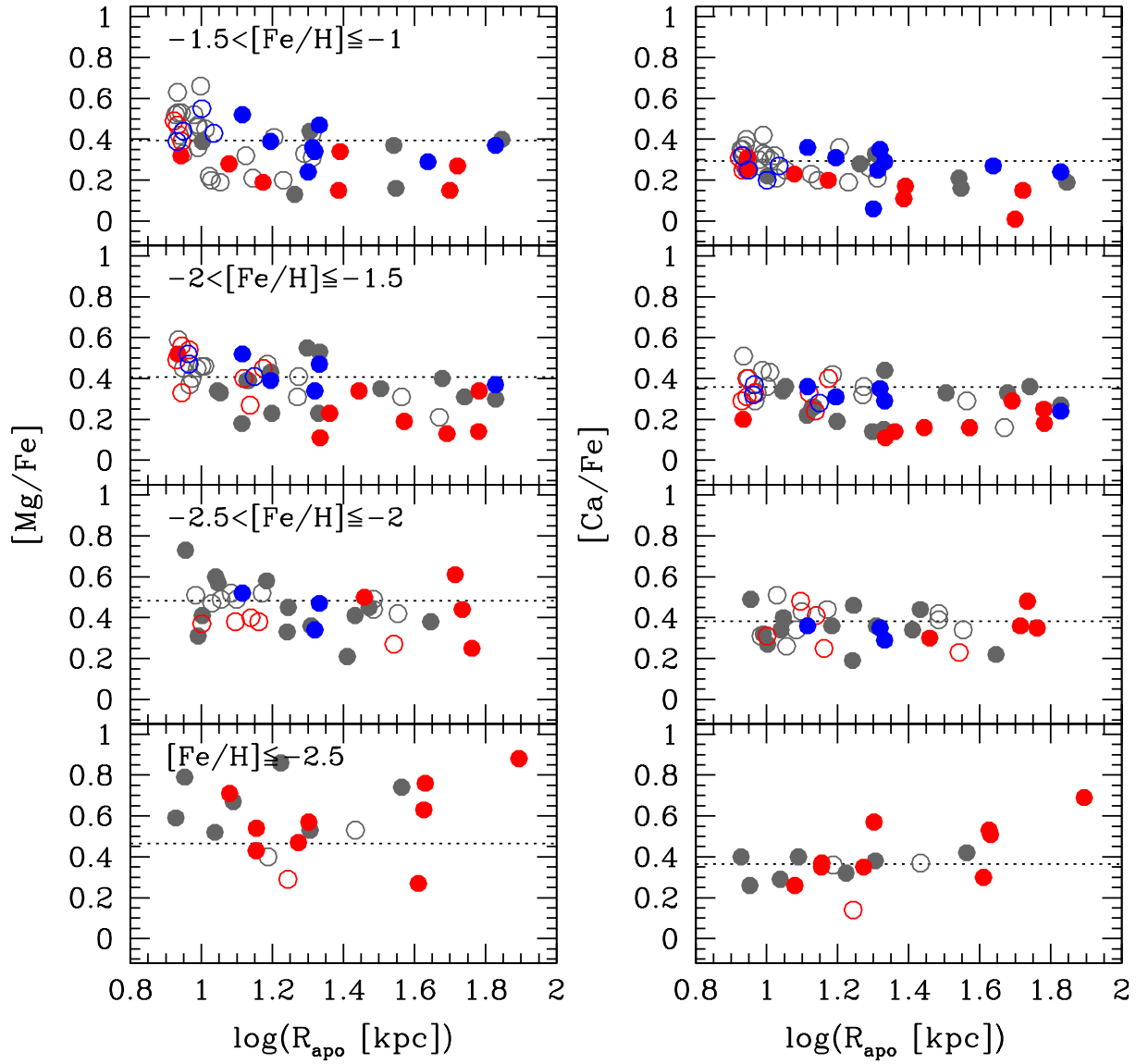


**Fig. 17.**  $[\text{Mg}/\text{Fe}]$  (*left* panel) and  $[\text{Ca}/\text{Fe}]$  (*right* panel) as a function of  $R_{\text{apo}}$  [kpc] for different metallicity ranges. The symbols are the same as in previous figures. Dotted lines in each panel show the average of the sample of the assumed typical inner halo ( $-50 < V_{\phi} \leq 150 \text{ km s}^{-1}$  and  $Z_{\text{max}} \leq 5 \text{ kpc}$ ) among each metallicity range.

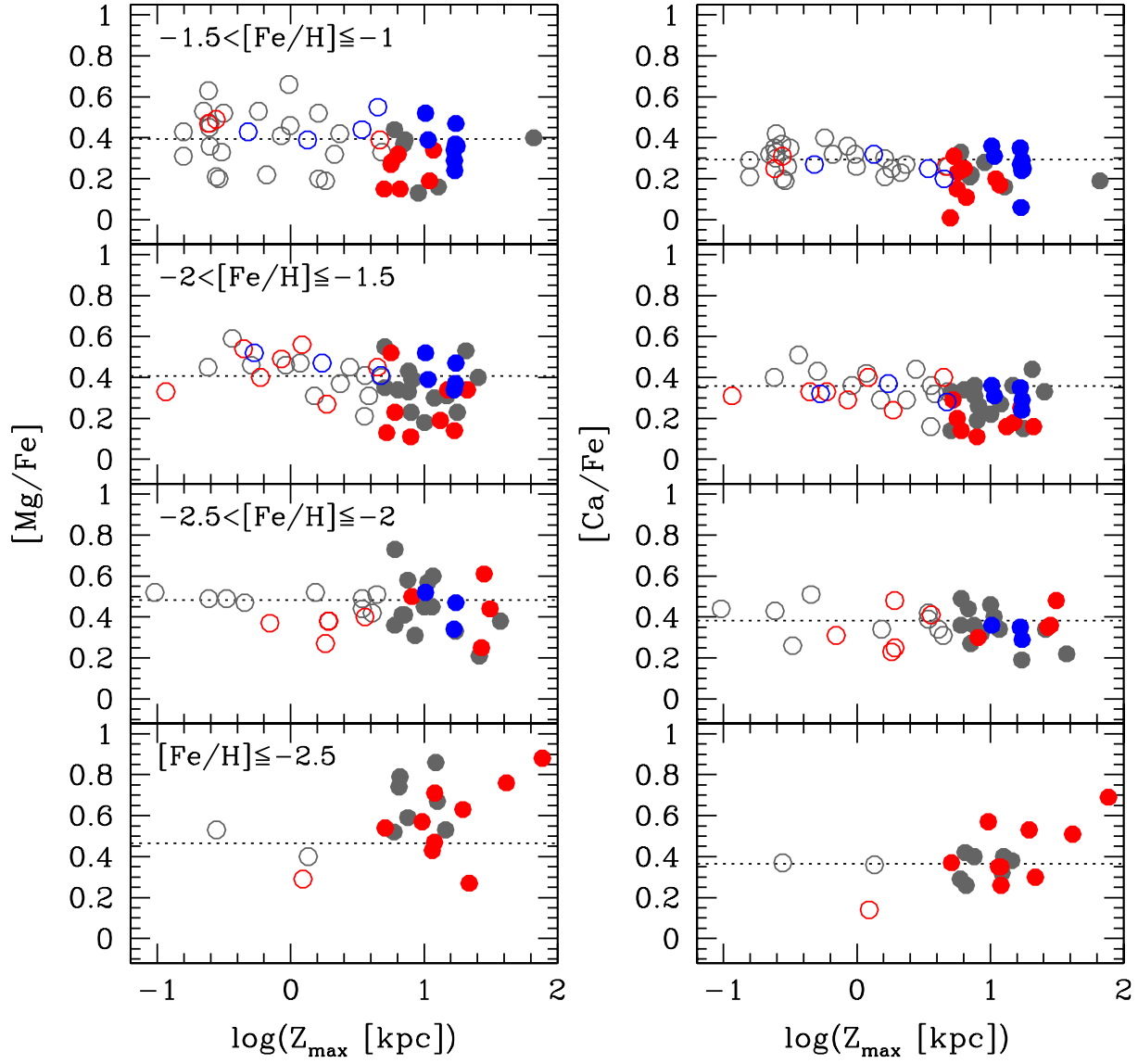


**Fig. 18.**  $[\text{Mg}/\text{Fe}]$ (left panel) and  $[\text{Ca}/\text{Fe}]$ (right panel) as a function of  $\log(Z_{\text{max}} [\text{kpc}])$  for different metallicity ranges. The symbols are the same as in previous figures. Dotted lines in each panel show the average of the sample of the assumed typical inner halo ( $-50 < V_{\phi} \leq 150 \text{ km s}^{-1}$  and  $Z_{\text{max}} \leq 5 \text{ kpc}$ ) among each metallicity range.

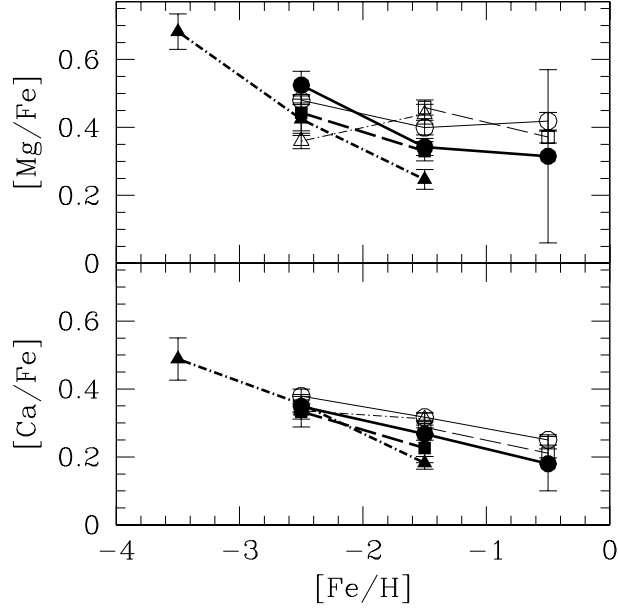


**Fig. 19.** Average  $[\text{Mg}/\text{Fe}]$  (*top*) and  $[\text{Ca}/\text{Fe}]$  (*bottom*) at each  $[\text{Fe}/\text{H}]$  bin for different kinematic subgroups. *Open* and *filled* symbols correspond to the inner and the outer halo sample, respectively. *Square*, *circle* and *triangle* correspond to  $V_\phi > 150$ ,  $-50 < V_\phi \leq 150$  and  $V_\phi \leq -50 \text{ km s}^{-1}$ , respectively. The error bars represent standard deviations divided by a square root of the number of objects in each  $[\text{Fe}/\text{H}]$  and kinematic domain.

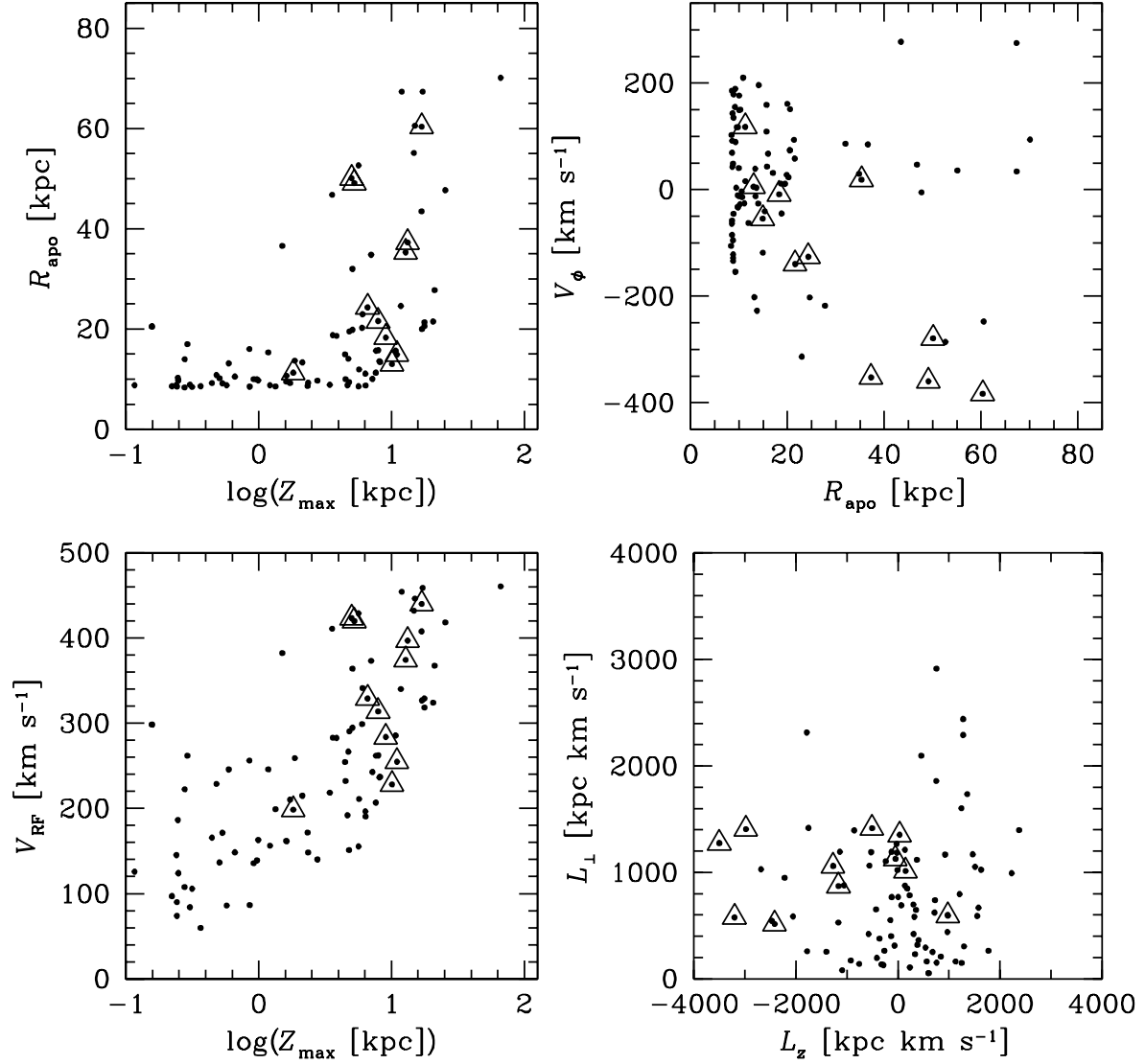


**Fig. 20.** Distribution of the sample stars in the planes defined in the orbital parameters. The sample stars with  $-2 < [\text{Fe}/\text{H}] < -1$  are plotted. *top-left:*  $Z_{\text{max}}-R_{\text{apo}}$ , *top-right:*  $R_{\text{apo}}-V_{\phi}$ , *bottom-left:*  $Z_{\text{max}}-V_{\text{RRF}}$ , *bottom-right:*  $L_z-L_{\perp}$ . The stars with  $[\text{Mg}/\text{Fe}] < 0.2$  are highlighted with *open triangles*.

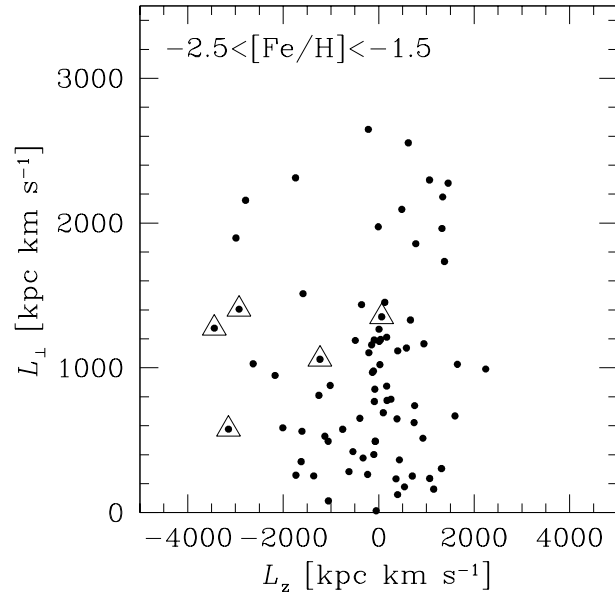


**Fig. 21.** Same as *bottom-right* panel of Figure 20 but now for metallicity interval of  $-2.5 < [\text{Fe}/\text{H}] < -1.5$



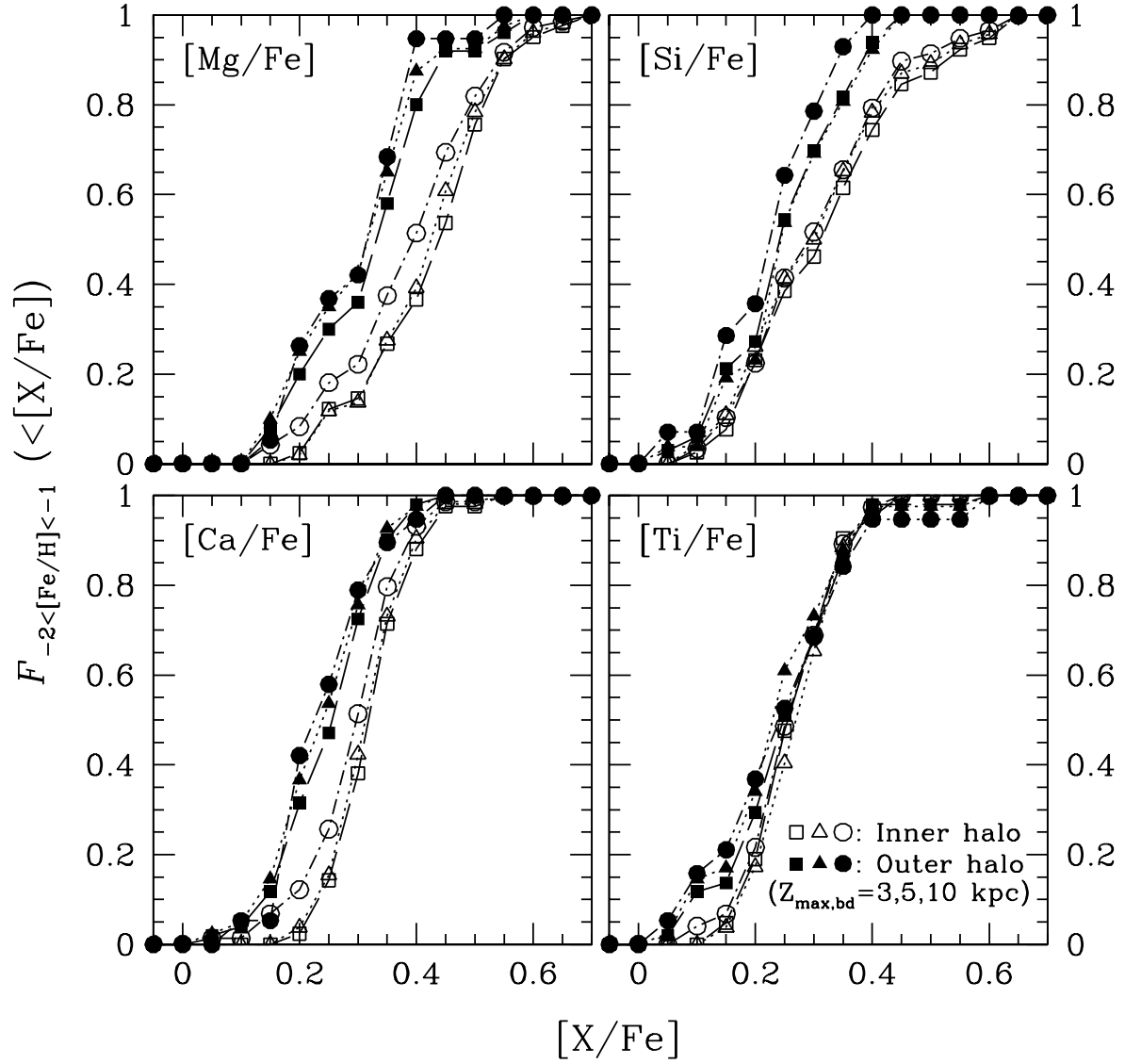


**Fig. 22.** Cumulative distribution of  $[X/Fe]$  for the sample stars with  $-2 < [Fe/H] < -1$  adopting various  $Z_{\max}$  boundaries ( $Z_{\max, \text{bd}} = 3, 5, 10$  kpc) to separate the inner and the outer halos. *Squares, triangles, circles* show distributions by setting the boundary as  $Z_{\max, \text{bd}} = 3, 5, 10$  kpc, respectively. *Open and filled* symbols show the corresponding distributions for the inner and the outer halo, respectively.

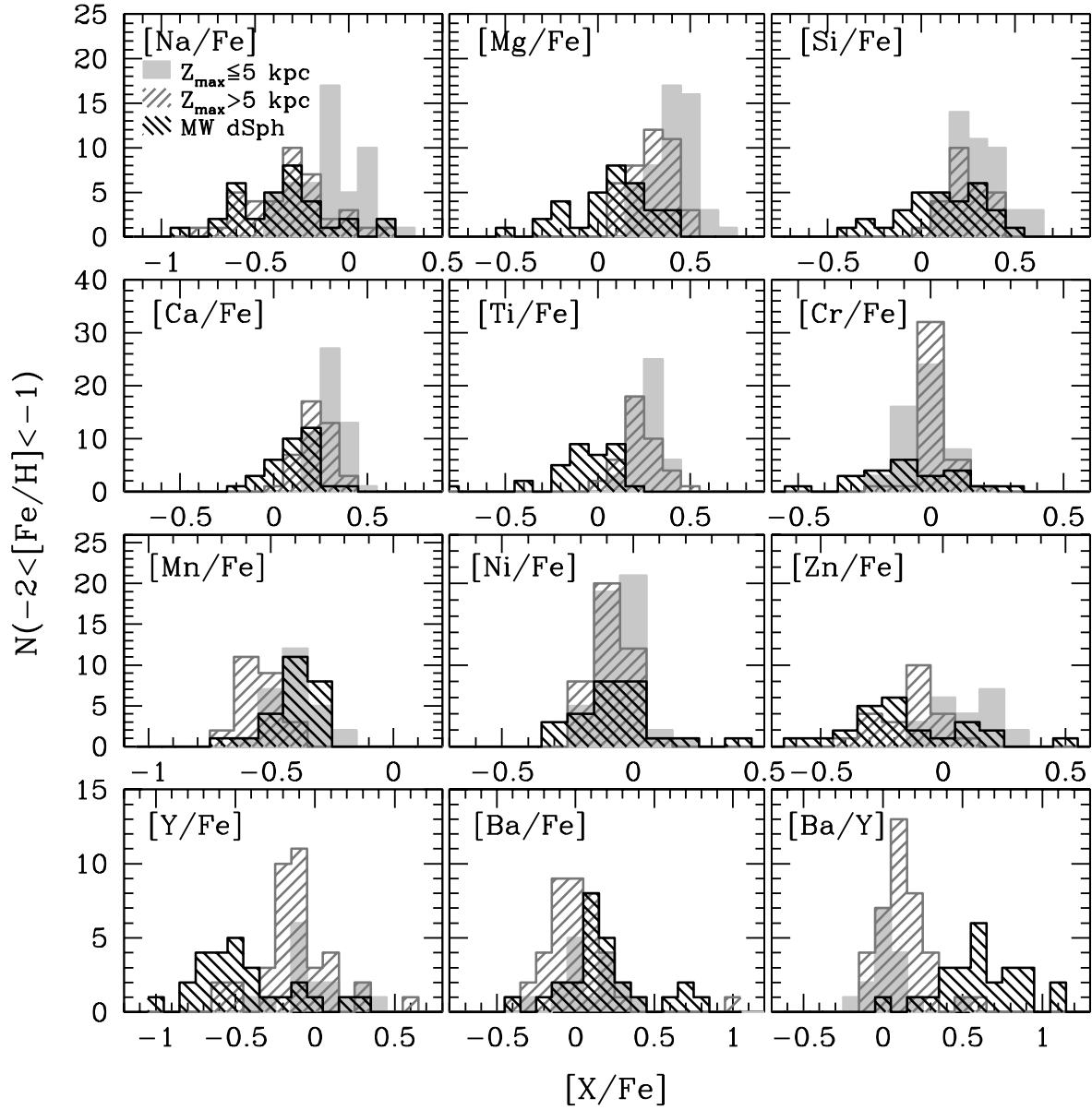


**Fig. 23.** Distribution of the abundance ratios for the inner and the outer halo samples (*gray-solid* and *gray-shaded* histogram, respectively) and the MW dSphs (*black-shaded* histogram) in the metallicity interval  $-2 < [\text{Fe}/\text{H}] < -1$ . The abundance data for the dSphs were taken from Shetrone et al. (2001), Shetrone et al. (2003), Geisler et al. (2005) and Koch et al. (2008a).